

CONSTITUTIVE MODELING OF FUSED DEPOSITION MODELING
ACRYLONITRILE BUTADIENE STYRENE (ABS)

A Thesis

by

MONISH SHIVAPPA MAMADAPUR

Submitted to the Office of Graduate Studies of
Texas A&M University
in partial fulfillment of the requirements for the degree of

MASTER OF SCIENCE

December 2007

Major Subject: Mechanical Engineering

CONSTITUTIVE MODELING OF FUSED DEPOSITION MODELING
ACRYLONITRILE BUTADIENE STYRENE (ABS)

A Thesis

by

MONISH SHIVAPPA MAMADAPUR

Submitted to the Office of Graduate Studies of
Texas A&M University
in partial fulfillment of the requirements for the degree of

MASTER OF SCIENCE

Approved by:

Chair of Committee,	Jyhwen Wang
Committee Members,	Hung-Jue Sue
	Yu Ding
Head of Department,	Dennis L. O'Neal

December 2007

Major Subject: Mechanical Engineering

ABSTRACT

Constitutive Modeling of Fused Deposition Modeling

Acrylonitrile Butadiene Styrene (ABS). (December 2007)

Monish Shivappa Mamadapur, B. E., Rashtreeya Vidyalaya College of Engineering,

Visvesvaraya Technological University

Chair of Advisory Committee: Dr. Jyhwen Wang

Fused deposition modeling is a rapid prototyping process that is widely used to create prototypes. Acrylonitrile butadiene styrene is the most widely used material for fused deposition modeling. The parts are fabricated in a layer by layer fashion and the individual layers are composed of fibers that are deposited, thus making them similar to parts made of a composite material. This study tries to model the behavior of this composite-like material to aid designers in designing parts made of such a “rapid prototyped” material. The mechanical material constants that need to be determined in order to obtain the compliance/stiffness matrix of the material have been identified and appropriate experiments have been conducted to determine them.

Biaxial tensile tests have been conducted to obtain the Young’s moduli and Poisson’s ratios. Torsion tests have been conducted to obtain the Shear moduli. Three point bending tests and combined loading tests have been conducted. Most of the experimental results are in excellent agreement with the analytical/finite element simulation results. Some that are not give a greater insight into the material behavior and have been discussed.

To Time.

ACKNOWLEDGEMENTS

I am thankful to Dr. Jyhwen Wang for all the encouragement and support. This thesis owes its genesis and completion to his critical reviews and excellent direction, and to his belief in me. I am also thankful to Dr. Hung-Jue Sue and Dr. Yu Ding for serving on my thesis committee and cooperating with me in their fullest capacity.

Special thanks to Rodney Inmon, Engineering Research Associate, Department of Aerospace Engineering, for without his help the tensile and torsion tests would have been impossible; it was a great learning experience. Special thanks also to James Sajewski, Master Instrument Maker, Department of Mechanical Engineering, for putting up with me at all times and helping me in fabricating the endless amount of testing specimens; that final last one was in fact the last one.

Special thanks also to my fellow researcher Liang Zhang whose inputs were extremely valuable in characterizing the material behavior. Thanks to my fellow researchers Wei Yang, Yu-Hsuan Huang and Mahesh Sonawane for all their inputs and help. Thanks also to the many staff members of the Departments of Mechanical Engineering, Engineering Technology and Industrial Distribution and Aerospace Engineering who helped me.

Thanks to my parents for the education, money and emotional support; all three were as valuable as the second.

TABLE OF CONTENTS

CHAPTER	Page
I	INTRODUCTION 1
	I. 1. Rapid prototyping 1
	I. 2. Fused deposition modeling 5
	I. 3. Literature review 10
	I. 4. Research objective and approach 17
II	MATERIAL CHARACTERIZATION 20
	II. 1. Material modeling 27
	II. 2. Torsion test 29
	II. 3. Tensile tests 33
III	MODELING OF FUSED DEPOSITION MODELING ABS MATERIAL .. 43
	III. 1. Torsion tests 43
	III. 2. Tensile tests 51
	III. 3. Assembly of compliance matrix 67
IV	APPLICATIONS OF THE CONSTITUTIVE MODEL 71
	IV.1. Three-point bending tests 71
	IV. 2. Combined bending and torsion tests 96
	IV. 3. Freeform body subjected to pressure loading 108
V	CONCLUSION 115
	REFERENCES 117
	APPENDIX A 121
	APPENDIX B 125
	VITA 128

LIST OF FIGURES

FIGURE		Page
1	Schematic of the FDM nozzle and platen	6
2	The rapid prototyping workstation.....	7
3	A schematic of the unidirectional and crisscross deposition strategies	9
4	Micrograph of a crisscross cross section	9
5	The Adelaide load frame on which torsion tests were conducted	30
6	A schematic of the torsion test specimen configurations.....	31
7	Close up of the torsion test.....	32
8	The MTS 100 KIP load frame	34
9	The MTS 632.85 biaxial extensometer	36
10	The extensometer calibrator.....	37
11	The specimen blocks that were used to calibrate the extensometer.....	38
12	A schematic of the <i>TN1</i> , <i>TN3.1</i> and <i>TN4</i> tensile test specimen configurations	41
13	A schematic of the <i>TN2</i> , <i>TN3.2</i> and <i>TN5</i> tensile test specimen configurations	42
14	A typical torsion curve of the <i>TR1</i> specimen configuration	44
15	A typical torsion curve of the <i>TR2</i> specimen configuration	45
16	A typical torsion curve of the <i>TR3</i> specimen configuration	46
17	A characteristic curve used to measure the shear modulus.....	47
18	Shear moduli of all specimen configurations.....	50
19	A characteristic stress-strain curve of the <i>TN4</i> specimen configuration.....	53

FIGURE	Page
20 A characteristic stress-strain curve of the <i>TN5</i> configuration.....	54
21 A characteristic stress-strain curve of the <i>TN3.1</i> specimen configuration.....	55
22 A characteristic stress-strain curve of the <i>TN3.2</i> specimen configuration.....	56
23 A characteristic stress-strain curve of the <i>TN1</i> configuration.....	57
24 A characteristic stress-strain curve of the <i>TN2</i> configuration.....	58
25 A characteristic plot used to calculate the Young's modulus	59
26 A characteristic plot used to calculate the Poisson's ratio.....	60
27 Young's moduli of all the specimen configurations	62
28 Poisson's ratios of all the specimen configurations.....	64
29 Dimensions of the three-point bending test specimens.....	72
30 A schematic of all the three-point bending test specimen configurations	72
31 A schematic of the three-point bending test	73
32 The Instron 4411 load frame on which the three-point bending tests were conducted	74
33 Close up of a specimen undergoing three-point bending.....	75
34 A characteristic load vs. slack deflection curve.....	77
35 A characteristic slack deflection vs. load curve that was used to calculate the y-intercept for toe compensation.....	78
36 A characteristic toe compensated load vs. absolute deflection curve.....	79
37 Deflections at 200 N of all the specimen configurations.....	81
38 The loading conditions of the beam in ABAQUS and the coordinate systems used to assign material orientations	82
39 Mesh density of the beam	84
40 Deflection of <i>3PI</i> specimen configuration	85

FIGURE	Page
41 Deflection of <i>3P2</i> specimen configuration	86
42 Deflection of <i>3P3</i> specimen configuration	87
43 Deflection of <i>3P4</i> specimen configuration	88
44 Simply supported beam configuration	90
45 Specimen dimensions of the specimens on which combined bending and torsion test was conducted (all dimensions are in mm)	97
46 The <i>CBT1</i> and <i>CBT2</i> specimen configurations.....	98
47 The TERCO Twist and Bend testing machine used to conduct the combined bending and torsion experiments	100
48 Close up of the dial gauge, specimen and the weight pan	101
49 (Left) The boundary conditions and the loading conditions on the specimen, and (Right) the two different coordinate systems used to simulate the two different specimen configurations	103
50 Mesh density of the combined bending and torsion specimen	105
51 Deflection of the <i>CBT1</i> specimen configuration	106
52 Deflection of the <i>CBT2</i> specimen configuration	107
53 The hollow freeform body subjected to the boundary and loading conditions.....	108
54 Mesh density of the freeform body	110
55 Von Mises stress in the freeform body made of bulk ABS	111
56 Von Mises stress in the freeform body made of fused deposition ABS	112
57 Deflection of the freeform body made of bulk ABS.....	113
58 Deflection in the freeform body made of fused deposition ABS.....	114

LIST OF TABLES

TABLE	Page
1 The shear moduli of the samples that underwent the torsion test, the average shear modulus of each specimen configuration and the standard deviation of the average moduli.....	49
2 The Young's moduli of the samples that underwent the tension test, the average Young's modulus of each specimen configuration and the standard deviation of the average moduli	61
3 The Poisson's ratios of the samples that underwent the tension test, the average Poisson's ratio of each specimen configuration and the standard deviation of the average ratio.....	63
4 The tensile strengths of the samples that underwent the tension test, the average tensile strength of each specimen configuration and the standard deviation of the average tensile strength.....	65
5 Deflection of all the specimens at 200 N, the average deflection of a specimen configuration and the corresponding standard deviation.....	80
6 A comparison table of the deflections of all specimen configurations at 200 N.....	93
7 Deflection of all the specimens at 100 g, the average deflection of a specimen configuration and the corresponding standard deviation.....	102

CHAPTER I

INTRODUCTION

I. 1. Rapid prototyping

Prototyping is an old practice whose intention is to realize the conceptualization of a design. A prototype has been defined [1] as “*the first or original example of something that has been or will be copied or developed; it is a model or a preliminary version.*” Rapid prototyping is a relatively new technology that speeds up the process of product development by creating prototypes in a very small period of time, especially when the model is complicated. Rapid prototyping processes, being a fabrication process, can be classified into three major groups. They are subtractive, additive and virtual [2].

Subtractive processes involve removal of the material from a *blank*, which is a workpiece (usually a block of material) whose dimensions are greater than that of the part. Nowadays, subtractive processes make use of the Computer aided design or Computer aided manufacturing (CAD/CAM) technologies to reduce the time taken to fabricate a part. Computer based drafting packages are used to create a three dimensional representation of the part which is then translated into a file format usable by the manufacturing software which plans the machining operations to be performed to fabricate the part. A numerically controlled machine then manufactures the part based on the output of the manufacturing software [2].

This thesis follows the style of ASME Journal of Engineering Materials and Technology.

Additive processes involve building the part in layers. Since the part is built in layers, additive processes require a software that slices the three dimensional representation of the part that is initially created using a computer based drafting package. After slicing the computer model into layers, each layer is analyzed separately and a set of instructions is compiled and provided to the machine with detailed information on how to create the part. Additive processes are much faster than subtractive processes in general [2].

Virtual prototyping involves using advanced design software packages that use advanced graphics and virtual reality environments to examine the three dimensional computer model of the part. The packages range from having graphics routines by using complex software to using virtual reality headgear and gloves with appropriate sensors that allows for observation of the prototype in a virtual environment [2]. These software packages are generally very expensive.

Another way to classify the various rapid prototyping systems broadly is by the initial form of its material. Accordingly, they are classified as liquid-based, solid-based and powder-based.

In liquid-bases rapid prototyping, the material is in its liquid state and is later on converted to a solid state through a process commonly called curing. The rapid prototyping systems that fall into this category are 3D Systems' Stereolithography Apparatus (SLA), Cubital's Solid Ground Curing (SGC), Sony's Solid Creation System (SCS), Mitsubishi's Solid Object Ultraviolet-laser Plotter (SOUP), EOS's Stereos Systems, Teijin Seiki's So-

liform System, Meiko's Rapid Prototyping System for the Jewellery Industry, Denken's SLP, Mitsui's COLAMM, Fockele & Schwarze's LMS, Light Sculpting, Two Laser Beams.

Solid-based rapid prototyping systems cover all bulk materials in solid state except for powder. This includes wires, rolls, laminates and pellets. The rapid prototyping systems that fall into this category are Helisys' Laminated Object Manufacturing (LOM), Stratasys' Fused Deposition Modeling (FDM), KIRA's Selective Adhesive and Hot Press (SAHP), Kinergy's Rapid Prototyping System, 3D Systems' Multi-Jet Modeling System (MJM), IBM's Rapid Prototyping System (RPS), Sanders Prototype Inc.'s Model Maker MM-6B, Sparx AB's Hot Plot, Scale Models Unlimited's LaserCAMM,

Although powder is definitely in the solid state in its strict sense, powder-based rapid prototyping is created as a separate category to mean powder in grain-like form. The rapid prototyping systems that fall into this category are DTM's Selective Laser Sintering (SLS), Soligen's Direct Shell Production Casting (DSPC), Fraunhofer's Multiphase Jet Solidification (MJS), EOS's EOSINT Systems, BPM Technology's Ballistic Particle Manufacturing (BPM), MIT's 3-Dimensional Printing (3DP)

The liquid-based methods generally use the photo-curing method while solid-based methods generally use either the cutting and gluing/joining method or the melting and solidifying/fusing method and the powder-based methods generally make use of the joining/binding method. All the above mentioned processes are explained in great deal in [1].

As discussed earlier, the input file to the rapid prototyping machine should be in a file format that is usable by the machine software. This necessitates a need for a standard interface to convey geometric descriptions to the rapid prototyping systems from the drafting packages. The STL (STereoLithiography) file, also written as .STL file, is used in most rapid prototyping systems as the *de facto* standard. The STL file was conceived by 3D Systems, USA. An unordered list of the triangular facets representing the outside skin of the part makes up an STL file. The two STL file formats are ASCII and binary. The binary format has a much smaller file size than the ASCII format, but the ASCII format is human readable. The triangular facets are described by a set of X, Y and Z coordinates for each of the three vertices along with a unit normal vector with x , y and z to indicate the side of the facet that is inside the part. The advantages of using an STL file are [1] that it provides a simple method of representing three dimensional models, it is used by most CAD systems and rapid prototyping systems and is already a *de facto* standard and it can provide simple files for data transfer for geometric shapes. The disadvantages of using an STL file are [1] that depending on the accuracy parameter, the file size may be many times larger than the original CAD data file, it carries much redundant information such as duplicate vertices and edges and the non robust tessellation algorithms used by CAD vendors today create geometric flaws in the file such as gaps, degenerate facets, overlapping facets and non-manifold topology conditions.

I. 2. Fused deposition modeling

Fused deposition modeling (FDMTM) is a rapid prototyping process that is patented as a technology and commercially marketed by Stratasys, Inc. In this process also, as with most rapid prototyping process, the part is deposited layer by layer; the layer itself, being deposited strand by strand. The conceptual design, which is created on a CAD software is inputted to the FDM system as an IGES or .STL file. Quickslice[®] and SupportWorkTM proprietary software then process the file. Slicing of the part into horizontal layers is done by Quickslice whereas the necessary support structures are generated by SupportWork software. The material is then deposited to create the part. This deposition is brought about by an extrusion nozzle to which the material is provided by the unwinding of a plastic filament coil. The nozzle head is heated to melt the material. The head can be moved horizontally or vertically and controlled to turn the flow of the material off or on (Fig. 1). The head moves to create the next layer upon completing the deposition of a layer. The support structures are deposited using a different secondary or release material. The support material forms a weak bond with the primary modeling material. Thus, the support material can be broken away from the part easily.

The x , y and z axes with reference to the platen on which the part is deposited is shown in Fig. 1. This is reference coordinate system of the machine in our laboratory and thus, this reference coordinated system has been used in creating the solid models using CAD software. The 1, 2 and 3 axes as shown in Fig. 1 are the directions along which the mechanical properties of the rapid prototyped material have been characterized, i.e., they have been selected as the principal directions of the material.

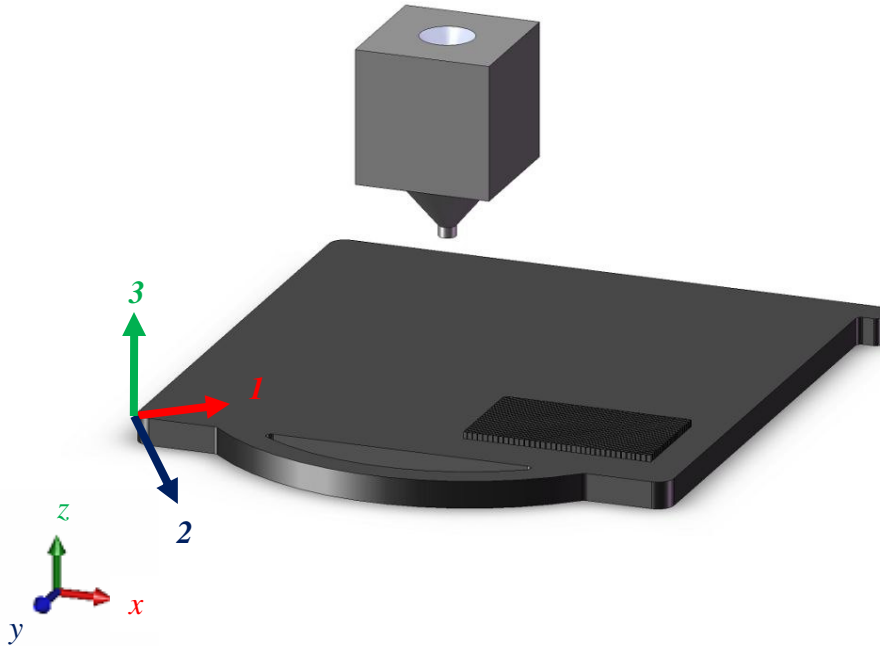


Fig. 1. Schematic of the FDM nozzle and platen

The FDM machines that are in our lab are the Dimension 3D printers (Dimension BST and Dimension SST 768). They have been manufactured by Stratasys, Inc. Both the machines in our lab are controlled by the same computer. BST stands for breakaway support technology and SST for soluble support technology. As the names indicate, the only difference between the two is that the supporting material is manually removed by breaking it away from the deposited part in BST and the supporting material may be removed by dissolving it in a liquid that does not react with part in SST [3]. The workstation is shown in Fig. 2. They convert a virtual solid model into a real one as described earlier. The virtual solid model is created as a computer file using a 3D modeling software package and saved in STL format. The Quickslice software then takes in the file and divides the solid model into layers to generate appropriate nozzle head path for the material to be depos-

ited. Quickslice then generates and executes the commands to make the printer “print” successive layers on top of each other to generate the real solid model.



Fig. 2. The rapid prototyping workstation

As described earlier, these machines can be used for making models and prototypes as well as functional parts. The material used to deposit the parts in these machines is Acrylonitrile Butadiene Styrene (ABS). ABS has been around since the late 1940's, and in the 1950's they underwent significant improvement as a result of improvements in polymer blending technology and the development of polymer grafting technology [4]. It is a commonly and extremely used thermoplastic that is used to manufacture appliance housings, shoe heels, pipes, chairs, insulated wires, automotive parts and pump impellers for

washing machines [4]. Some notable properties of ABS [4] are excellent impact strength and high rigidity, very good chemical and heat resistance properties, good creep resistance under heavy load and very low moisture absorption.

The two common types of deposition in FDM strategies are *unidirectional* and *crisscross* as shown in Fig. 3. While the angle between the corresponding strands in subsequent layers in unidirectional deposition is 0° , the angle between the corresponding strands in subsequent layers in crisscross deposition is 90° . And while the unidirectional deposition strategy provides the part with maximum strength along the path of deposition, crisscross deposition strategy provides the part with the equal strength in the plane of deposition (xy plane). Although both deposition strategies have their own strong points, the crisscross deposition is most suited to any part irrespective of its shape and position. A micrograph of a cross section of a crisscross part is shown in Fig. 4. Micrographs of various other cross sections are included in Appendix A.

As the number of applications where functional parts manufactured by FDM increase, it becomes necessary to characterize their physical properties. This may help designers in designing the parts that have load bearing applications. This will be the outcome of this research, in a nutshell.

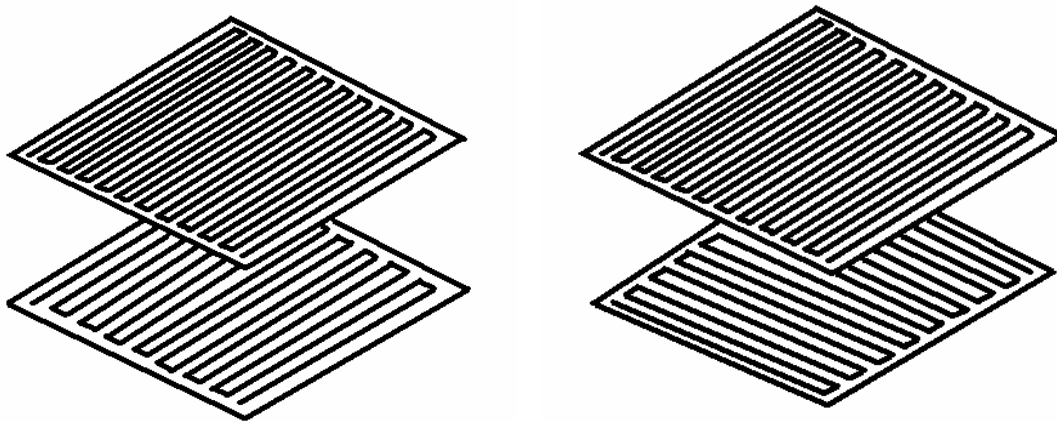


Fig. 3. A schematic of the unidirectional (left) and crisscross (right) deposition strategies



Fig. 4. Micrograph of a crisscross cross section

I. 3. Literature review

Masood [5] has presented an intelligent rapid prototyping framework that improves the efficiency and productivity of an FDM system. It has been suggested that a knowledge based system be incorporated in the system and use the framework right from the design phase of a problem. It has been claimed that doing so will result in an increased accuracy of the part as well as an optimized design.

Palmer et al. [6] have researched in the area of rapid prototyping of high density circuitry which involves the integration of direct write conductive ink dispensing technology with stereolithography to show that it is possible to manufacture robust electronic devices with integrated DL-SL structures.

Agarwala et al. [7] have investigated the structural quality of the parts processed by FDM. It has been concluded that the surface and internal defects that resulted from the then existing solid freeform fabrication (SFF) systems could severely limit the structural properties of the processed parts. The defects have been investigated and some strategies have been suggested as well, that, if implemented could eliminate the defects to a large extent and thus, greatly improve the properties of the processed parts.

Kulkarni and Dutta [8] have also worked on devising different deposition strategies to strengthen the material. Extensive experimentation has been carried out to prove that the proposed strategies to improve upon the existing ones have actually done so. The material has also been modeled, and the deposition paths have been analyzed taking into consid-

eration the voids formed during deposition. The material has been modeled on the lines of a composite laminate and the results were consistent with the experimental ones.

It can be seen that the researchers initially started out with improving the process and thought about various methods to increase the part quality and also optimize the part design. Once the process stabilized and a convention was established, the researchers then began to try to improve the part quality by trying out different deposition strategies. They were also gradually progressing towards improving the mechanical properties of the processed part. A few more researchers have investigated the mechanical properties of the processed part.

Rodríguez et al. [9] have experimented on unidirectional fused deposition ABS to determine its mechanical properties. Their long term objective was to develop a computationally automated capability for designing fused deposition materials with superior structural properties. Their specimens have been fabricated using the FDM 1600 system. The focus of their study has been the mechanical behavior of unidirectional fused deposition ABS materials with three different mesostructures; an aligned mesostructure with fiber-to-fiber gap setting, $g = -25.4 \mu\text{m}$, a skewed configuration with $g = -25.4 \mu\text{m}$ and a skewed configuration with $g = 76.2 \mu\text{m}$. Tensile tests have been performed on specimens with various fiber orientations to determine the in-plane elastic constants under the assumption of orthotropic material symmetry. The results have been reported and it has been concluded that “the results can be used in future research to benchmark various analytical and computational models for fused deposition ABS stiffness and strength as a function of the

mesostructure (i.e. void density and interfacial density) and base material properties.” Rodríguez et al. [10] have also developed an analytical/computational model for the unidirectional fused deposition material stiffness and strength as a function of mesostructural parameters. The strength of materials as well as elasticity based approaches have been used to model the elastic moduli of unidirectional fused deposition ABS materials with the three different mesostructures as described in their previous work [9]. The unidirectional fused deposition materials have been modeled as three-dimensional homogeneous linear elastic orthotropic continua, and it has been identified that nine independent elastic moduli have to be specified to characterize the linear elastic constitutive equation for this material, where the effective moduli depend on the moduli of the bulk material (ABS) and the mesostructure of the fused deposition material. Using the mechanics of material/strength of materials approach, the effective moduli have been developed considering the material to be a solid with aligned prismatic voids. Thus, equations have been developed to calculate the effective moduli as a function of the corresponding elastic moduli of the bulk material and the void density. Using the theory of homogenization/elasticity based approach, the displacement is expressed as a perturbed solution in the period of the micro/meso structure which is assumed to tend to zero. Excellent results have been obtained from both the approaches. It was seen that the homogenization approach matched closely with the analytical method. The homogenization offered the advantage of providing a set of elastic moduli which are complete and coherent. However, the strength of materials method offered the great advantage of simplicity. Rodríguez et al. [11] have also furthered their study by developing a methodology for optimizing the mechanical performance parts made of fused deposition ABS. This optimization methodology allows

manufacturing parts with the maximum load carrying capacity. The results from [6 and 8] have been used and integrated with an optimization algorithm to achieve the objective.

Ahn et al. [12] have characterized the properties of ABS parts fabricated by the FDM 1650 system. The various build parameter considerations, which were likely to affect the properties of FDM parts, such as bead width, air gap, model-build temperature, raster orientation and color have been identified. The goal of the experiments has been to determine the effect of changing selected design and process variables on the tensile strength of the FDM specimens. Their tensile specimens consisted of 12 layers with various raster orientations. They have performed tensile experiments on $[0^\circ]_{12}$ axial, $[45^\circ/-45^\circ]_6$ criss-cross, $[0^\circ/90^\circ]_6$ cross and $[90^\circ]_{12}$ transverse raster orientation specimens and have reported their results. Also, these tests have been performed on specimens with zero air gap as well as specimens with -0.003 inch air gap. Compression tests have been performed as well, but this time the only consideration was the build direction. The results have been reported and it is seen that the material shows higher compressive strengths compared to the tensile strengths. Based on the experimental results and observations, 6 build rules to improve the strength and quality of FDM parts have been formulated.

It should be noted that the above notation follows that of laminate designation of composite materials [14]. $[0^\circ]_{12}$ means that the material was deposited along an axis that was inclined at 0° to the x-axis of the machine and consisted of 12 layers. Similarly, $[45^\circ/-45^\circ]_6$ means that the material was deposited along an axis that was inclined at 45° and -45° to

the x-axis of the machine, subsequently. 6 layers of each type were deposited and so there were a total of 12 layers. The other conventions also follow the same rules.

Bellini and Güçeri [13] have tried to characterize the mechanical behavior of parts fabricated using FDM. The stiffness matrix for fused deposition ABS materials has been determined. It has been identified that the material exhibits orthotropic behavior and the strain-stress relation is as below (Eq. (1)):

$$\begin{bmatrix} \varepsilon_1 \\ \varepsilon_2 \\ \varepsilon_3 \\ \gamma_{23} \\ \gamma_{13} \\ \gamma_{12} \end{bmatrix} = \begin{bmatrix} \frac{1}{E_1} & \frac{-\nu_{12}}{E_1} & \frac{-\nu_{13}}{E_1} & 0 & 0 & 0 \\ \frac{-\nu_{21}}{E_2} & \frac{1}{E_2} & \frac{-\nu_{23}}{E_2} & 0 & 0 & 0 \\ \frac{-\nu_{31}}{E_3} & \frac{-\nu_{32}}{E_3} & \frac{1}{E_3} & 0 & 0 & 0 \\ 0 & 0 & 0 & \frac{1}{G_{23}} & 0 & 0 \\ 0 & 0 & 0 & 0 & \frac{1}{G_{13}} & 0 \\ 0 & 0 & 0 & 0 & 0 & \frac{1}{G_{12}} \end{bmatrix} \cdot \begin{bmatrix} \sigma_1 \\ \sigma_2 \\ \sigma_3 \\ \tau_{23} \\ \tau_{13} \\ \tau_{12} \end{bmatrix} \quad (1)$$

where,

ε_1 , ε_2 and ε_3 are the normal strains in the principal directions of the material,

γ_{23} , γ_{13} and γ_{12} are the shear strains on the planes of symmetry,

σ_1 , σ_2 and σ_3 are the normal stresses corresponding to the normal strains,

τ_{23} , τ_{13} and τ_{12} are the shear stresses corresponding to the shear strains,

E_1 , E_2 and E_3 ; and ν_{12} , ν_{13} , ν_{23} , ν_{21} , ν_{31} and ν_{32} are the Young's moduli and Poisson's ratios corresponding to the normal stresses and strains, and

G_{23} , G_{13} and G_{12} are the shear moduli corresponding to the shear stresses and strains.

It has been identified that to define the material's mechanical behavior, determination of nine independent constants becomes necessary. It has been explained that the Young's moduli (Eq. (2)) and Poisson's ratios (Eq. (3)) can be obtained from the stress-strain diagrams as below:

$$E_x = \frac{\Delta\sigma_x}{\Delta\varepsilon_x} \quad (2)$$

where,

$\Delta\sigma$ is the change in the stress of the material,

$\Delta\varepsilon$ is the corresponding change in the strain, and

x is the loading direction.

and

$$\nu_{xy} = -\frac{\varepsilon_y}{\varepsilon_x} \quad (3)$$

where,

x is the loading direction, and

y is the direction perpendicular to it.

Further, it has been said that the in-plane shear modulus can be obtained by testing a 45° oriented unidirectional test specimen according to the following equation:

$$G_{ab} = \frac{E_x}{2(1 + \nu_{xy})} \quad (4)$$

Where x is the direction of load application and y is the direction perpendicular to it. Furthermore, a and b correspond 1 and 2 for specimens built in the xy plane, 1 and 3 for the ones built in xz plane and 2 and 3 for the ones built in the yz plane.

Two kinds of toolpaths have been used to fabricate their test specimens; the pseudo-isotropic or $[0\ 90\ +45\ -45]$ path or configuration, and the domain decomposition raster, and the machine in which they were fabricated was FDM 1650.

While the Young's moduli and Poisson's ratios can be determined from Eqs. (2) and (3) respectively for any specimen irrespective of the toolpath, Eq. (4) can only be used if the specimen is unidirectional, with the fibers or roads running perpendicular to the plane on which the shear modulus is being measured. But, the authors seem to have used the $[0\ 90\ +45\ -45]$ toolpath for fabricating their specimens that were used to measure the shear moduli. For a generally orthotropic material, as it has been said earlier in their paper, the shear moduli are independent of the other material properties, hence validating the existence of the nine independent properties discussed earlier.

Tests have then been conducted on the domain decomposition raster specimens to find their mechanical properties as well. But, it was unable to measure the shear moduli in this case because it was not possible to build specimens oriented at 45° in the yz and xz planes because of the small size of a single layer section, thus rendering the stiffness matrix of the domain decomposition lay-up incomplete. Flexure tests have been conducted; and subsequently finite element simulations have been conducted using ANSYS 5.5 to show

the difference between considering the material to be isotropic and considering the material to be orthotropic.

I. 4. Research objective and approach

Many powerful FEA packages are available nowadays for researchers to conduct simulations to verify their results. But even the most powerful FEA packages have their own limitations in performing the simulations. Most packages require that the mesh size and aspect ratio be good enough to obtain good results. Also, having an extremely large number of elements in the material also requires a lot of computation time and also great computational power. It is essential to have a fine balance between the two requisites to obtain a reasonably good mesh size, which can be thought of as one that doesn't consume an extremely large amount of time and computational power for simulating the part loading conditions as well as gives accurate enough results.

It may be possible that the parts manufactured by FDM be analyzed using the FEA packages by entering the properties of the raw material in the package, and making a strand by strand and layer by layer 3D model of the part in the package (which is the way it actually is). Also, this would require us to know the bonding strength between successive strands as well as the bonding strength between successive layers, which would be a difficult parameter to measure. Assuming that we measure the bonding strengths also, the futility of analyzing the part in the above mentioned way becomes obvious when we think of the thickness of the strands in comparison with the size of the normally manufactured parts. It would result in hundreds of thousands of elements in the part after mesh-

ing. This process would require a great amount of time to model even simple parts, leave alone the computational time required to run the simulations after modeling and meshing the parts. It would defeat the whole objective of “rapid” prototyping by slowing down the design process very much.

Hence, considering all the above difficulties and issues involved in simulating the manufactured parts in the above mentioned way, it is proposed that the parts be treated as though they have been manufactured by a different material (hereafter referred to as rapid prototyped material) whose properties depend on the deposition strategy and other parameters. It may be so that the rapid prototyped material may have properties similar to that of the material from which it is made (the bulk material), but it will still have many deviations from the bulk material. One of the most obvious one being that the rapid prototyped material will not remain isotropic any more even if the parent material is isotropic. It is proposed that the moduli be obtained independently of each other from experiments that shall enable us to use their basic equations. Thus, the whole objective of this research is to determine the materials properties of the rapid prototyped material. Determination of the material properties of a rapid prototyped material also requires suitable verification to see the correctness of the results.

The rapid prototyped material will be characterized first, i.e., the behavior of the material will be investigated into, followed by a detailed study of the characteristic equations of the material. This will help us determine the mechanical constants that need to be determined in order to obtain the deformations, stresses and strains in the material upon load-

ing it. The mechanical constants will then be determined using their definitions and fundamental equations, using the appropriated testing apparatus. After determining the mechanical constants, the accuracy of the results will be verified by comparing the experimental results with the results obtained from the finite element simulations and analytical methods. The experiments will also help us establish the accuracy of material characterization.

CHAPTER II

MATERIAL CHARACTERIZATION

Characterizing a material involves obtaining a relation between stress in the material and the corresponding strain within its elastic limit. A material may be characterized based on the existence of any planes of symmetry, i.e., its behavior when loaded in various directions. As it has been described earlier, the Dimension BST 768 and SST 768 in our laboratory always deposit the material in a crisscross fashion, i.e., the toolpath is always $[+45^\circ/-45^\circ]$. Since the material is made of fibers in a plane and the fibrous planes are deposited layer by layer, the material may be imagined to be like a composite material with fibers laid out in the $[+45^\circ/-45^\circ]$ configuration. While it may be easy to visualize that the material is orthotropic [14] in nature because it has three planes of symmetry, upon further examination it becomes clear that the material in fact exhibits a special case of orthotropy, which means that the material is essentially orthotropic, but on one of its planes, the Young's moduli of the two perpendicular directions, and the corresponding Poisson's ratios are the same, but the corresponding shear modulus is still independent of the Young's modulus or the Poisson's ratio. Thus, the material comes close to being a transversely isotropic material, but is not. This part is explained in more detail in the following paragraphs.

The stress-strain relations for an orthotropic material are as given below [15]:

$$\begin{bmatrix} \sigma_1 \\ \sigma_2 \\ \sigma_3 \\ \tau_{23} \\ \tau_{13} \\ \tau_{12} \end{bmatrix} = \begin{bmatrix} C_{11} & C_{12} & C_{13} & 0 & 0 & 0 \\ C_{12} & C_{22} & C_{23} & 0 & 0 & 0 \\ C_{13} & C_{23} & C_{33} & 0 & 0 & 0 \\ 0 & 0 & 0 & C_{44} & 0 & 0 \\ 0 & 0 & 0 & 0 & C_{55} & 0 \\ 0 & 0 & 0 & 0 & 0 & C_{66} \end{bmatrix} \begin{bmatrix} \varepsilon_1 \\ \varepsilon_2 \\ \varepsilon_3 \\ \gamma_{23} \\ \gamma_{13} \\ \gamma_{12} \end{bmatrix} \quad (5)$$

and

$$\begin{bmatrix} \varepsilon_1 \\ \varepsilon_2 \\ \varepsilon_3 \\ \gamma_{23} \\ \gamma_{13} \\ \gamma_{12} \end{bmatrix} = \begin{bmatrix} S_{11} & S_{12} & S_{13} & 0 & 0 & 0 \\ S_{12} & S_{22} & S_{23} & 0 & 0 & 0 \\ S_{13} & S_{23} & S_{33} & 0 & 0 & 0 \\ 0 & 0 & 0 & S_{44} & 0 & 0 \\ 0 & 0 & 0 & 0 & S_{55} & 0 \\ 0 & 0 & 0 & 0 & 0 & S_{66} \end{bmatrix} \begin{bmatrix} \sigma_1 \\ \sigma_2 \\ \sigma_3 \\ \tau_{23} \\ \tau_{13} \\ \tau_{12} \end{bmatrix} \quad (6)$$

Where, C_{ij} and S_{ij} are the stiffness and compliance matrices respectively. The three important observations that can be made with respect to the stress-strain relation in Eqs. (5) and (6) are [14]:

1. “No interaction exists between normal stresses σ_1 , σ_2 , σ_3 and shear strains γ_{23} , γ_{13} , γ_{12} ; i.e., normal stresses acting along principal material directions produce only normal strains.”
2. “No interaction exists between shear stresses τ_{23} , τ_{13} , τ_{12} and normal strains ε_1 , ε_2 , ε_3 ; i.e., shear stresses acting on principal material planes produce only shear strains.”
3. “No interaction exists between shear stresses and shear strains on different planes; i.e., a shear stress acting on a principal plane produces a shear strain only on that plane.”

In terms of engineering constants, the stress-strain relations are expressed as follows [15]:

$$\begin{bmatrix} \varepsilon_1 \\ \varepsilon_2 \\ \varepsilon_3 \\ \gamma_{23} \\ \gamma_{13} \\ \gamma_{12} \end{bmatrix} = \begin{bmatrix} \frac{1}{E_1} & \frac{-\nu_{21}}{E_2} & \frac{-\nu_{31}}{E_3} & 0 & 0 & 0 \\ \frac{-\nu_{12}}{E_1} & \frac{1}{E_2} & \frac{-\nu_{32}}{E_3} & 0 & 0 & 0 \\ \frac{-\nu_{13}}{E_1} & \frac{-\nu_{23}}{E_2} & \frac{1}{E_3} & 0 & 0 & 0 \\ 0 & 0 & 0 & \frac{1}{G_{23}} & 0 & 0 \\ 0 & 0 & 0 & 0 & \frac{1}{G_{13}} & 0 \\ 0 & 0 & 0 & 0 & 0 & \frac{1}{G_{12}} \end{bmatrix} \cdot \begin{bmatrix} \sigma_1 \\ \sigma_2 \\ \sigma_3 \\ \tau_{23} \\ \tau_{13} \\ \tau_{12} \end{bmatrix} \quad (7)$$

where,

1, 2 and 3 are the principal axes directions as shown in Fig. 1,

ε is the normal strain,

γ is the shear strain,

σ is the normal stress,

τ is the shear stress,

E is the Young's modulus,

ν is the Poisson's ratio, and

G is the shear modulus of the material.

It may be noted that Eq. (7) is essentially the same as Eq. (1). From the symmetry of the compliance matrix, it follows that, in general,

$$\frac{\nu_{ij}}{E_i} = \frac{\nu_{ji}}{E_j} \quad (8)$$

It is also clearly seen from Eqs. (5) and (6) that an orthotropic material can be characterized by nine independent elastic constants. This means that there exists no relationship among the nine constants and there is no way we can find out one provided we have the knowledge of the others.

A material is said to be transversely isotropic if one of its principal planes is a plane of isotropy, i.e., one on one of its planes the mechanical material properties are the same in all directions. The existence of transverse isotropy makes the above equations, i.e., Eqs. (5) - (7), simpler. For 1-2 plane of isotropy, the subscripts 1 and 2 in the material constants can be interchanged and also the subscripts 5 and 6 can be interchanged in Eqs. (5) and (6). Thus the stress strain relations of a transversely isotropic material are [14]:

$$\begin{bmatrix} \sigma_1 \\ \sigma_2 \\ \sigma_3 \\ \tau_{23} \\ \tau_{13} \\ \tau_{12} \end{bmatrix} = \begin{bmatrix} C_{11} & C_{12} & C_{13} & 0 & 0 & 0 \\ C_{12} & C_{11} & C_{13} & 0 & 0 & 0 \\ C_{13} & C_{13} & C_{33} & 0 & 0 & 0 \\ 0 & 0 & 0 & C_{44} & 0 & 0 \\ 0 & 0 & 0 & 0 & C_{44} & 0 \\ 0 & 0 & 0 & 0 & 0 & \frac{C_{11} - C_{12}}{2} \end{bmatrix} \cdot \begin{bmatrix} \varepsilon_1 \\ \varepsilon_2 \\ \varepsilon_3 \\ \gamma_{23} \\ \gamma_{13} \\ \gamma_{12} \end{bmatrix} \quad (9)$$

and

$$\begin{bmatrix} \varepsilon_1 \\ \varepsilon_2 \\ \varepsilon_3 \\ \gamma_{23} \\ \gamma_{13} \\ \gamma_{12} \end{bmatrix} = \begin{bmatrix} S_{11} & S_{12} & S_{13} & 0 & 0 & 0 \\ S_{12} & S_{11} & S_{13} & 0 & 0 & 0 \\ S_{13} & S_{13} & S_{33} & 0 & 0 & 0 \\ 0 & 0 & 0 & S_{44} & 0 & 0 \\ 0 & 0 & 0 & 0 & S_{44} & 0 \\ 0 & 0 & 0 & 0 & 0 & 2(S_{11} - S_{12}) \end{bmatrix} \begin{bmatrix} \sigma_1 \\ \sigma_2 \\ \sigma_3 \\ \tau_{23} \\ \tau_{13} \\ \tau_{12} \end{bmatrix} \quad (10)$$

In terms of engineering constants, the following constants are related in a transversely isotropic material [15]:

$$E_1 = E_2, \quad G_{13} = G_{23}, \quad \nu_{32} = \nu_{31} \quad \text{and} \quad G_{12} = \frac{E_1}{2(1+\nu_{12})} \quad (11)$$

And the stress-strain relations in terms of engineering constants now become:

$$\begin{bmatrix} \varepsilon_1 \\ \varepsilon_2 \\ \varepsilon_3 \\ \gamma_{23} \\ \gamma_{13} \\ \gamma_{12} \end{bmatrix} = \begin{bmatrix} \frac{1}{E_1} & \frac{-\nu_{21}}{E_1} & \frac{-\nu_{31}}{E_3} & 0 & 0 & 0 \\ \frac{-\nu_{12}}{E_1} & \frac{1}{E_1} & \frac{-\nu_{31}}{E_3} & 0 & 0 & 0 \\ \frac{-\nu_{13}}{E_1} & \frac{-\nu_{13}}{E_1} & \frac{1}{E_3} & 0 & 0 & 0 \\ 0 & 0 & 0 & \frac{1}{G_{13}} & 0 & 0 \\ 0 & 0 & 0 & 0 & \frac{1}{G_{13}} & 0 \\ 0 & 0 & 0 & 0 & 0 & \frac{2(1+\nu_{12})}{E_1} \end{bmatrix} \begin{bmatrix} \sigma_1 \\ \sigma_2 \\ \sigma_3 \\ \tau_{23} \\ \tau_{13} \\ \tau_{12} \end{bmatrix} \quad (12)$$

Close examination of Eqs. (9), (10) and (12) reveals that the number of independent constants in the compliance or stiffness matrix is only five. It is thus possible to characterize

the material provided that the five independent constants, viz., E_1 , ν_{21} , ν_{31} , E_3 and G_{13} are known.

It has been stated earlier that the rapid prototyped material comes close to being transversely isotropic, but is not. This is because in rapid prototyped ABS, the shear stress in the 12 plane is also independent of the corresponding normal stress like the other two shear stresses. If the manner in which the part is built in the machines is considered, it can be seen that the crisscross $[+45^\circ/-45^\circ]$ toolpath actually makes the material have the same Young's modulus and Poisson's ratio along the principal directions in the 12 plane. This is a natural outcome of crisscross deposition. While it may be argued that a single layer itself is unidirectional and hence orthotropic, if two layers are considered together at all times, it becomes quite clear that the material has the same Young's modulus and Poisson's ratio. The fact that the shear modulus is independent of the other two mechanical material constants is because the layer to layer bonding is the chief strength when the material is in shear, and the unidirectional fiber strength is the chief strength when the material is in tension. For such a material, the stress strain relations will be a slight modification of Eq. (9) – (12), making them

$$\begin{bmatrix} \sigma_1 \\ \sigma_2 \\ \sigma_3 \\ \tau_{23} \\ \tau_{13} \\ \tau_{12} \end{bmatrix} = \begin{bmatrix} C_{11} & C_{12} & C_{13} & 0 & 0 & 0 \\ C_{12} & C_{11} & C_{13} & 0 & 0 & 0 \\ C_{13} & C_{13} & C_{33} & 0 & 0 & 0 \\ 0 & 0 & 0 & C_{44} & 0 & 0 \\ 0 & 0 & 0 & 0 & C_{44} & 0 \\ 0 & 0 & 0 & 0 & 0 & C_{66} \end{bmatrix} \cdot \begin{bmatrix} \epsilon_1 \\ \epsilon_2 \\ \epsilon_3 \\ \gamma_{23} \\ \gamma_{13} \\ \gamma_{12} \end{bmatrix} \quad (13)$$

$$\begin{bmatrix} \varepsilon_1 \\ \varepsilon_2 \\ \varepsilon_3 \\ \gamma_{23} \\ \gamma_{13} \\ \gamma_{12} \end{bmatrix} = \begin{bmatrix} S_{11} & S_{12} & S_{13} & 0 & 0 & 0 \\ S_{12} & S_{11} & S_{13} & 0 & 0 & 0 \\ S_{13} & S_{13} & S_{33} & 0 & 0 & 0 \\ 0 & 0 & 0 & S_{44} & 0 & 0 \\ 0 & 0 & 0 & 0 & S_{44} & 0 \\ 0 & 0 & 0 & 0 & 0 & S_{66} \end{bmatrix} \begin{bmatrix} \sigma_1 \\ \sigma_2 \\ \sigma_3 \\ \tau_{23} \\ \tau_{13} \\ \tau_{12} \end{bmatrix} \quad (14)$$

$$E_1 = E_2, \quad G_{13} = G_{23} \quad \text{and} \quad \nu_{32} = \nu_{31} \quad (15)$$

and

$$\begin{bmatrix} \varepsilon_1 \\ \varepsilon_2 \\ \varepsilon_3 \\ \gamma_{23} \\ \gamma_{13} \\ \gamma_{12} \end{bmatrix} = \begin{bmatrix} \frac{1}{E_1} & \frac{-\nu_{21}}{E_1} & \frac{-\nu_{31}}{E_3} & 0 & 0 & 0 \\ \frac{-\nu_{12}}{E_1} & \frac{1}{E_1} & \frac{-\nu_{31}}{E_3} & 0 & 0 & 0 \\ \frac{-\nu_{13}}{E_1} & \frac{-\nu_{13}}{E_1} & \frac{1}{E_3} & 0 & 0 & 0 \\ 0 & 0 & 0 & \frac{1}{G_{13}} & 0 & 0 \\ 0 & 0 & 0 & 0 & \frac{1}{G_{13}} & 0 \\ 0 & 0 & 0 & 0 & 0 & \frac{1}{G_{12}} \end{bmatrix} \begin{bmatrix} \sigma_1 \\ \sigma_2 \\ \sigma_3 \\ \tau_{23} \\ \tau_{13} \\ \tau_{12} \end{bmatrix} \quad (16)$$

Close examination of Eqs. (13), (15) and (16) reveals that the number of independent constants in the compliance or stiffness matrix is six. It is thus possible to characterize the material provided that the six independent constants, viz., E_1 , ν_{21} , ν_{31} , E_3 , G_{13} and G_{12} are known.

To obtain the values of these six independent constants, suitable experiments have been conducted. The experiments have been conducted in such a way as to obtain the numerical values of the moduli from their basic equations.

II. 1. Material modeling

As explained earlier, it is necessary to determine six independent constants, i.e., the Young's moduli E_1 and E_3 , the Poisson's ratios ν_{21} and ν_{31} , and the shear moduli G_{13} and G_{12} to define its compliance or stiffness matrix completely. The basic equations that were used to determine these constants are explained below.

Shear moduli

The shear modulus in any plane of the material can be determined by performing a torsion test on a shaft made of that material and using the torsion formula [16]:

$$\phi = \frac{T \cdot L}{G \cdot J} \quad (17)$$

where,

ϕ is the angle of twist in rad,

T is the torque in N.m

L is the length of the shaft in m,

G is the shear modulus in Pa (N/m^2), and

J is the polar moment of inertia in m^4 .

Thus, shear modulus can be calculated as:

$$G = \frac{180 \cdot T \cdot L}{\pi \cdot J \cdot \theta} \quad (18)$$

where, θ is the angle of twist in deg.

Young's moduli

The Young's moduli can be determined by carrying out tensile tests on suitable deposited specimens. The tensile test is used to obtain the stress vs. longitudinal strain curve in that direction, thus enabling us to calculate the Young's modulus in that direction as the slope of the elastic portion of the curve.

$$E = \frac{\Delta\sigma}{\Delta\varepsilon} \quad (19)$$

The tests can be performed in the 1, 2 and 3 principal directions to obtain the corresponding Young's moduli E_1 , E_2 and E_3 .

Poisson's ratios

The Poisson's ratios can be determined by simultaneously measuring the strain in the lateral direction along with the longitudinal strains while doing the tensile tests. If both the longitudinal as well as the lateral strain at a given stress value in the elastic limit are known, the Poisson's ratio can be calculated as:

$$\nu_{ij} = \frac{\varepsilon_j}{\varepsilon_i} \quad (20)$$

With this knowledge of the basic equations of the mechanical constants, torsion and tensile tests have been done on various specimens to determine the constants.

II. 2. Torsion test

Torsion tests have been conducted on an Adelaide load frame (Fig. 5). The load frame had capabilities of performing both torsion and axial tests. The machine was controlled using a LabVIEW virtual instrument (VI). The angular displacement was measured in radians and the torque was measured in in-lb. The rate of angular displacement could be controlled and the corresponding torque value could be obtained while testing. Thus, the machine gave us two outputs – angular displacement in radians and the corresponding torque in in-lb. To check the calibration of the load cell, torsion tests were carried out on aluminum specimens. It was established that the modulus value obtained from the tests had to be multiplied by a correction factor of 1.6 to obtain the actual value of the shear modulus of the material.

The specimens were fabricated in accordance with the ASTM standard E 143 [17] which is the standard test method for shear modulus at room temperature. The standard requires that “specimens in the form of solid cylinders be straight and of uniform diameter for a length equal to the gage length plus two to four diameters”, and the gage length be at least four diameters and the gripping length be at least one diameter on either side, i.e., the total length be equal to a minimum of four diameters plus two diameters. The machine had one inch collet chucks in which the specimens could be gripped. Thus, the specimens that were manufactured had to have a diameter of one inch, which meant that the specimens that were fabricated were six inches tall.



Fig. 5. The Adelaide load frame on which torsion tests were conducted

The specimens were fabricated in three different specimens to obtain the corresponding shear modulus values. The specimens whose longitudinal axes were parallel to the x-axis of the machine (*TR1*) and the specimens whose longitudinal axes were at an angle of 135° to the x-axis of the machine on the *xy* plane (*TR2*) were used to obtain the value of G_{23} , and thus, G_{13} , since they are equal to one another. The specimens whose longitudinal axes were parallel to the z-axis of the machine (*TR3*) were used to obtain the value of G_{12} . Equation (18) was used to experimentally determine the shear moduli for all the specimens. The different specimen configurations are as shown in Fig. 6.

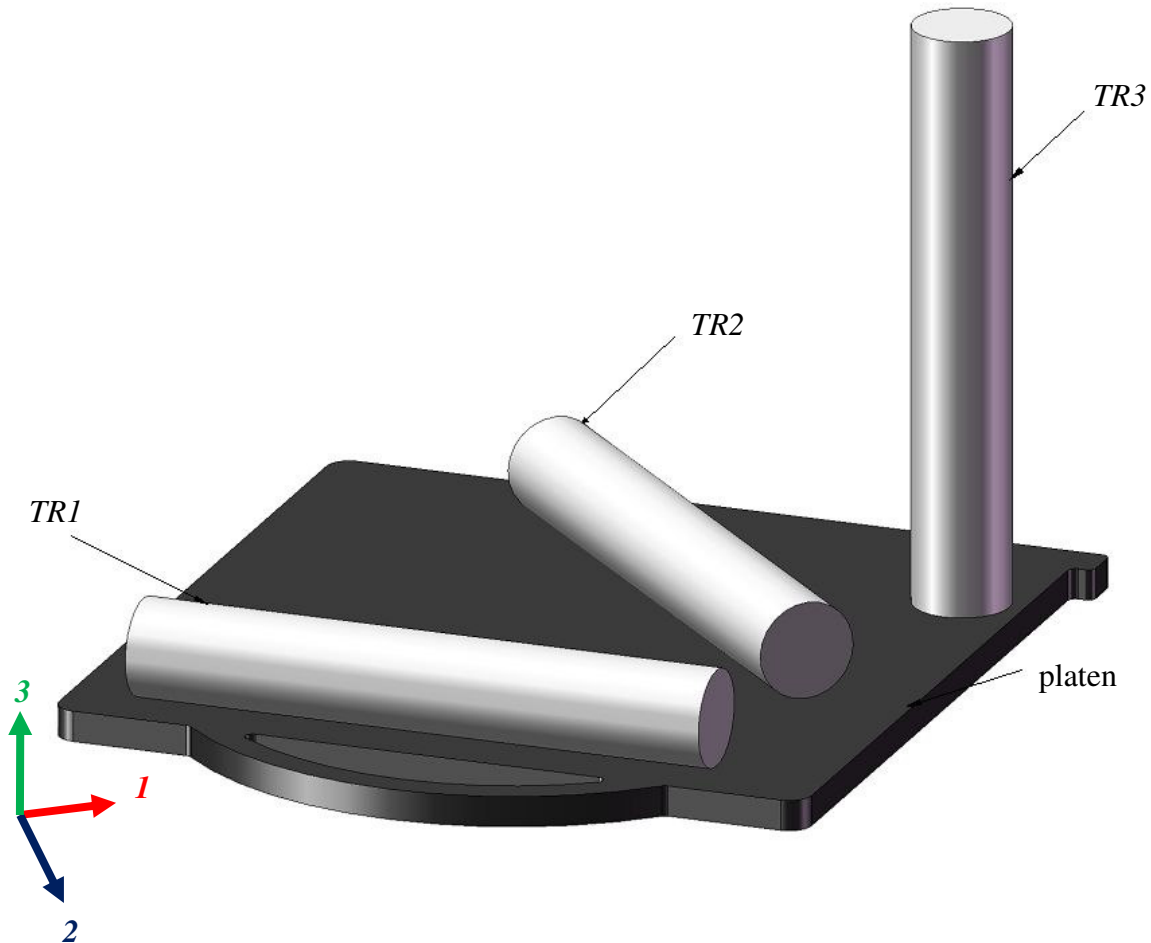


Fig. 6. A schematic of the torsion test specimen configurations

The test was also conducted in accordance with the ASTM standard [17]. The specimen was gripped firmly between the collet chucks and the specimen was twisted at a constant rate and the corresponding torque values were recorded. The testing rate was 0.5 rad/min. A close up of the machine while testing a specimen is shown in Fig. 7. The torque values were converted to SI units (N-m) and a graph of Torque/Polar moment of inertia (T/J) vs. angle of twist/gage length (ϕ/L) was plotted for all specimens. Its shear modulus was ob-

tained as the linear portion of the curve and the resulting slope was multiplied by the correction factor (1.6).



Fig. 7. Close up of the torsion test

II. 3. Tensile tests

Tensile tests have been performed on an MTS 100 KIP load frame (Fig. 8). Three sets of reading were obtained from the tests, viz., the load value, the axial strain value and the transverse strain value. A 1000 lb external load cell was used to obtain more accurate load values, and a biaxial extensometer was used to obtain simultaneous axial and transverse strain readings. The load frame was capable of giving out only two signals at a time. So, the configuration was set up in such a way that the machine gave us axial and transverse strain signals. The load signal was obtained from an external data acquisition device that was used in conjunction with LabVIEW. The whole process of setting up a new configuration to perform these tensile tests to acquire biaxial data involved several stages.

The first stage involved calibrating the load cell to read out load values in kg through the LabVIEW virtual instrument (VI). The laboratory in which these tests were conducted had a previously created VI that read load values from the load cell. Calibration of the load cell was carried on a load cell calibrating frame. Different weights were added to a weight hanger which was connected to the load cell and the subsequent load values were entered in the VI to form a calibration table for the load cell. The VI then used this table to interpolate or extrapolate the in-lying values to give out the load reading. Once the load cell was calibrated, attention was focused towards the extensometer.



Fig. 8. The MTS 100 KIP load frame

The second stage of conducting the tensile tests involved calibrating the extensometer. The extensometer used to carry out the tensile tests was an MTS 632.85 biaxial extensometer (Fig. 9). Calibration had to be done on this to ensure accuracy of the measurements. The MTS 632.85 biaxial extensometer manual was used for the calibration [18]. According to the manual, an extensometer calibrator and two kinds of specimen blocks were needed to calibrate the extensometer. Although the exact same extensometer calibrator was not present in the lab, there was a similar one (Fig. 10) that could be used to serve the same purpose provided we had the correct specimen blocks (Fig. 11). The specimen blocks were designed and machined in the Mechanical Engineering Department Machine Shop. They were made of brass. Two sets of specimen blocks were machined; one for calibrating the longitudinal strain measurements and one for calibrating the transverse strain measurements. This had to be done because of the different ways in which the extensometer has to be fixed to the blocks while calibrating it. The extensometer calibrator is basically a micrometer with a least count of 0.0001", i.e., the smallest dimension that can be measured using the micrometer is 0.0001". The specimen blocks are secured in the slots provided for them in the extensometer calibrator. The axial strain specimen block was secured to the slots and the extensometer was attached to the block. The MTS load frame had its own proprietary software that gave us the strain readings from the axial and transverse sensors. The axial strain reading was zeroed after removing the zero set pins from the extensometer. The micrometer head was then moved by a known distance and the corresponding axial strain reading was observed. The Gain/Delta-K was then suitably adjusted to correct any errors in the reading. This procedure was repeated by displacing the micrometer head by many known distances until the extensometer readings

were accurate. The same procedure was followed to calibrate the transverse strain sensor also; the only difference being that since the gauge length of the transverse strain sensor was variable while the gauge length of the axial strain sensor is fixed at one inch, the specimen blocks were secured to the calibrator such that the distance between the upper surface of the top block and the bottom surface of the bottom block was equal to the current gauge length of the transverse strain sensor. The strain gauge was calibrated to reach both strains accurately to 0.001 mm/mm. Upon calibrating the strain gauge, the calibration parameters were saved in the software.

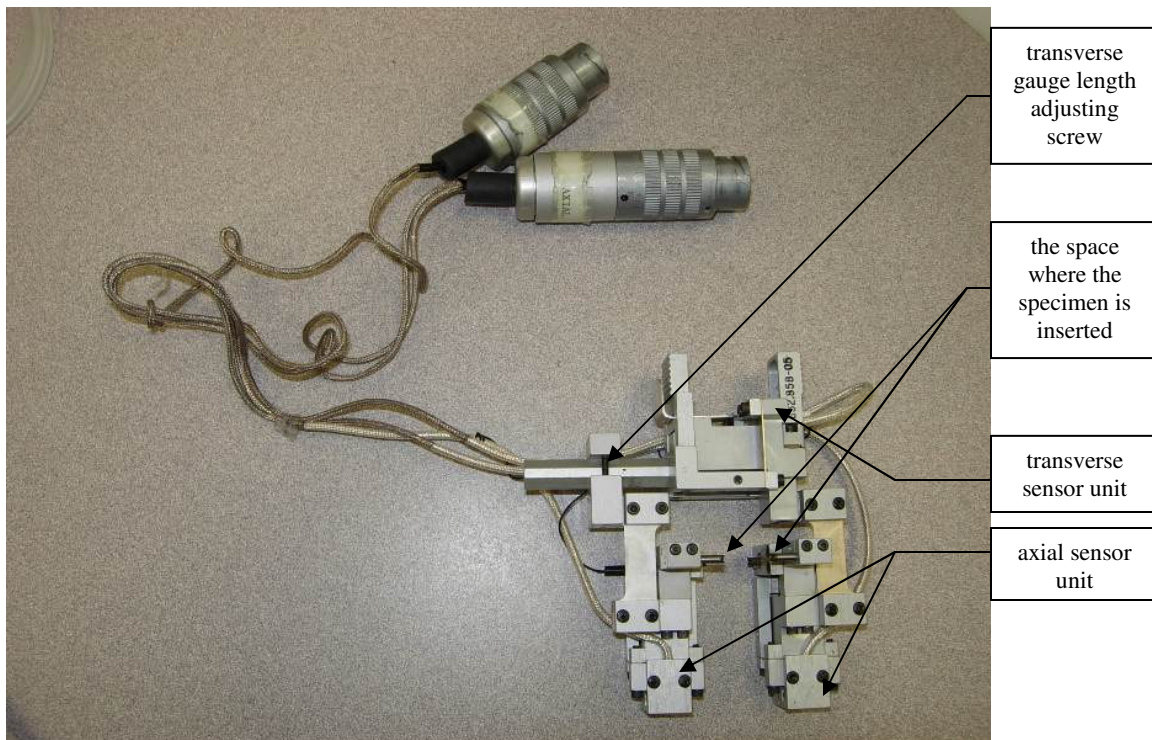


Fig. 9. The MTS 632.85 biaxial extensometer

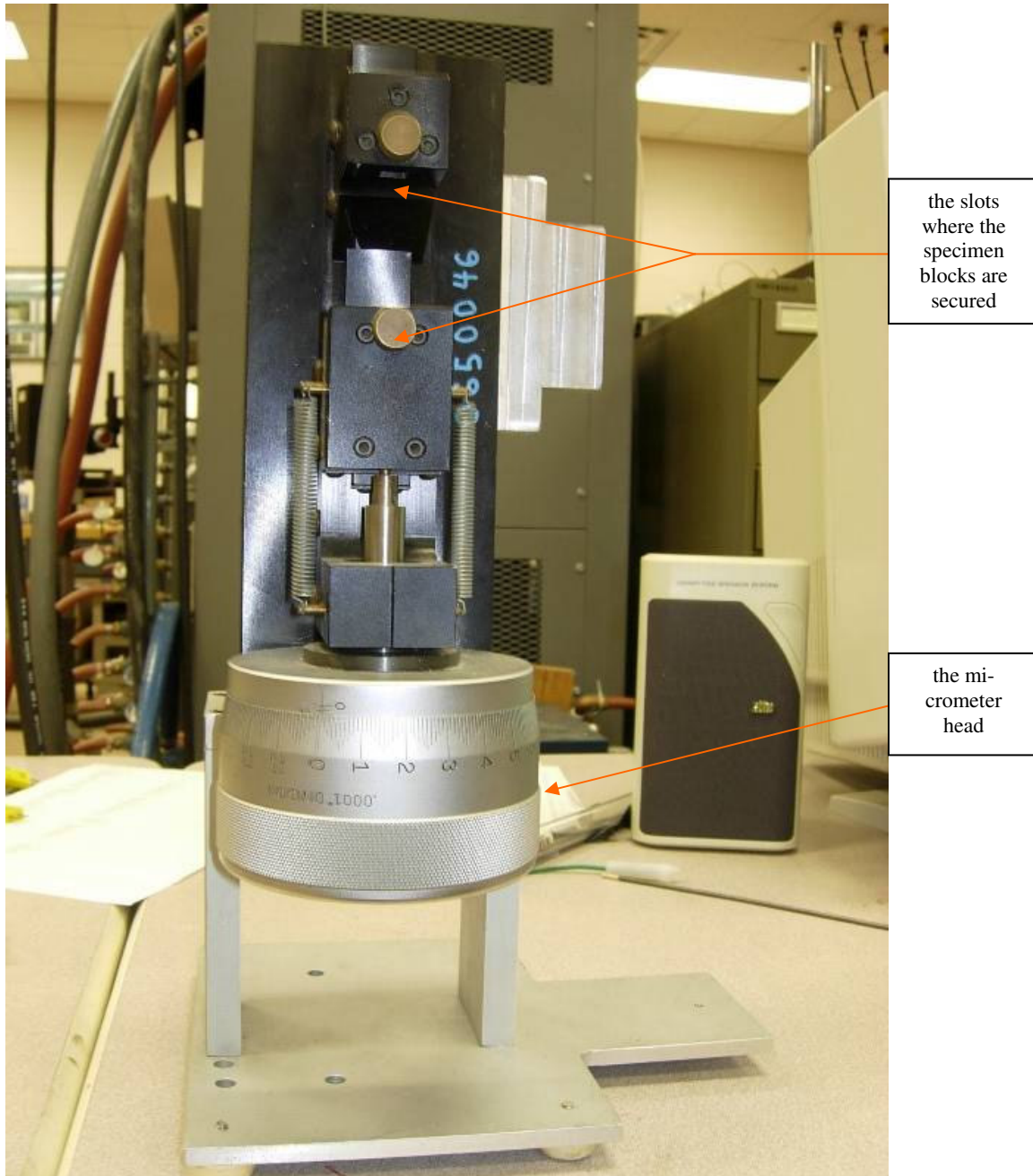


Fig. 10. The extensometer calibrator

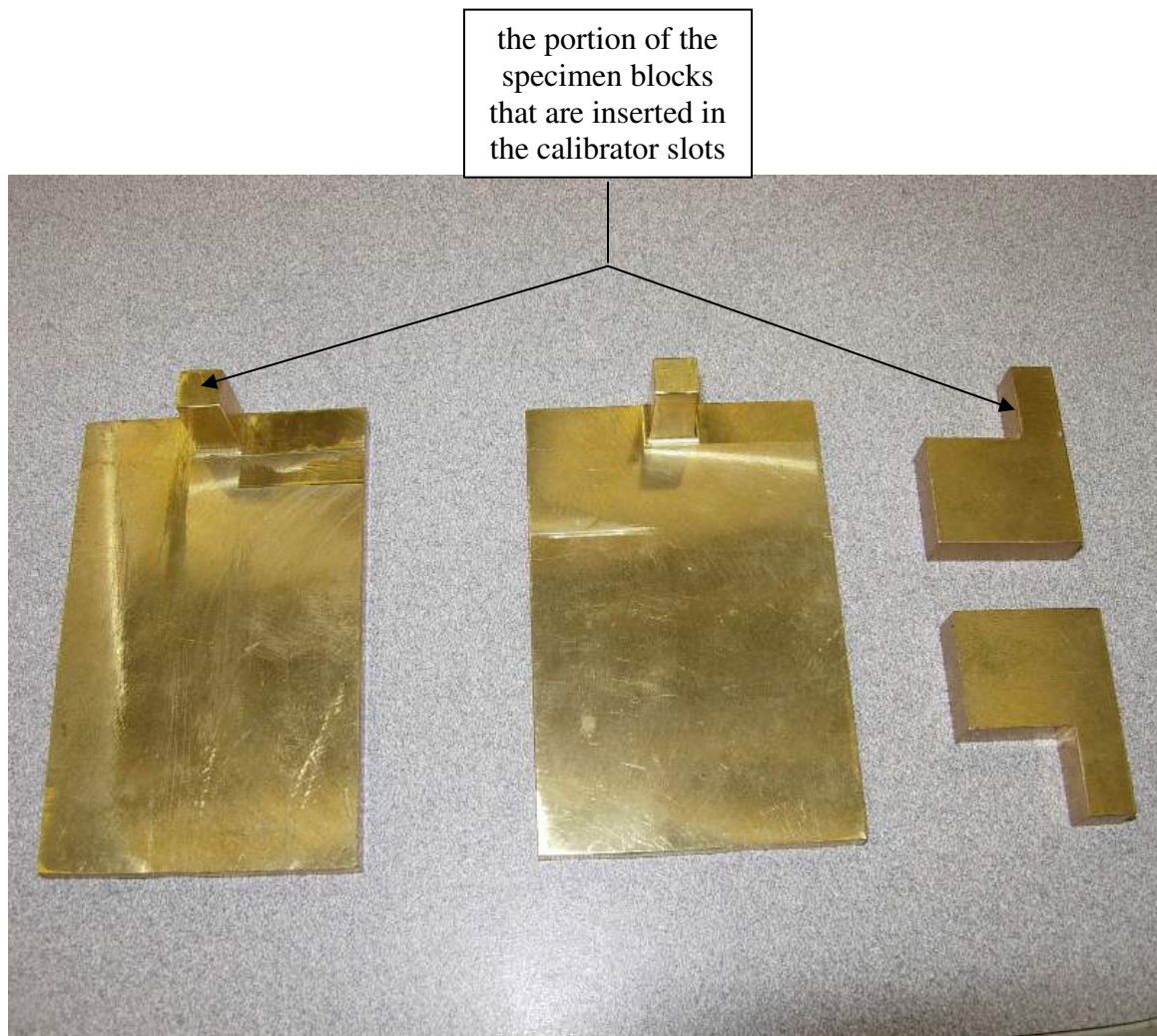


Fig. 11. The specimen blocks that were used to calibrate the extensometer. The 2 large ones on the left were used to calibrate the transverse strain readings and the 2 smaller ones on the right were used to calibrate the longitudinal strain readings

The tensile test specimens were fabricated in accordance with the ASTM D638 standard test method for tensile properties of plastics [19]. The specimens were fabricated in various configurations as it was done for the torsion test specimens to get the mechanical properties in different directions. The specimens deposited on the xy plane of the machine and the specimens that were deposited along the z -axis of the machine were of type I as given in [19]. The vertical specimens were fabricated in accordance with the type I specimens at various inclinations on the xy plane, but most of the specimens turned out to be defective or they got detached from their base and fell down making only a few of them suitable for our experiments. This was because the deposition head hit the parts after it was deposited up to a certain height. The ordering of the deposition was too random which resulted in the deposition head moving haphazardly in all directions. The only two kinds of specimens that did not turn out to be defective were the ones deposited whose lateral axis was inclined at 135° to the x -axis and the ones whose lateral axis was along the y -axis of the machine coordinate system. But enough number of specimens survived for us to conduct the tensile test to determine the corresponding mechanical properties.

The tensile specimens whose longitudinal axes were inclined at 45° to the x -axis ($TN4$) of the machine $[0/90]$ (Fig. 12) gave us the value of E_1 and ν_{12} , the ones whose longitudinal axes were inclined at 135° ($TN5$) $[90/0]$ (Fig. 13) to the x -axis of the machine gave us the value of E_2 and ν_{21} , and the ones whose longitudinal axes were vertical ($TN3.1$ and $TN3.2$) (Figs. 12 and 13) gave us the value of E_3 and the corresponding Poisson's ratio of the material. It should be noted that the results of the $TN4$ and $TN5$ specimens were expected to be approximately the same, and the rotation of the compliance matrix by 45°

about the z-axis (by applying transformation laws) should provide us the values of the moduli of the x-axis ($TN1$) [+45/-45] (Fig. 12) and y-axis ($TN2$) [-45/+45] (Fig. 13). The specimen configurations have been named similar to the torsion test specimen configurations.

The experiments were then conducted in accordance with the guidelines provided by the ASTM standard [19]. It was a displacement controlled test. The axial and transverse strains were collected in mm/mm, whereas the corresponding loads were collected in kg. The loads were then converted to (engineering) stresses by dividing the load values by the original area of cross section of the specimen. Stress vs. axial strain curve was obtained for each specimen and the corresponding elastic modulus was obtained as the slope of the linear elastic portion of the curve. The axial strain and the transverse strain were plotted against the applied load, and the corresponding Poisson's ratio was obtained as the ratio of the slopes of the two straight line curves in accordance with the definition of Poisson's ratio (Eq. (20)). The yield strengths of different specimens were also obtained from their stress vs. axial strain plots.

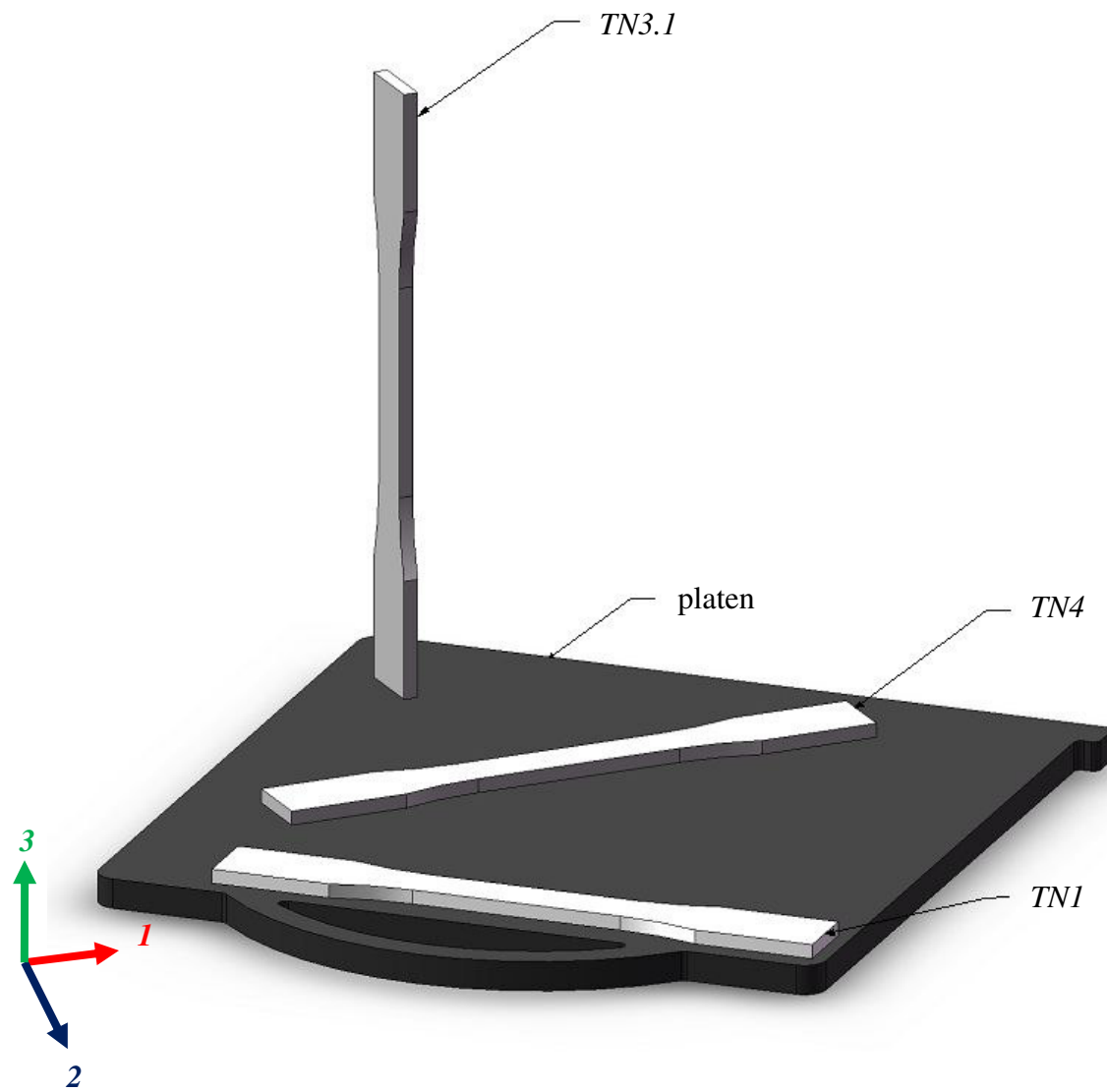


Fig. 12. A schematic of the *TN1*, *TN3.1* and *TN4* tensile test specimen configurations

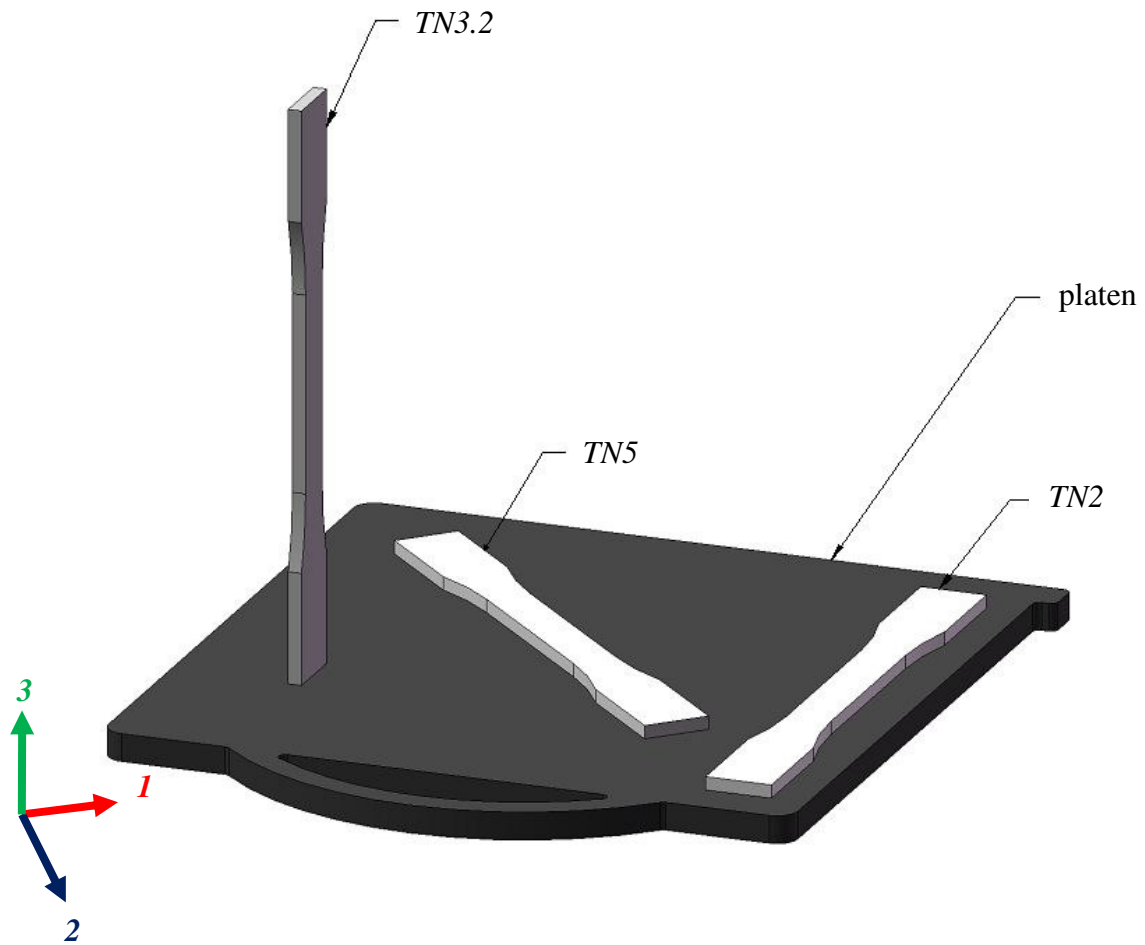


Fig. 13. A schematic of the *TN2*, *TN3.2* and *TN5* tensile test specimen configurations

CHAPTER III

MODELING OF FUSED DEPOSITION MODELING ABS MATERIAL

The material was characterized in the previous chapter. Also, it has been described how, to model the material completely, it is necessary to determine six independent constants. In terms of the mechanical constants of the materials, it was chosen to determine the values of the Young's moduli E_1 and E_3 , the Poisson's ratios ν_{21} , ν_{32} , and the shear moduli G_{13} and G_{12} to define the compliance and stiffness matrices completely.

III. 1. Torsion tests

The torsion tests were carried out as described in the previous chapter. The specimens that were fabricated for the torsion were circular shafts that were 6 inches long and had a diameter of 1 inch. The diameter was chosen as 1 inch because the torsion load frame on which the torsion experiments were performed had collet chucks that had a diameter of 1 inch. The test was a rate controlled one with a testing rate of 0.5 rad/min. Since it was a rate controlled test, the torque values corresponding to the angle of twist was obtained and recorded. The experiments were conducted with utmost care to minimize the experimental errors.

A plot of T/J vs. ϕ/L was drawn (hereby referred to as the torsion curve) and the slope of the linear region of the resulting curve was measured to obtain the shear modulus of that configuration in N/m^2 or Pa. Typical torsion curves of the *TR1*, *TR2* and *TR3* specimen configurations are as shown in Fig. 14, Fig. 15 and Fig. 16 respectively. A characteristic

curve used to measure the shear modulus of the material is as shown in Fig. 17. The curve shows a y-intercept in its straight line equation. This shows the existence of slack in the equipment. Since only the slope of the curve was of concern and not the actual angles of twist, slack was ignored.

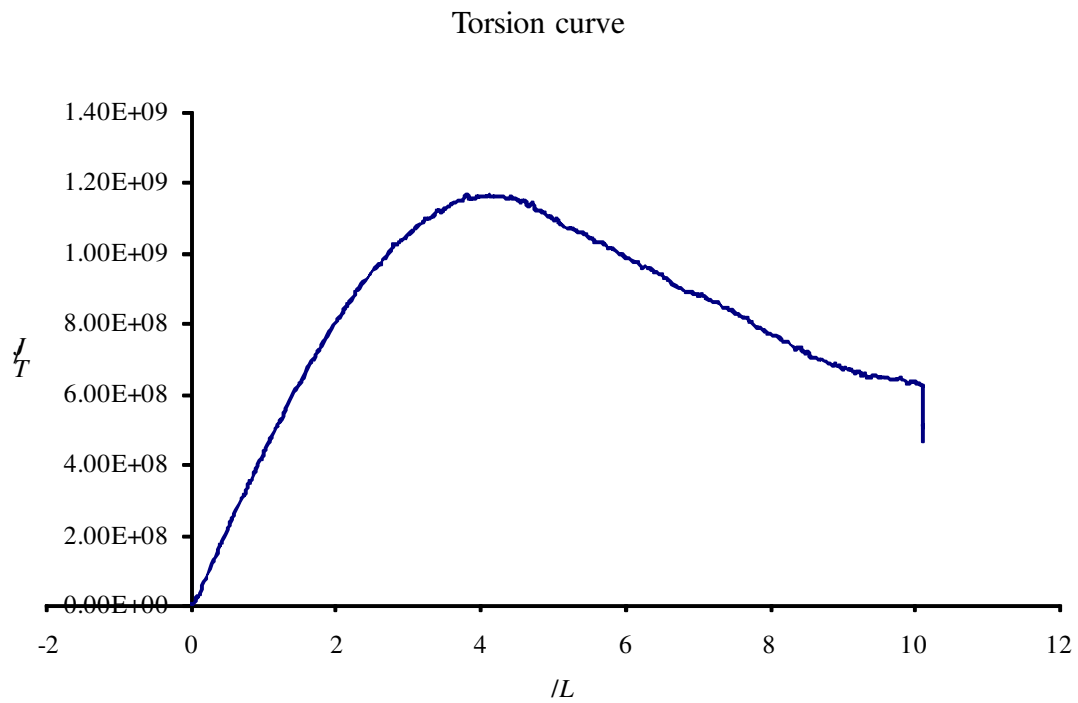


Fig. 14. A typical torsion curve of the *TRI* specimen configuration

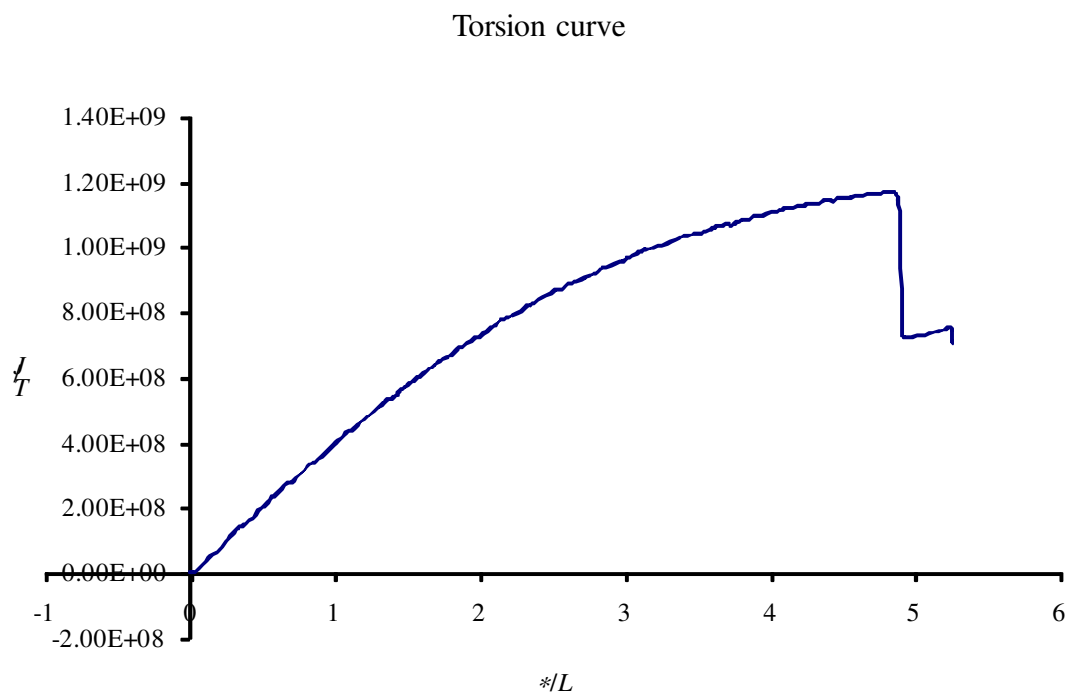


Fig. 15. A typical torsion curve of the *TR2* specimen configuration

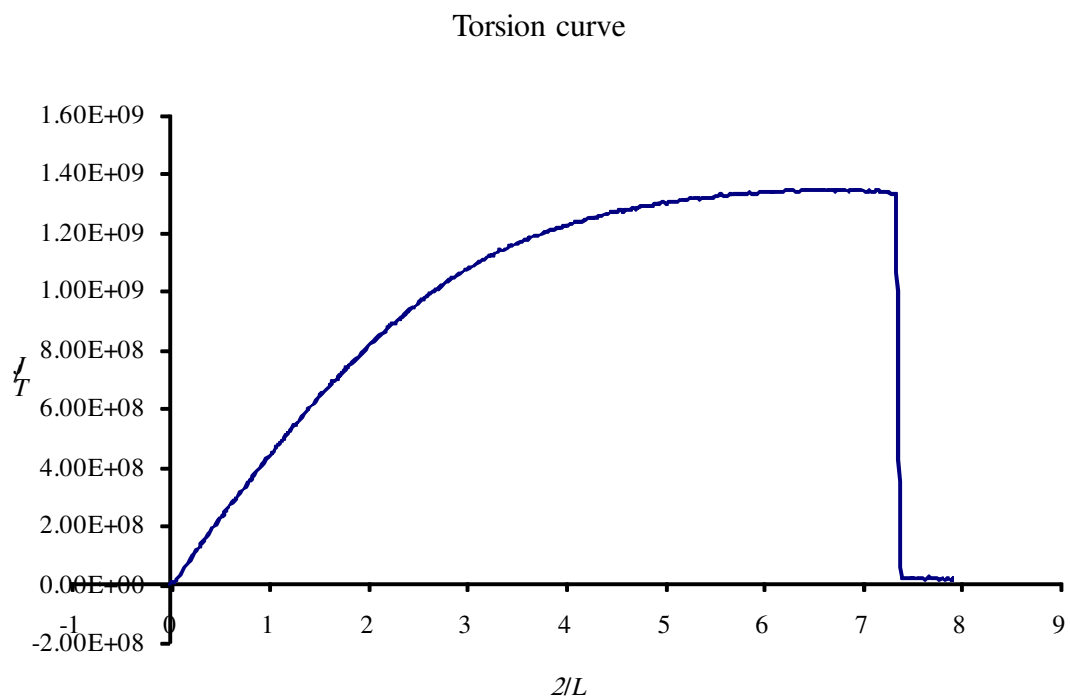


Fig. 16. A typical torsion curve of the *TR3* specimen configuration

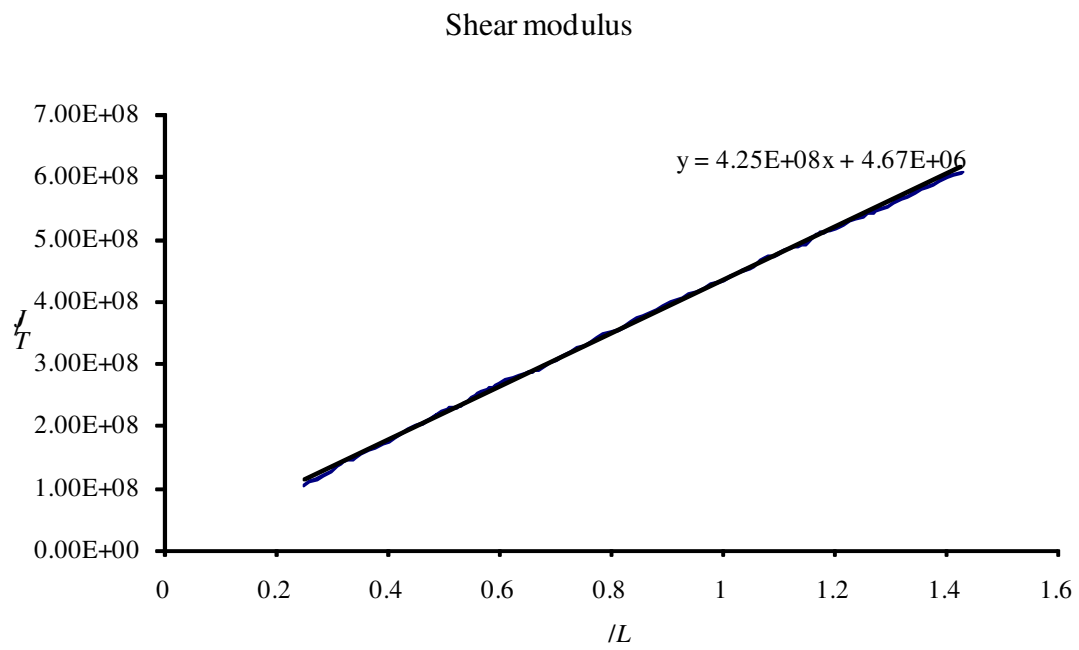


Fig. 17. A characteristic curve used to measure the shear modulus

The torsion tests were conducted on shafts that were fabricated according to the three specimen configurations as shown in Fig. 6. The *TR2* configuration specimens were used to obtain the value of the shear modulus on the plane of its cross section, i.e., G_{13} . Similarly, the *TR3* configuration specimens were used to obtain the value of G_{12} . The *TR1* configuration specimens were fabricated and the torsion test was performed on them too. It was expected that the average shear modulus of these specimens would be approximately equal to the shear modulus of the *TR2* specimens. The shear moduli of all the specimens that were tested for the three specimen configurations are tabulated below in Table 1. The average shear modulus and its standard deviation are also given in Table 1 and the corresponding error bar graph is shown in Fig. 18.

A difference of approximately 8.0% was seen in the average values of shear moduli of the *TR1* and *TR2* specimen configurations. The value of G_{23} was thus calculated as the average of the average values of shear moduli of the *TR1* and *TR2* specimen configurations. Thus the value of G_{23} was 645 MPa with a standard deviation of 5.8%. The value of G_{12} obtained from the experiments was 676 MPa.

Table 1. The shear moduli of the samples that underwent the torsion test, the average shear modulus of each specimen configuration and the standard deviation of the average moduli (Note. The *TR3* specimen configurations had only four specimens that were usable to measure the shear modulus)

<i>Specimen configuration</i>	<i>TR1</i>	<i>TR2</i>	<i>TR3</i>
Shear modulus (MPa)	696	622	683
	672	604	697
	702	629	644
	614	615	680
	678	621	
Average shear modulus (MPa)	672	618	676
Standard deviation	35	9	23

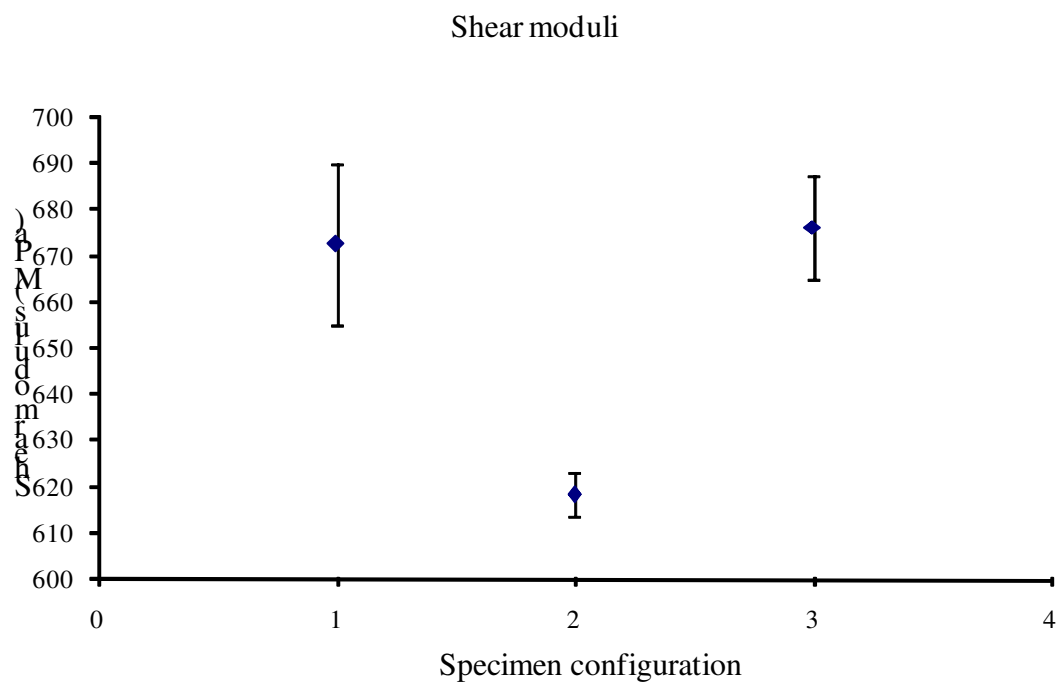


Fig. 18. Shear moduli of all specimen configurations

III. 2. Tensile tests

The tensile tests were conducted as described in the previous chapter. The specimens were fabricated according to the specimen dimension guidelines provided in [19]. Type I specimen was chosen from among the various types prescribed in [19]. Type I specimen was chosen because according to [19], “Type I specimen is the preferred specimen and shall be used where sufficient material having a thickness of 7 mm [0.28 in.] or less is available” for all rigid and semirigid plastics.

As described in the previous chapter, the tensile tests were performed on an MTS load frame (100 kip). A 2000 lb external load cell was used to obtain the load values instead of the in-built load cell to get more accurate readings. An MTS 632.85 biaxial extensometer was used to obtain the longitudinal and the transverse strain readings corresponding to the load readings. Due to the limitations on the number of signals that could be simultaneously obtained from the load frame (it was two, in this case), an external DAQ via LabVIEW was used to obtain the load values. An existing VI was slightly modified to suit the purpose [20] of these experiments. Both the load cell and the extensometer needed calibration.

The load and strains data for a specimen obtained from the tests were assembled together and a stress-strain curve for that specimen was drawn. A linear trend line was plotted for the linear elastic region of the curve and its slope was measured to obtain the value of Young’s modulus of the specimen in the direction of its loading. Plots of the axial strain

and the transverse strain obtained from the biaxial extensometer were plotted against the applied load to obtain the corresponding Poisson's ratio. A linear trend line was plotted for both the curves to obtain their corresponding slopes. The Poisson's ratio of the material was calculated as the slope of transverse strain curve divided by the slope of the axial strain curve.

The tensile tests were performed on the six specimen configurations that are shown in Figs. 12 and 13. The *TN4* specimens were used to obtain the values of the Young's modulus along its longitudinal axis and the corresponding Poisson's ratio, i.e., E_1 and ν_{12} of the material. Similarly, the *TN5* specimens were used to obtain the values of E_2 and ν_{21} , the z-axis specimens (*TN3.1* and *TN3.2*) were used to obtain the value of E_3 and the corresponding Poisson's ratio ν_{32} . The values of E_1 and E_2 were expected to be approximately equal because of the material behavior. The Young's moduli values obtained from testing the *TN1* and *TN2* were expected to be approximately equal to the values of the corresponding moduli obtained by rotating the material by 45° about axis 3.

The stress-strain curves of the specimens were also used to obtain the tensile strengths of the various specimen configurations. It was seen that all the specimens exhibited a definite linear elastic region. The curve of the plastic region of the material was different for different configurations. The characteristic stress-strain curves for all the specimen configurations are as shown in Figs. 19 - 24.

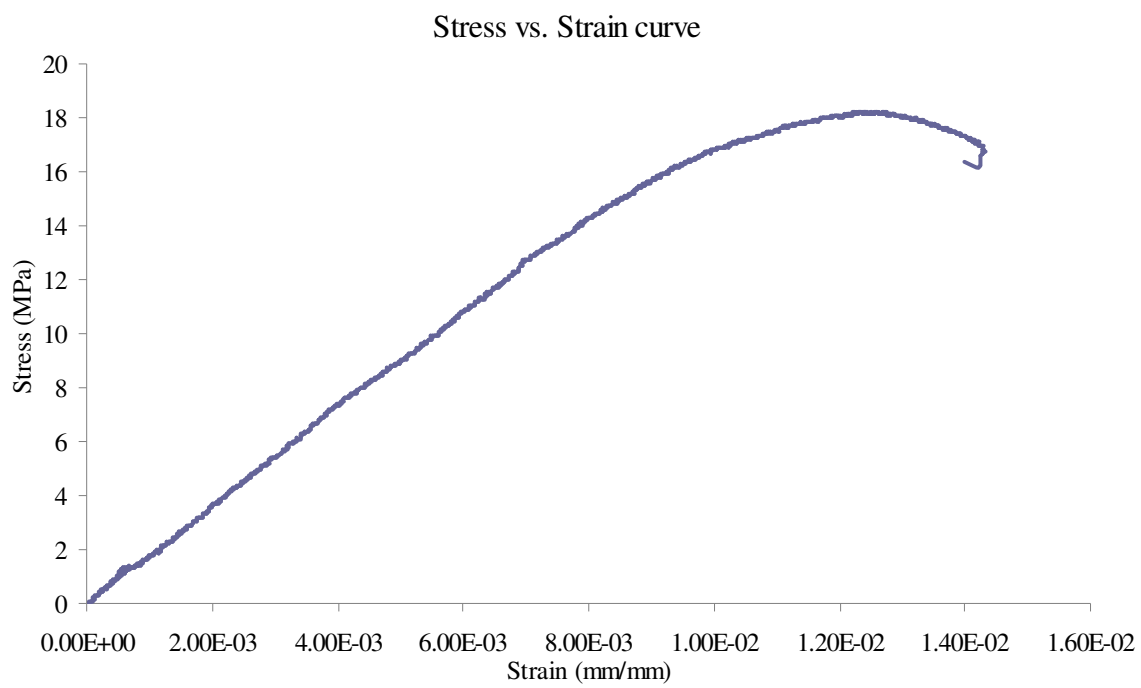


Fig. 19. A characteristic stress-strain curve of the *TN4* specimen configuration

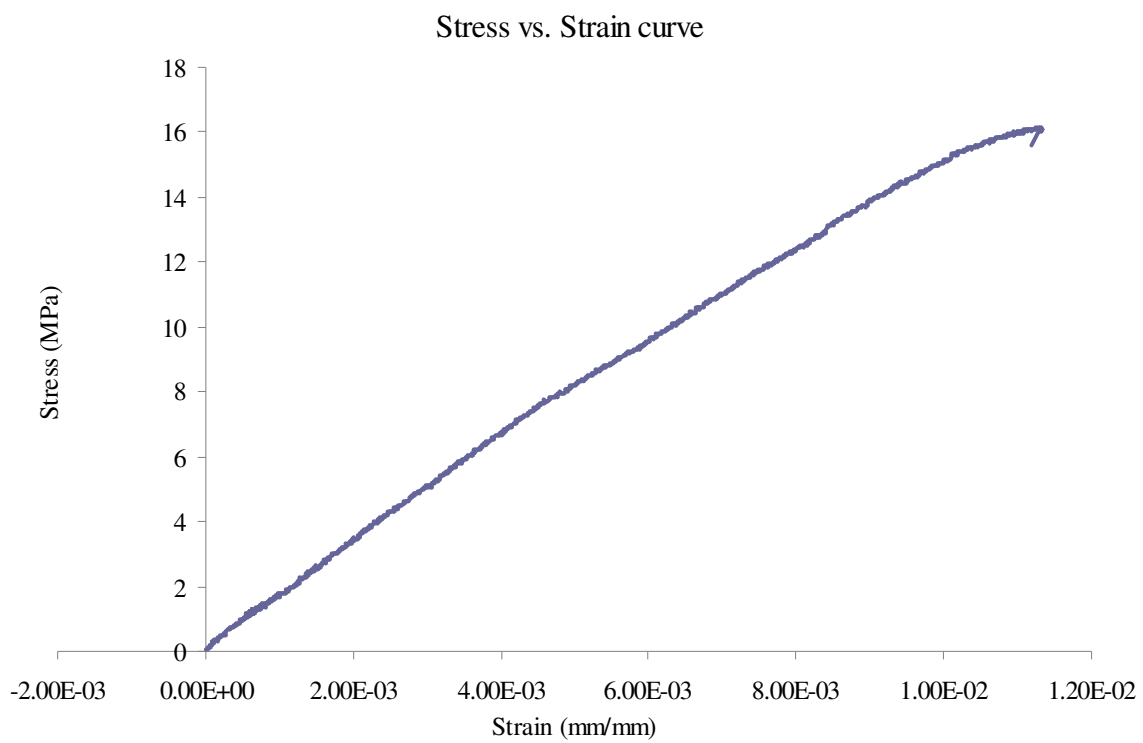


Fig. 20. A characteristic stress-strain curve of the *TN5* configuration

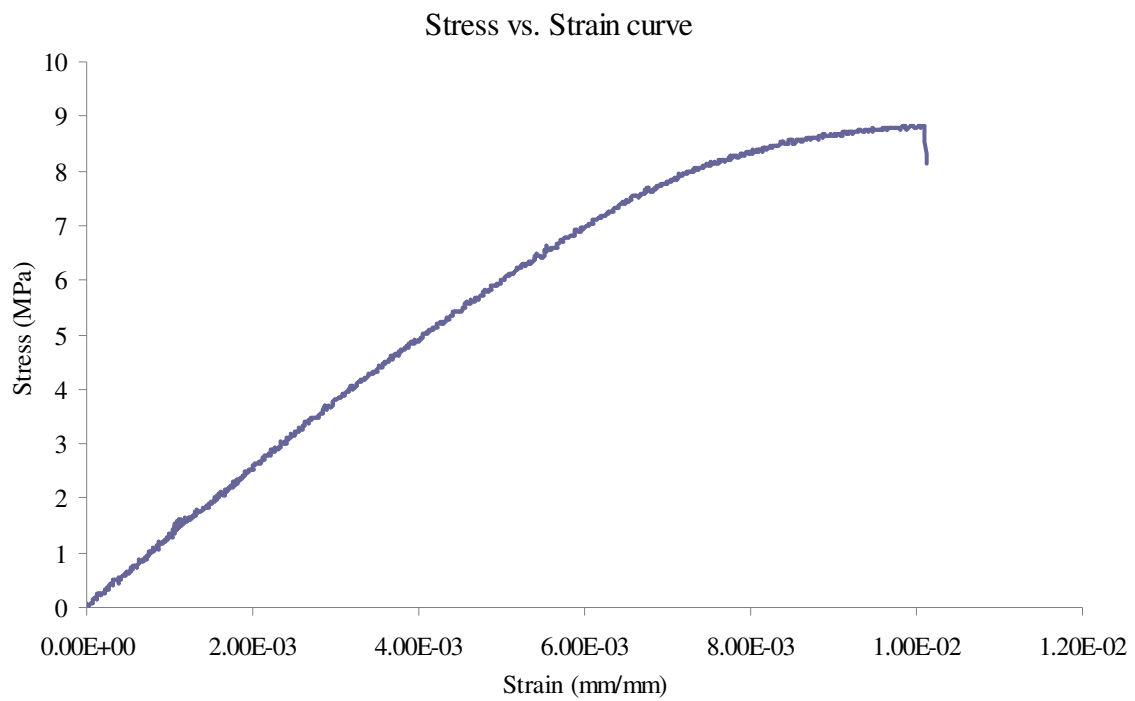


Fig. 21. A characteristic stress-strain curve of the *TN3.1* specimen configuration

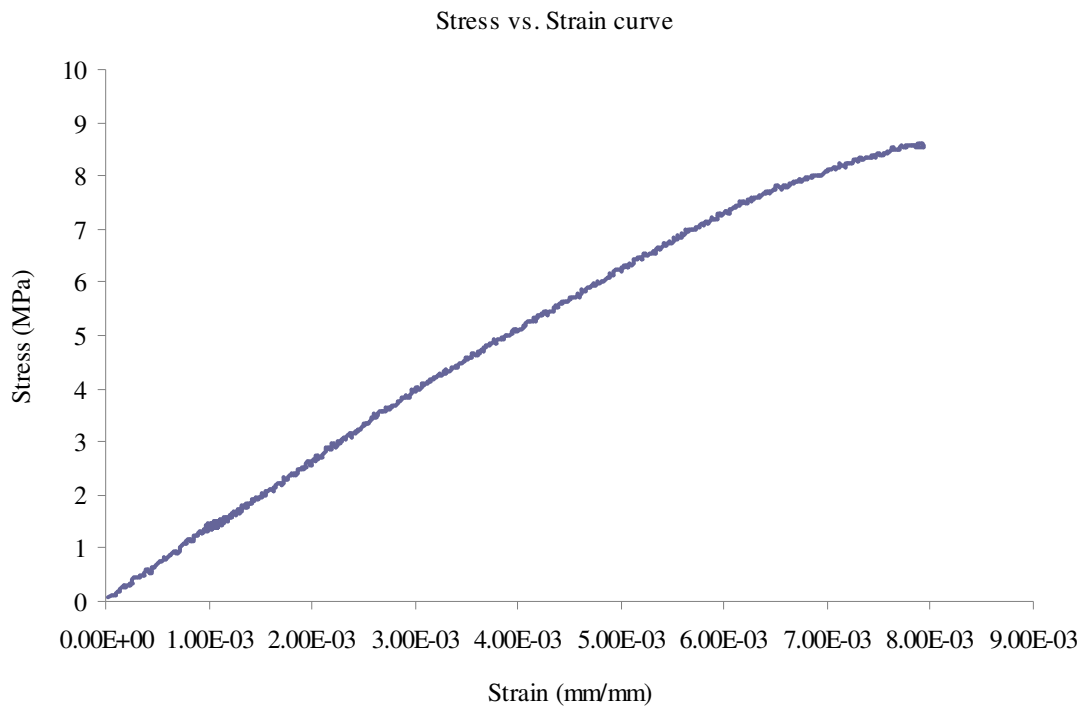


Fig. 22. A characteristic stress-strain curve of the *TN3.2* specimen configuration

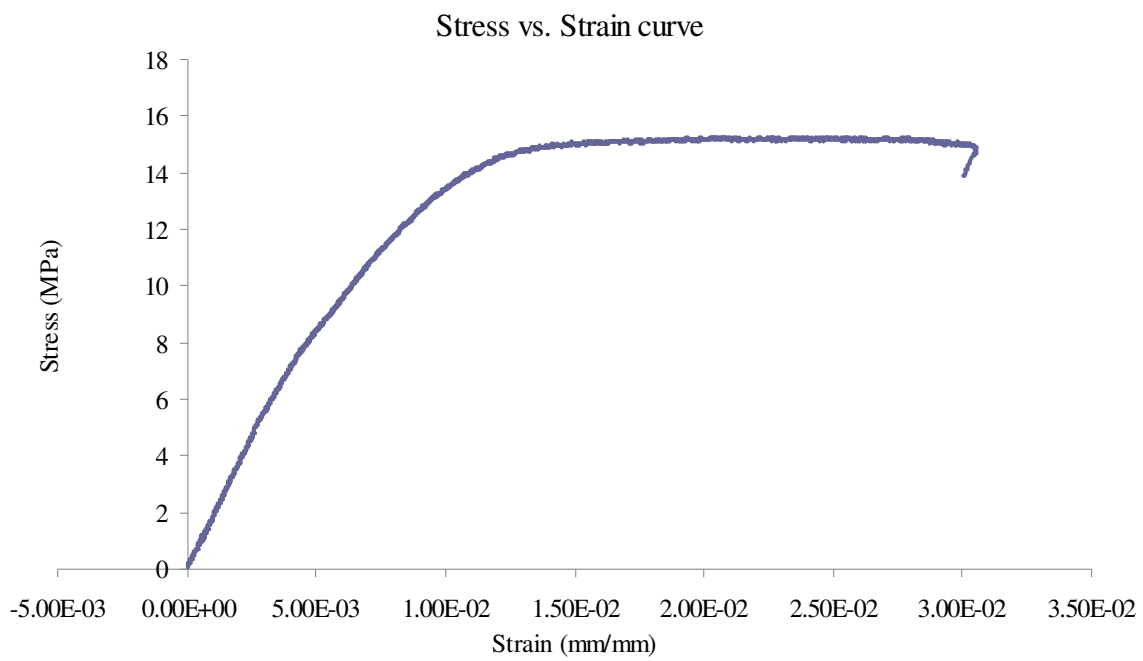


Fig. 23. A characteristic stress-strain curve of the *TN1* configuration

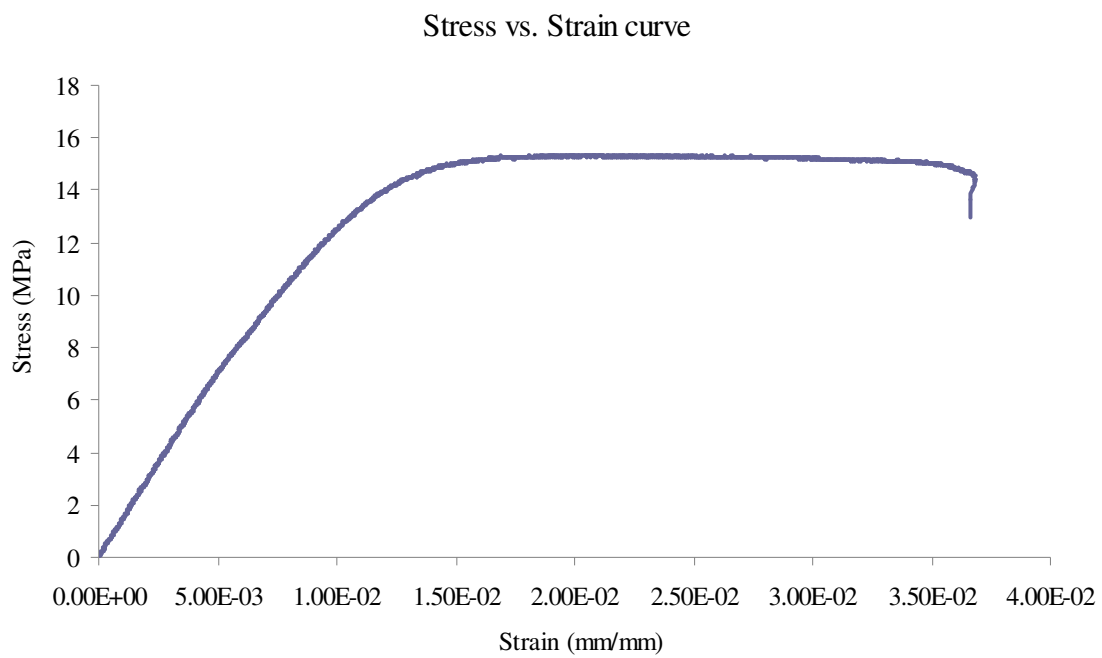


Fig. 24. A characteristic stress-strain curve of the *TN2* configuration

Characteristic curves that were used to calculate the Young's modulus and the Poisson's ratio of the specimen are as shown in Figs. 25 and 26 respectively.

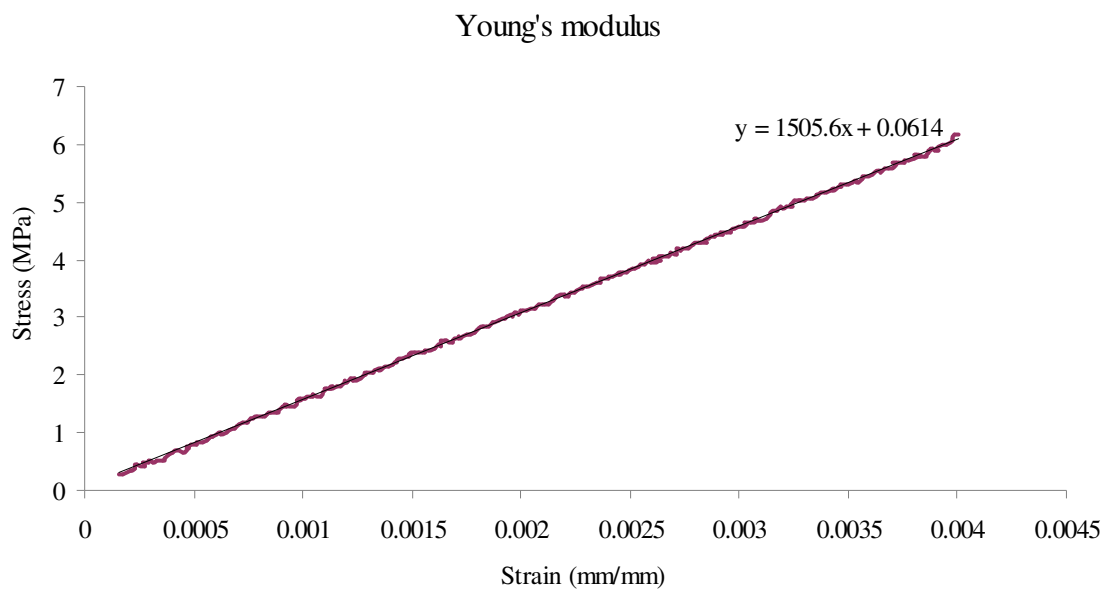


Fig. 25. A characteristic plot used to calculate the Young's modulus

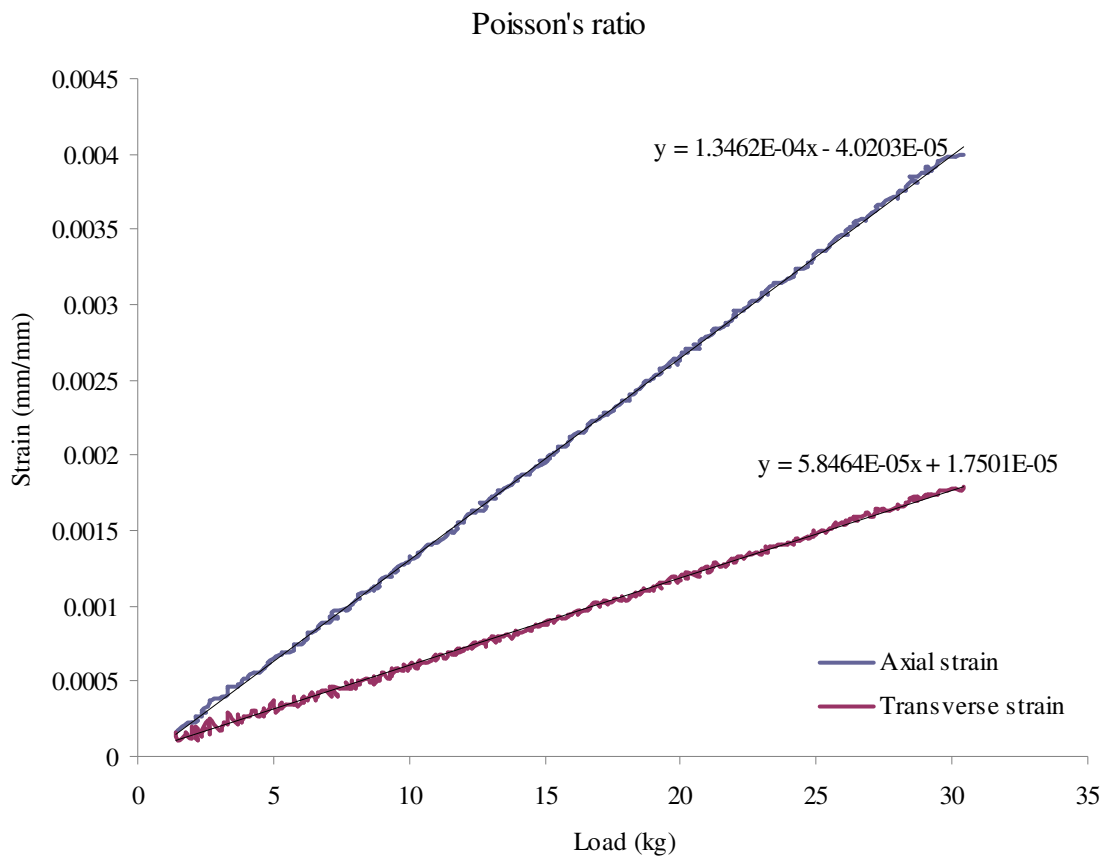


Fig. 26. A characteristic plot used to calculate the Poisson's ratio

The Young's moduli of all the tensile test specimen configurations are as shown in Table 2 and Fig. 27. The average Young's modulus of a configuration and its standard deviation are also given.

Table 2. The Young's moduli of the samples that underwent the tension test, the average Young's modulus of each specimen configuration and the standard deviation of the average moduli (Note. Blank cells represent the fact that there was no that numbered specimen for that specific specimen configuration.)

<i>Specimen configuration</i>	<i>TN1</i>	<i>TN2</i>	<i>TN3.1</i>	<i>TN3.2</i>	<i>TN4</i>	<i>TN5</i>
Young's moduli (MPa)	1454	1490	1249	1230	1734	1640
	1590	1464	1183	1212	1606	1591
	1540	1420	1173	1235	1751	1502
	1577	1441	1152	1240	1811	1670
	1560	1505		1105	1456	1599
	1508	1408				
Average (MPa)	1538	1455	1189	1204	1672	1600
Standard deviation	50	39	42		142	64

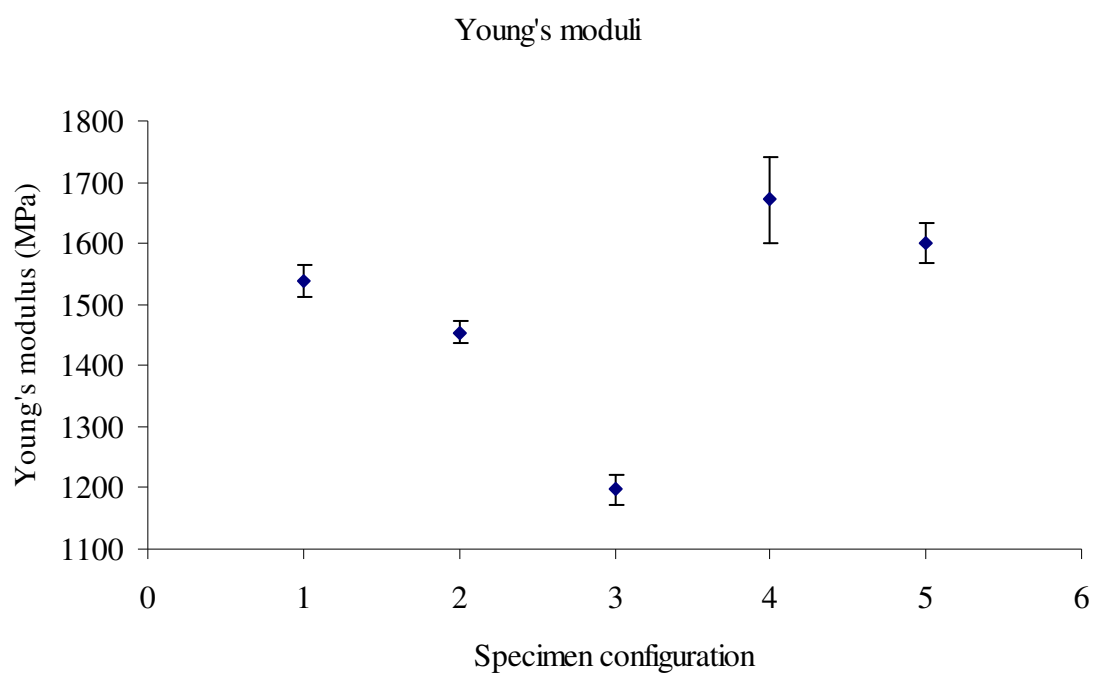


Fig. 27. Young's moduli of all the specimen configurations

The Poisson's ratios of all the tensile test specimen configurations are as shown in Table 3 and Fig. 28. The average Poisson's ratios of a configuration and its standard deviation are also given.

Table 3. The Poisson's ratios of the samples that underwent the tension test, the average Poisson's ratio of each specimen configuration and the standard deviation of the average ratio (Note. The second specimen in the *TN2* configuration was not used to determine the Poisson's ratio because the transverse strain gauge was not zeroed before starting the experiment. Blank cells represent the fact that there was no that numbered specimen for that specific specimen configuration.)

<i>Specimen configuration</i>	<i>TN1</i>	<i>TN2</i>	<i>TN3.1</i>	<i>TN3.2</i>	<i>TN4</i>	<i>TN5</i>
	0.37	0.40	0.36	0.37	0.38	0.40
	0.42		0.40	0.37	0.38	0.39
	0.42	0.41	0.36	0.39	0.37	0.38
Poisson's ratio	0.43	0.42	0.38	0.36	0.38	0.39
	0.38	0.43		0.37	0.41	0.39
	0.41	0.43				
Average	0.41	0.42	0.38	0.37	0.38	0.39
Standard deviation	0.02	0.01	0.02		0.01	0.01

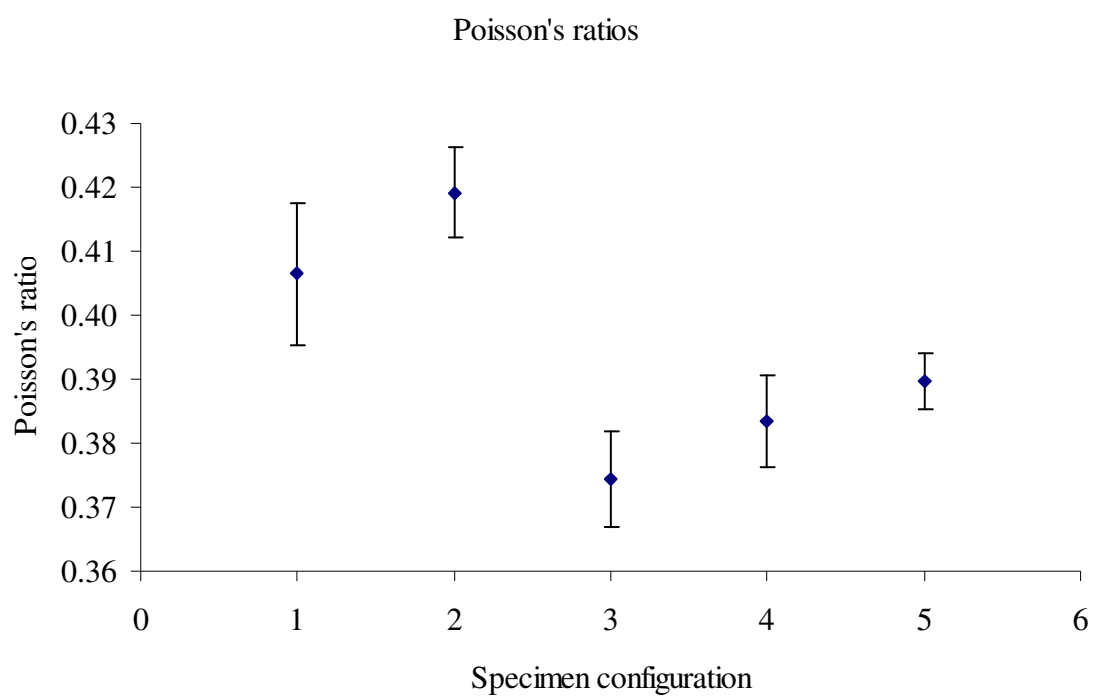


Fig. 28. Poisson's ratios of all the specimen configurations

The tensile (yield) strengths of all the tensile test specimen configurations are as shown in Table 4. The average tensile strength of a configuration and its standard deviation are also given.

Table 4. The tensile strengths of the samples that underwent the tension test, the average tensile strength of each specimen configuration and the standard deviation of the average tensile strength (Note. Blank cells represent the fact that there was no that numbered specimen for that specific specimen configuration.)

<i>Specimen configuration</i>	<i>TN1</i>	<i>TN2</i>	<i>TN3.1</i>	<i>TN3.2</i>	<i>TN4</i>	<i>TN5</i>
	13.0	13.0	7.0	7.0	14.0	14.0
	13.0	13.0	7.0	7.0	14.0	14.0
	13.0	13.0	7.0	7.0	14.0	14.0
Tensile strengths (MPa)	13.0	13.0	7.0	7.0	14.0	14.0
	13.0	13.0		7.0	14.0	14.0
	12.0	13.0				
Average (MPa)	12.8	13.0	7.0	7.0	14.0	14.0
Standard deviation	0.4	0.0	0.0	0.0	0.0	0.0

The Young's modulus E_1 of the material was calculated as the average of the Young's moduli values of the *TN4* and *TN5* configurations. The value of E_1 was thus obtained as:

$$E_1 = \frac{1672 + 1600}{2} \quad (21)$$

$$E_1 = 1636 \text{ MPa}$$

The value of E_1 was thus fixed as 1636 Mpa with a standard deviation of around 3%.

The Young's modulus E_3 of the material was calculated as the average of the Young's moduli values of the *TN3.1* and *TN3.2* configurations. The value of E_3 was thus obtained as:

$$E_3 = \frac{1189 + 1204}{2} \quad (22)$$

$$E_3 = 1197 \text{ MPa}$$

The value of E_3 was thus fixed as 1197 Mpa with a standard deviation of around 1%.

The value of ν_{21} was calculated as the average of the Poisson's ratio values of the *TN4* and *TN5* configurations. The value of ν_{21} was thus obtained as:

$$\nu_{21} = 0.39 \quad (23)$$

The value of ν_{21} was thus fixed as 0.39 with a standard deviation of around 3%.

The value of ν_{32} was calculated as the average of the Poisson's ratio values of the *TN3.1* and *TN3.2* configurations. The value of ν_{32} was thus obtained as:

$$\nu_{32} = 0.37 \quad (24)$$

The value of ν_{32} was thus fixed as 0.37 with a standard deviation of around 2%.

III. 3. Assembly of compliance matrix

The results obtained from the tensile and torsion experiments were assembled together to fill in the numerical values of the components of the compliance matrix (Eq. (16)). As discussed previously, the six independent mechanical constants of the material were determined by the experiments. The dependent constants were calculated by the material property relations as in Eq. (15) and the symmetry of the compliance matrix. Thus,

$$\begin{aligned} E_2 &= E_1 = 1636 \text{ MPa}, \\ E_3 &= 1197 \text{ MPa}, \\ \nu_{21} &= 0.39, \\ \nu_{31} &= \nu_{32} = 0.37, \\ G_{13} &= G_{23} = 645 \text{ MPa}, \\ \text{and} \\ G_{12} &= 676 \text{ MPa} \end{aligned} \quad (25)$$

The above values were plugged into Eq. 11 to obtain the compliance matrix in SI units

as:

$$[S] = \begin{bmatrix} \frac{1}{1636} & -\frac{0.39}{1636} & -\frac{0.37}{1197} & 0 & 0 & 0 \\ \frac{0.39}{1636} & \frac{1}{1636} & -\frac{0.37}{1197} & 0 & 0 & 0 \\ -\frac{0.37}{1197} & -\frac{0.37}{1197} & \frac{1}{1197} & 0 & 0 & 0 \\ 0 & 0 & 0 & \frac{1}{645} & 0 & 0 \\ 0 & 0 & 0 & 0 & \frac{1}{645} & 0 \\ 0 & 0 & 0 & 0 & 0 & \frac{1}{676} \end{bmatrix} \times 10^{-6} \text{ Pa}^{-1}$$

i.e.,

(26)

$$[S] = \begin{bmatrix} 6.1125 & -2.3839 & -3.0911 & 0 & 0 & 0 \\ -2.3839 & 6.1125 & -3.0911 & 0 & 0 & 0 \\ -3.0911 & -3.0911 & 8.3542 & 0 & 0 & 0 \\ 0 & 0 & 0 & 15.5039 & 0 & 0 \\ 0 & 0 & 0 & 0 & 15.5039 & 0 \\ 0 & 0 & 0 & 0 & 0 & 14.7929 \end{bmatrix} \times 10^{-10} \text{ Pa}^{-1}$$

The stiffness matrix of the material was then obtained as the inverse of the compliance matrix, i.e.,

$$[C] = [S]^{-1}$$

$$[C] = \begin{bmatrix} 40.5777 & 28.8079 & 25.6727 & 0 & 0 & 0 \\ 28.8079 & 40.5777 & 25.6727 & 0 & 0 & 0 \\ 25.6727 & 25.6727 & 30.9678 & 0 & 0 & 0 \\ 0 & 0 & 0 & 6.4500 & 0 & 0 \\ 0 & 0 & 0 & 0 & 6.4500 & 0 \\ 0 & 0 & 0 & 0 & 0 & 6.7600 \end{bmatrix} \times 10^8 \text{ Pa} \quad (27)$$

The mechanical material constants w.r.t. the machine coordinate system were $E_x = E_y = 1496$ MPa, $E_z = 1197$ MPa, $\nu_{yz} = 0.41$, $\nu_{zx} = \nu_{zy} = 0.37$, $G_{yz} = G_{xz} = 645$ MPa and $G_{xy} = 676$ Mpa.

As discussed earlier, the modulus of the material when it is rotated by 45° about axis 3 of the material was obtained by transforming the compliance matrix accordingly. The transformed compliance matrix is given by [15]

$$[S'] = [T_\epsilon][S][T_\sigma]^{-1} \quad (28)$$

where,

$[S']$ is the transformed compliance matrix,

$[T_\epsilon]$ is the strain transformation matrix,

$[T_\sigma]$ is the stress transformation matrix, and

$[S]$ is the compliance matrix of the material.

Equation (28) is discussed in more detail in Appendix B. The machine coordinate system was chosen as the principal coordinate system. The machine coordinate system was transformed to yield the global coordinate system, i.e., the transformation of this matrix yielded the values of E_1 and E_2 . Applying this transformation, the values of the Young's moduli were

$$E_1 = E_2 = 1764 \text{ MPa},$$

and

$$E_3 = 1197 \text{ MPa}$$

(29)

The experimentally obtained value of the Young's modulus E_1 or E_2 was 1636 MPa. It is seen that this value is in good agreement with the value in Eq. (29) with an error of approximately 7.8%.

The values of the components of the compliance or stiffness matrices or the values of the mechanical constants were plugged into ABAQUS to run finite element simulations of parts subjected to loading. These simulations were used compare the experimental results with the numerical results and demonstrate some applications of the results of this research.

CHAPTER IV

APPLICATIONS OF THE CONSTITUTIVE MODEL

To verify the accuracy of our experimental results and to demonstrate the application of the developed constitutive model, experiments and finite element simulations were conducted on simple geometries. ABAQUS was used to carry out the finite element simulations.

IV.1. Three-point bending tests

The rapid prototyped material was tested in three-point bending and the results from the experiments were compared with the results obtained from ABAQUS simulations of parts with the same loading conditions. The results were also compared with the analytical results.

Experimental results

The three-point bending test was carried out along the guidelines provided in the ASTM standard [21]. The specimens were fabricated in four different configurations. The specimen dimensions are as shown in Fig. 29. The specimens were fabricated with their longitudinal axis at 45° to the x-axis of the machine on the xy plane ($3P2$), longitudinal axis along the x-axis of the machine on the xy plane ($3P1$), longitudinal axis along the y-axis of the machine on the yz plane ($3P3$) and longitudinal axis along the z-axis of the machine on the xz plane ($3P4$) of the machine as shown in Fig. 30.

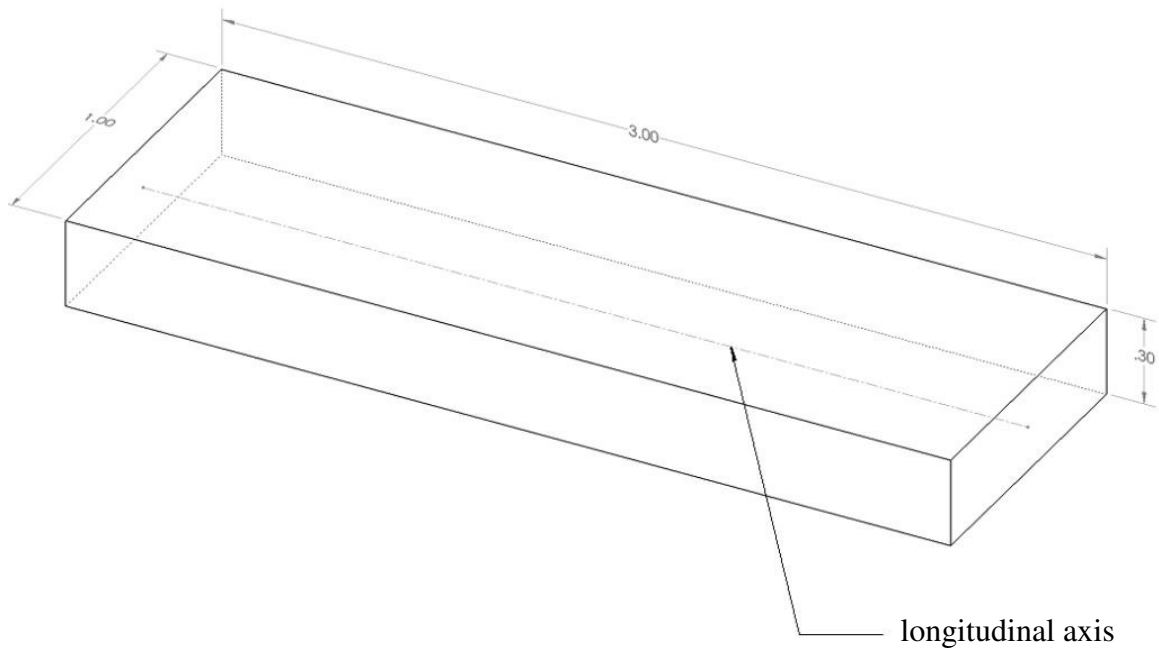


Fig. 29. Dimensions of the three-point bending test specimens

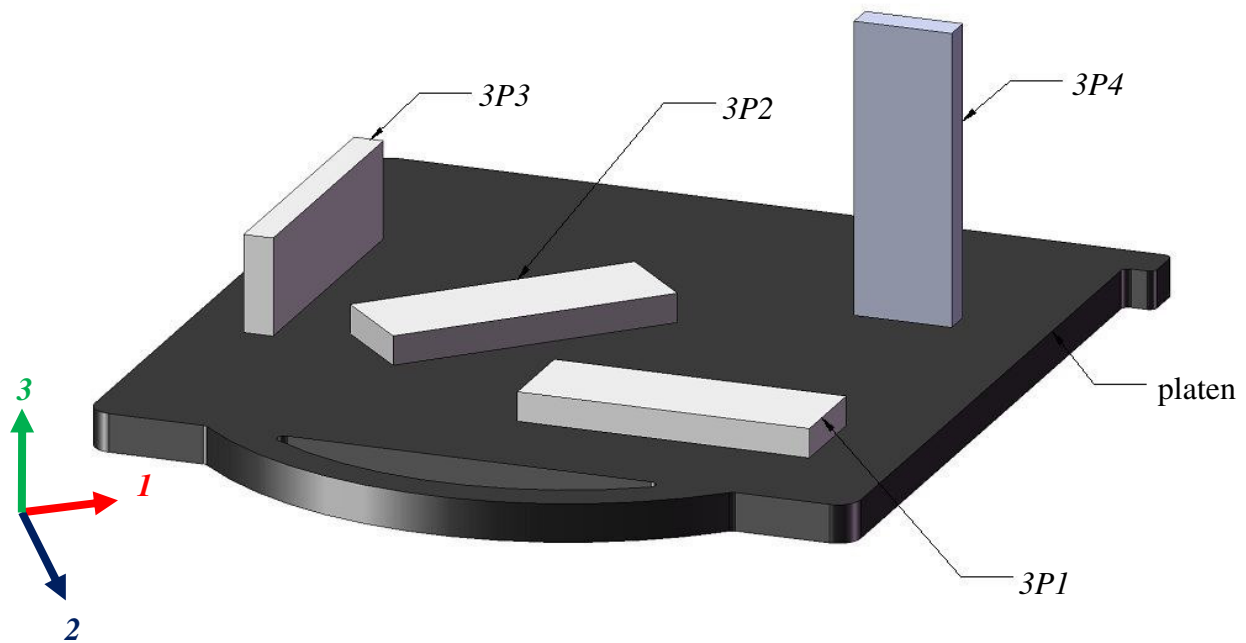


Fig. 30. A schematic of all the three-point bending test specimen configurations

The three-point bending tests were conducted on an Instron 4411 load frame. The machine had its own DAQ connected to LabVIEW and was preset to give us the load and the corresponding deflection data. It had a built-in 1000 lb load cell in it. The three-point bending fixture which consisted of the loading nose and the supports was mounted on the load frame. The support span was set at 50.80 mm (2.00 inches). The loading nose radius was 6.35 mm (0.25 inches) and the support radius was 6.35 mm (0.25 inches). A schematic of the test is shown in Fig. 31. The actual testing rig is shown in Fig. 32. Close up of a specimen undergoing the three-point bending is shown in Fig. 33. A load vs. deflection curve was plotted for all the specimens.

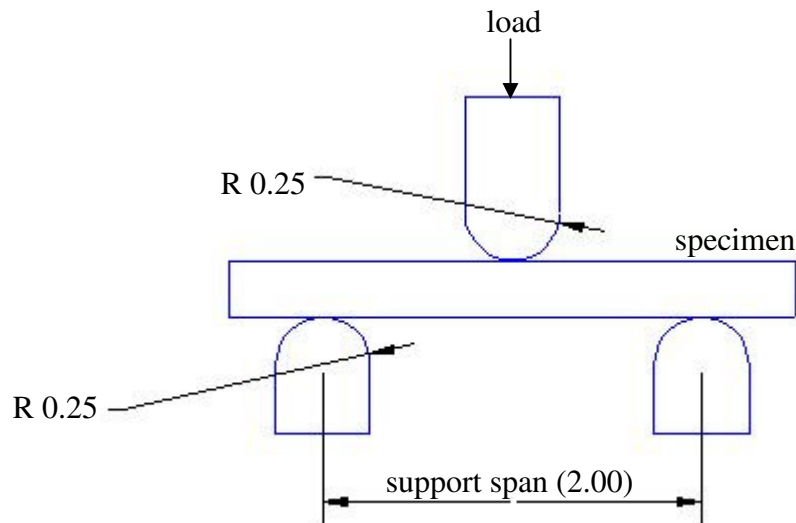


Fig. 31. A schematic of the three-point bending test (all dimensions are in inches)

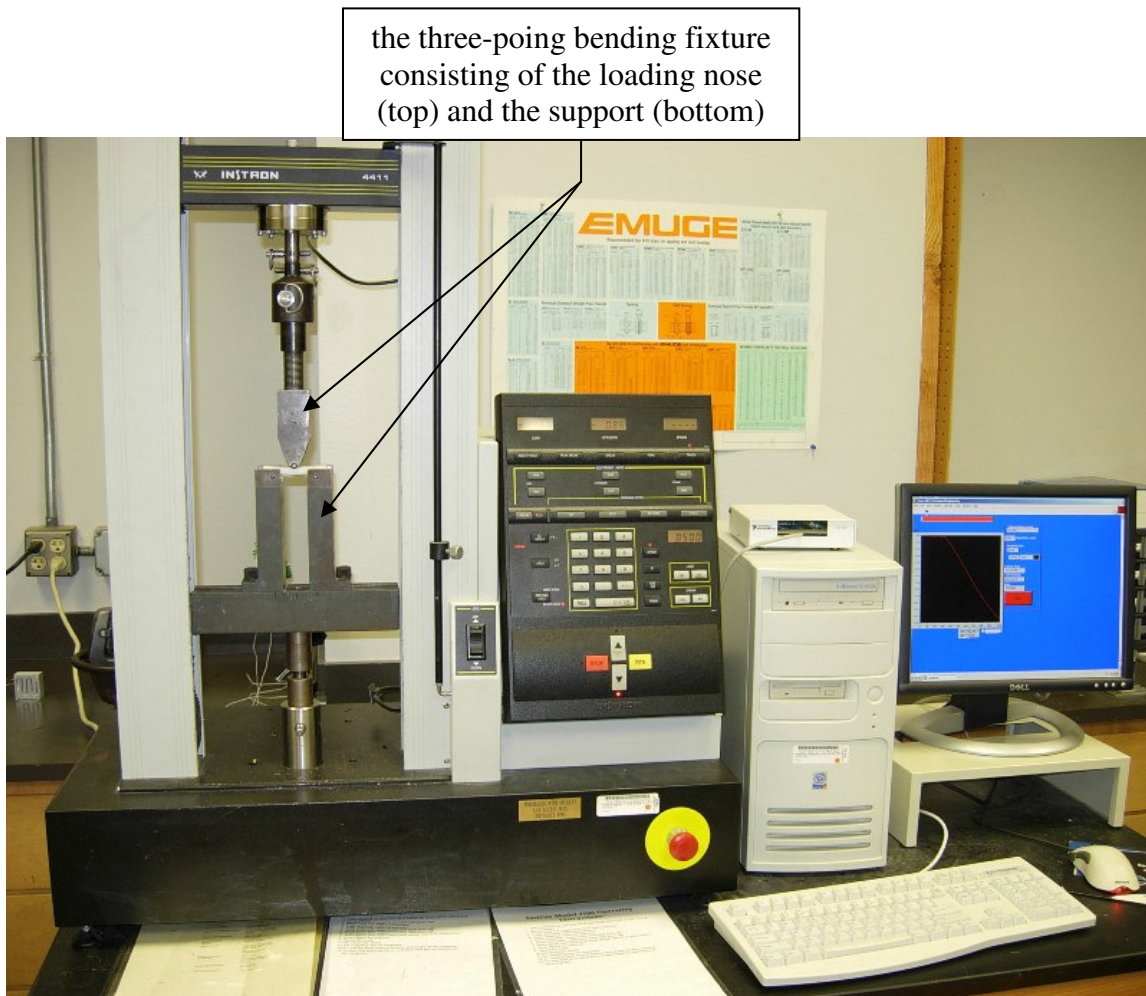


Fig. 32. The Instron 4411 load frame on which the three-point bending tests were conducted



Fig. 33. Close up of a specimen undergoing three-point bending

An observation of the load vs. deflection curves revealed the existence of a large amount of slack in the three-point bending fixture. To take care of this error in the data, toe compensation was provided to the curves. Toe compensation was provided in accordance with the guidelines provided in the ASTM standard [19]. Examination of the load vs. deflection curve also provided with the load at which the material began to yield. This would prove useful while running the ABAQUS simulations. To provide toe compensation to the curves, a deflection vs. load curve was plotted for the linear portion of the load vs. (slack) deflection curve previously plotted (150 N – 400 N in this case). A straight line trend curve was drawn for the deflection vs. load curve to obtain its equation in the form of $y = m.x + c$. The y -intercept of this curve (c) was subtracted from the slack deflections to obtain the actual deflection of the part. This procedure was repeated for all the specimens that were tested to obtain the actual deflections of all specimens. The deflection of all the parts at 200 N was picked as the point of comparison, i.e., the load value that would be used for running ABAQUS simulations and for the analytical calculations. 200 N was chosen because for all the graphs, it was the load value that was approximately in the middle of the linear elastic curve. A characteristic load vs. (slack) deflection curve is shown in Fig. 34, a characteristic deflection vs. load curve used to provide toe compensation is shown in Fig. 35, a characteristic toe compensated load vs. deflection curve is shown in Fig. 36 and deflections of all the specimen configurations, the average deflection and the standard deviation at 200 N are provided in Table 5 and Fig. 37. The ABAQUS simulations that were conducted are explained in the following section.

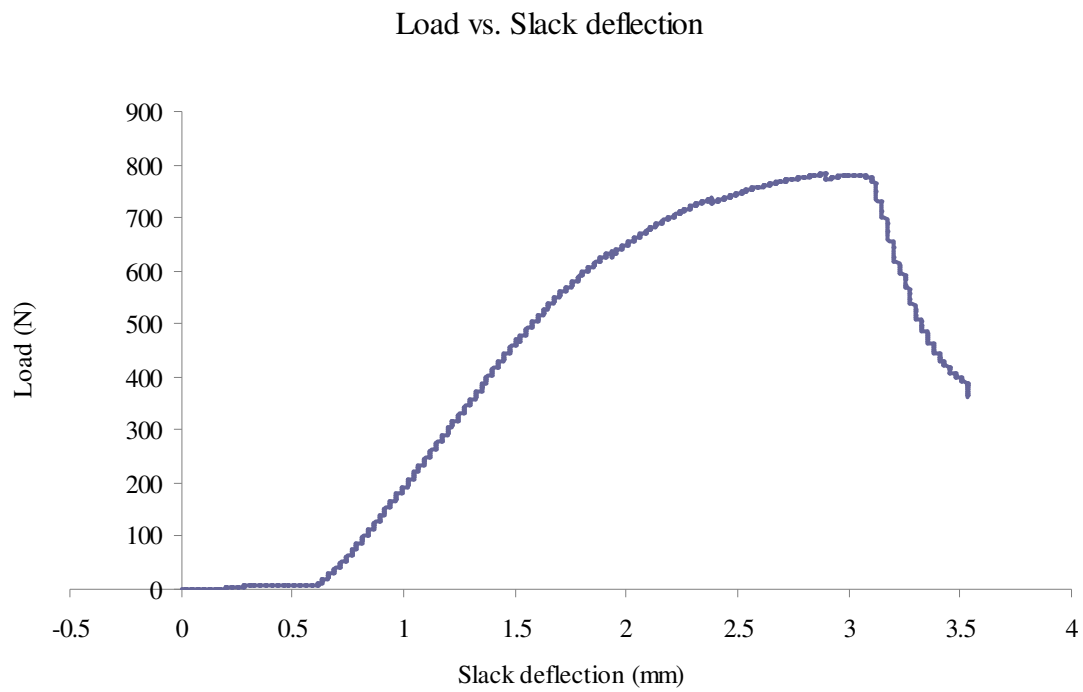


Fig. 34. A characteristic load vs. slack deflection curve

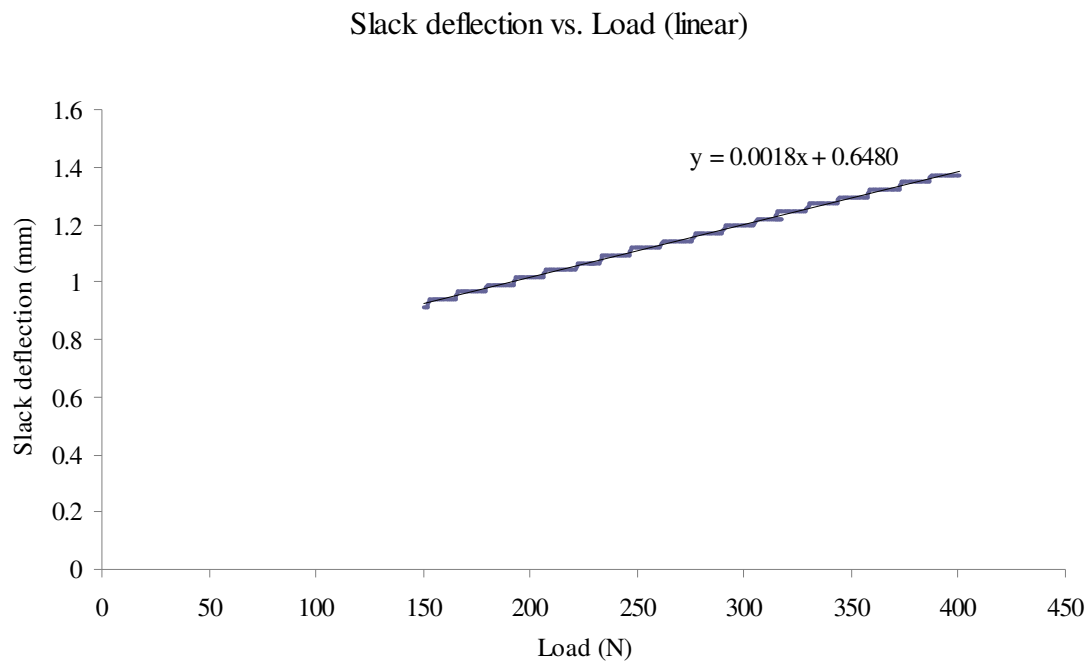


Fig. 35. A characteristic slack deflection vs. load curve that was used to calculate the y-intercept for toe compensation

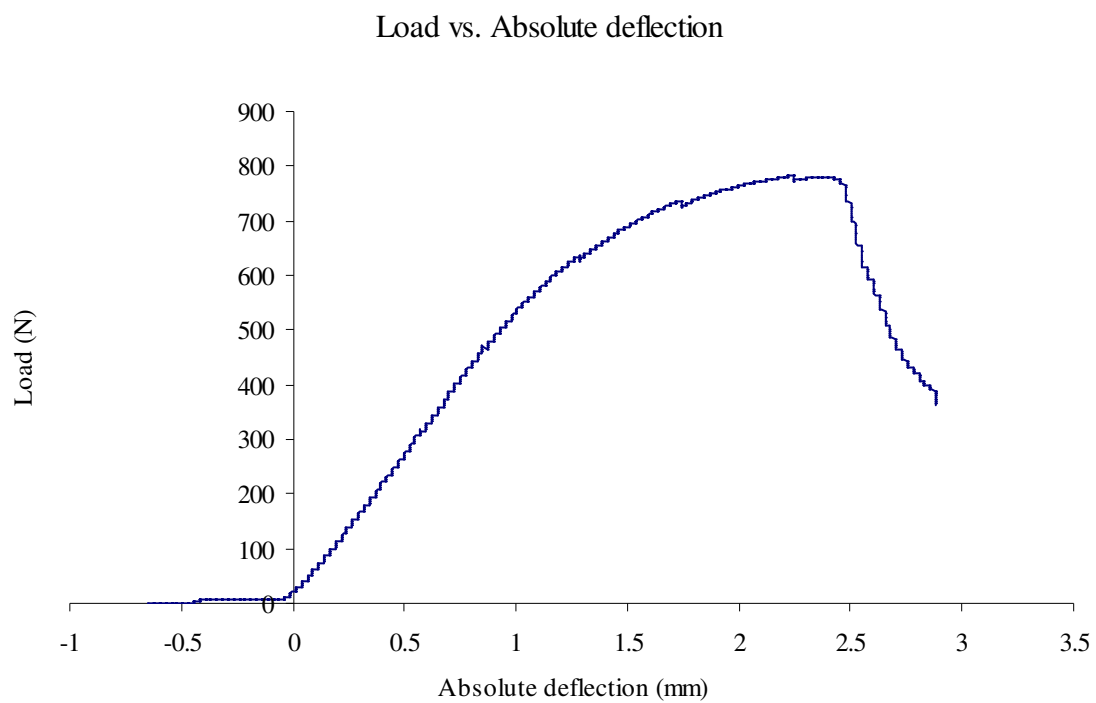


Fig. 36. A characteristic toe compensated load vs. absolute deflection curve

Table. 5. Deflection of all the specimens at 200 N, the average deflection of a specimen configuration and the corresponding standard deviation

<i>Specimen configuration</i>	<i>3P1</i>	<i>3P2</i>	<i>3P3</i>	<i>3P4</i>
Deflection at 200 N (mm)	0.5002	0.4049	0.3676	0.5362
	0.5126	0.3829	0.3848	0.5172
	0.4886	0.3931	0.3662	0.5288
	0.5123	0.3800	0.3680	0.5309
	0.5021	0.4129	0.3681	0.5377
	0.5210	0.3805	0.3771	0.5287
	0.4664	0.3976	0.3719	0.5238
	0.4696	0.3981	0.3588	0.5241
	0.4743	0.4082	0.3807	0.5157
	0.4710	0.3981	0.3699	0.5055
Average	0.4918	0.3956	0.3713	0.5249
Standard deviation	0.0205	0.0115	0.0076	0.0099

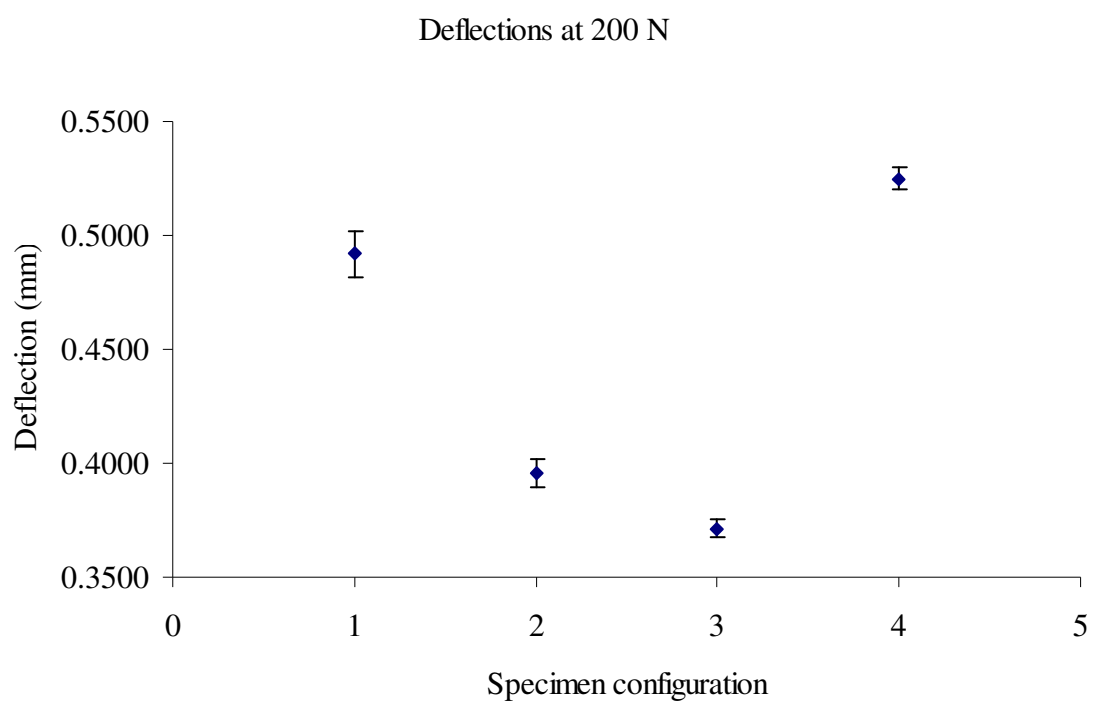


Fig. 37. Deflections at 200 N of all the specimen configurations

Numerical (ABAQUS) results

As discussed earlier, the three-point bending tests conducted above were simulated for a load value using ABAQUS [22]. The SI Units system was used throughout. A solid model of the beam was created using ABAQUS CAE which was then subjected to the loading conditions as shown in Fig. 38.

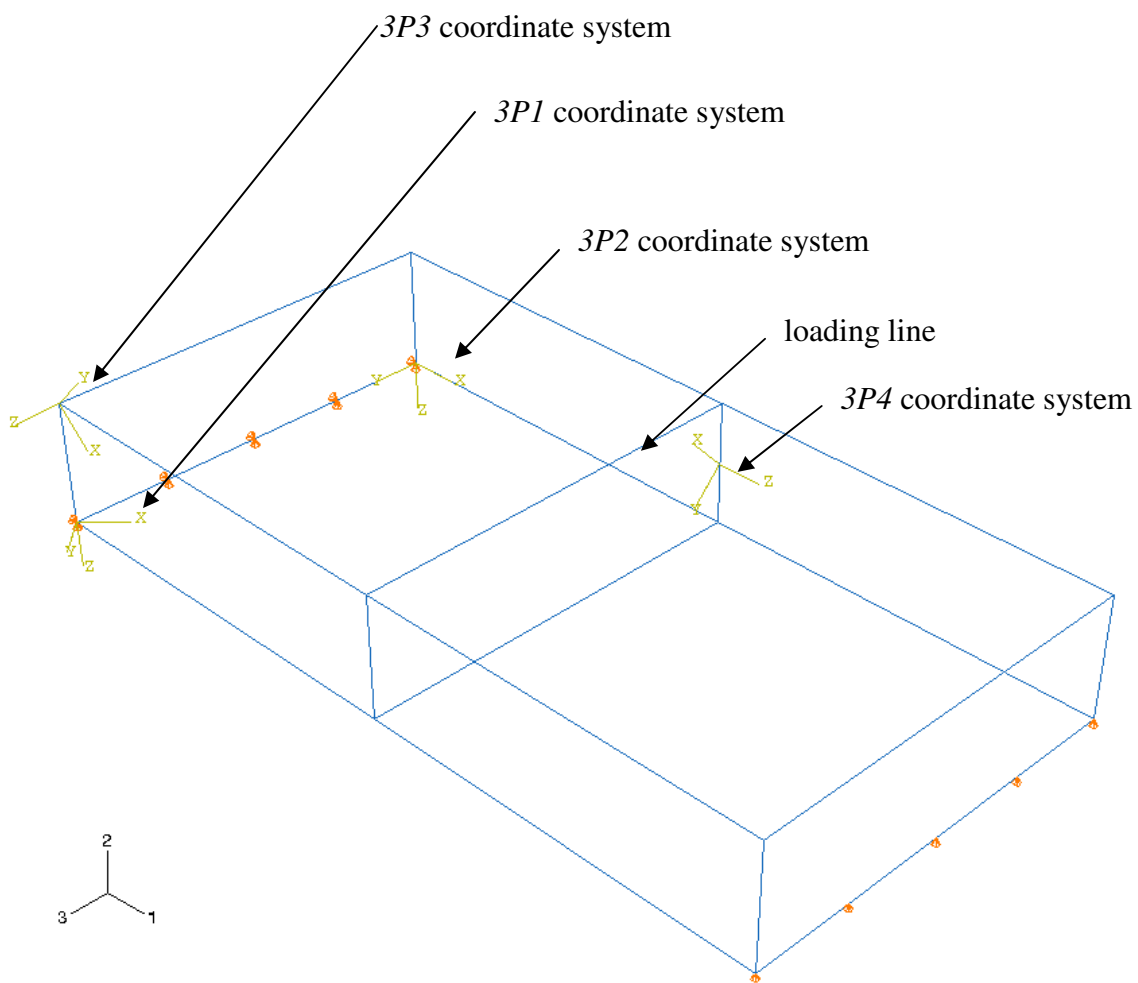


Fig. 38. The loading conditions of the beam in ABAQUS and the coordinate systems used to assign material orientations

The bottom left edge of the beam was restrained from moving in both 1 and 2 directions, and the bottom left edge of the beam was restrained from moving in direction 2. The loading condition was simulated by applying concentrated loads on all the nodes that happened to be on the loading line. The CAE was not used for this and the commands were manually programmed in the input file. The total load of 200 N was divided by the number of nodes to obtain the load value that was applied on each node. The mesh density is shown in Fig. 39. The element shape was chosen as *hex – structured* which is the default element shape in ABAQUS. The element type was *C3D8R: An 8-node linear brick, reduced integration, hourglass control* which is the default element type in ABAQUS because of the fairly simple and symmetric geometry of the beam.

The material properties were entered in the form of material constants which made ABAQUS treat the material as orthotropic. The global coordinate system of the ABAQUS CAE was made to be the machine coordinate system (x, y and z axes). Four different coordinate systems were created to assign the four different material orientations as required by the *3P1*, *3P2*, *3P3* and *3P4* specimen configurations as shown in Fig. 38. An additional rotation of 45° about the z-axis of the specimen configurations was given to make the global coordinate system of ABAQUS coincide with the machine coordinate system. The beam was subjected to the same loading conditions and boundary conditions for each configuration and only the material orientation was changed according to the specimen configuration that was being simulated. Displacement in direction 2 was chosen as the field output to see the deflection of the beam. The deflections of the four specimen configurations are as shown in Figs. 40, 41, 42 and 43.

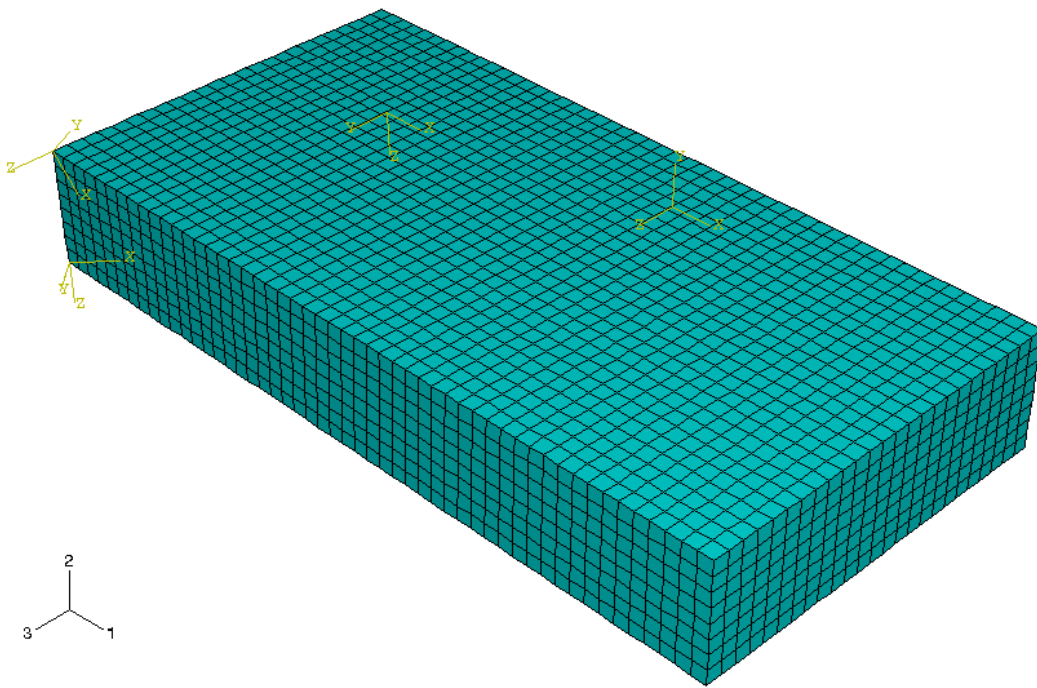


Fig. 39. Mesh density of the beam

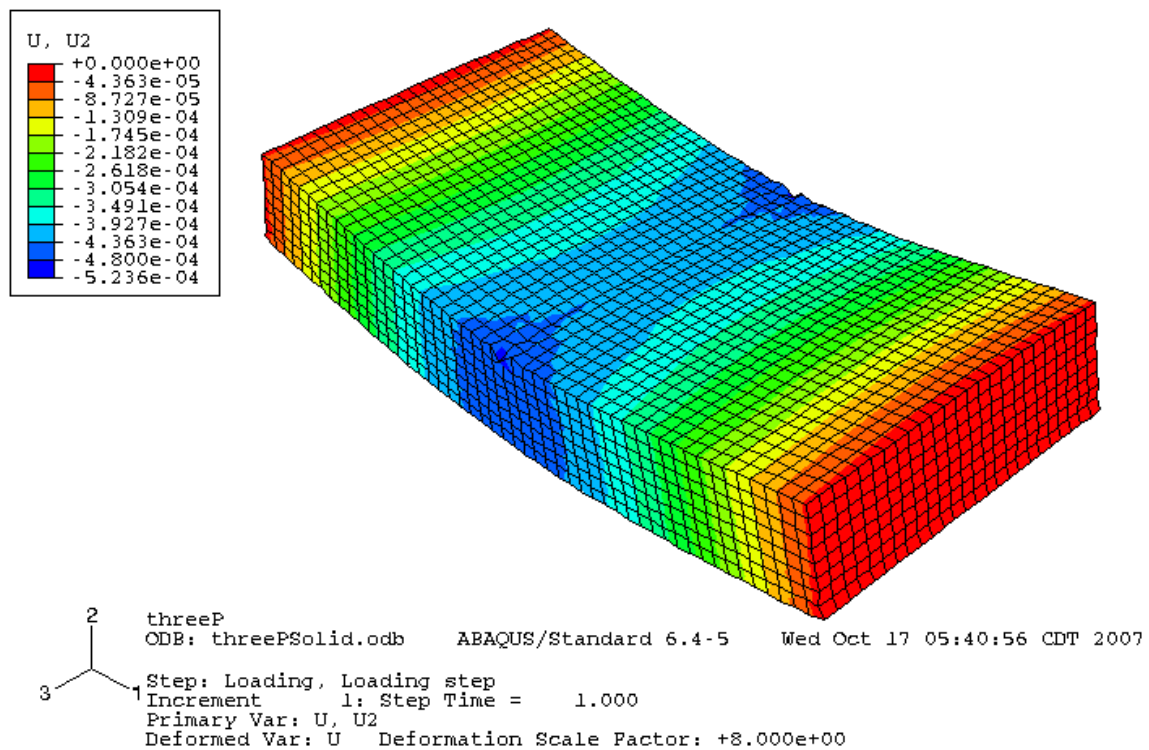


Fig. 40. Deflection of *3PI* specimen configuration (Note – The deflections are in meters (SI Units))

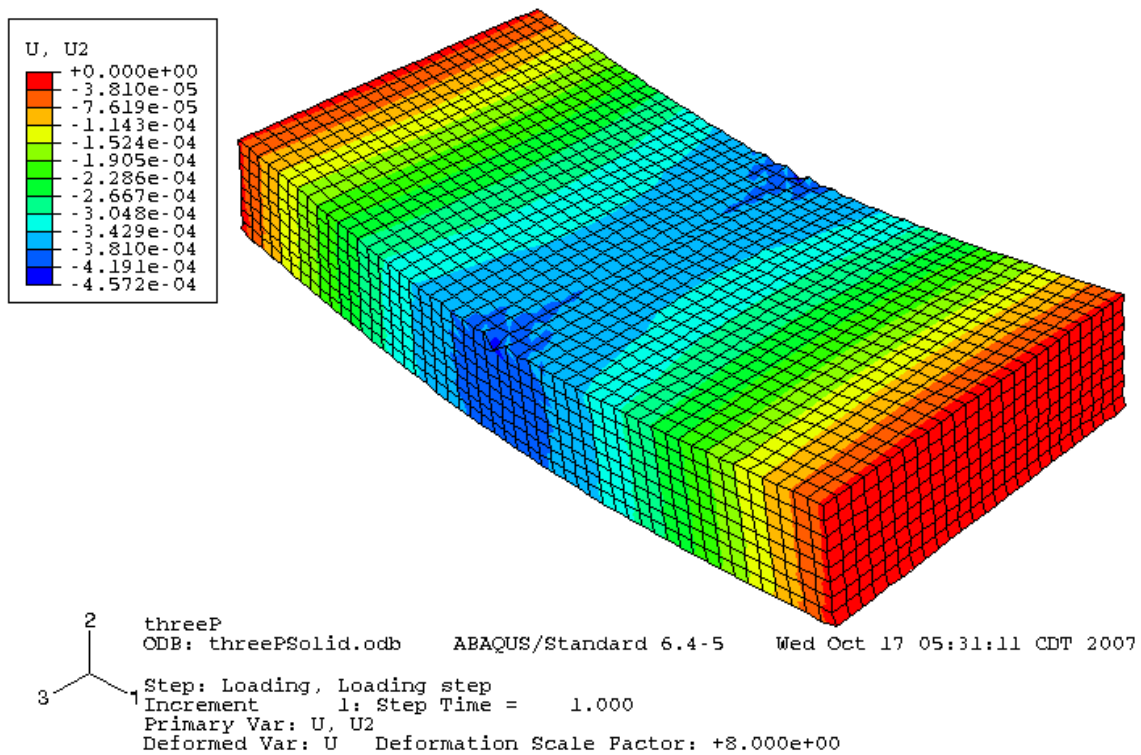


Fig. 41. Deflection of 3P2 specimen configuration (Note – The deflections are in meters (SI Units))

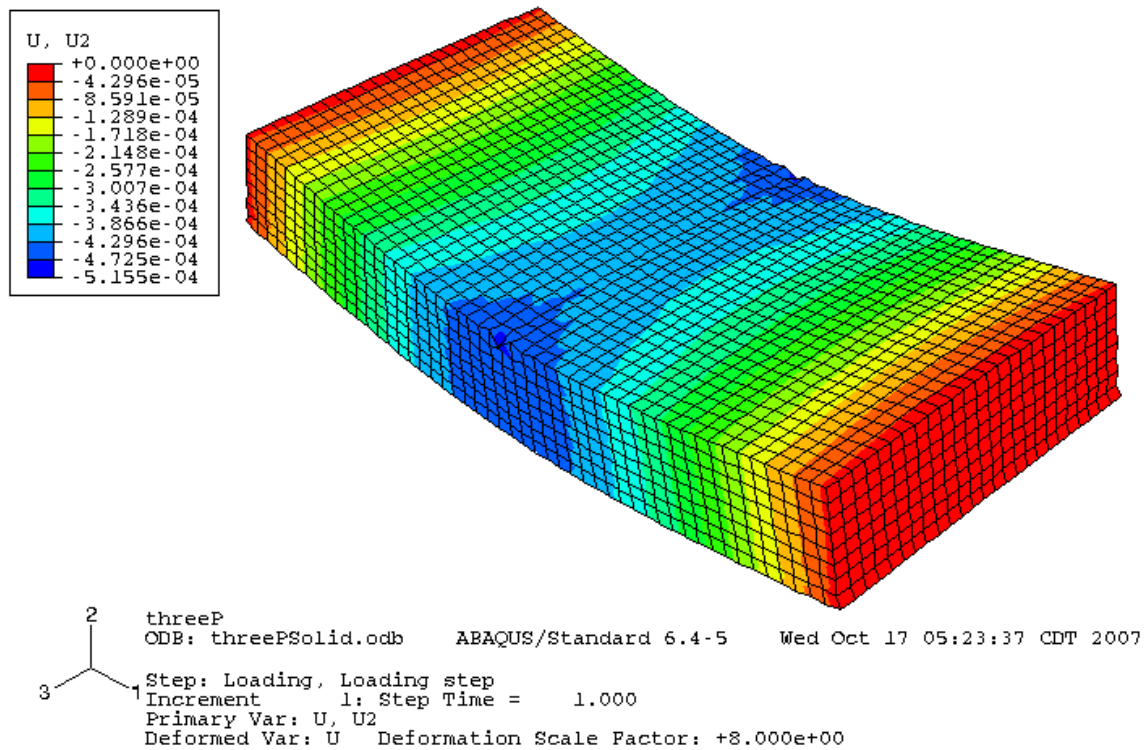


Fig. 42. Deflection of 3P3 specimen configuration (Note – The deflections are in meters (SI Units))

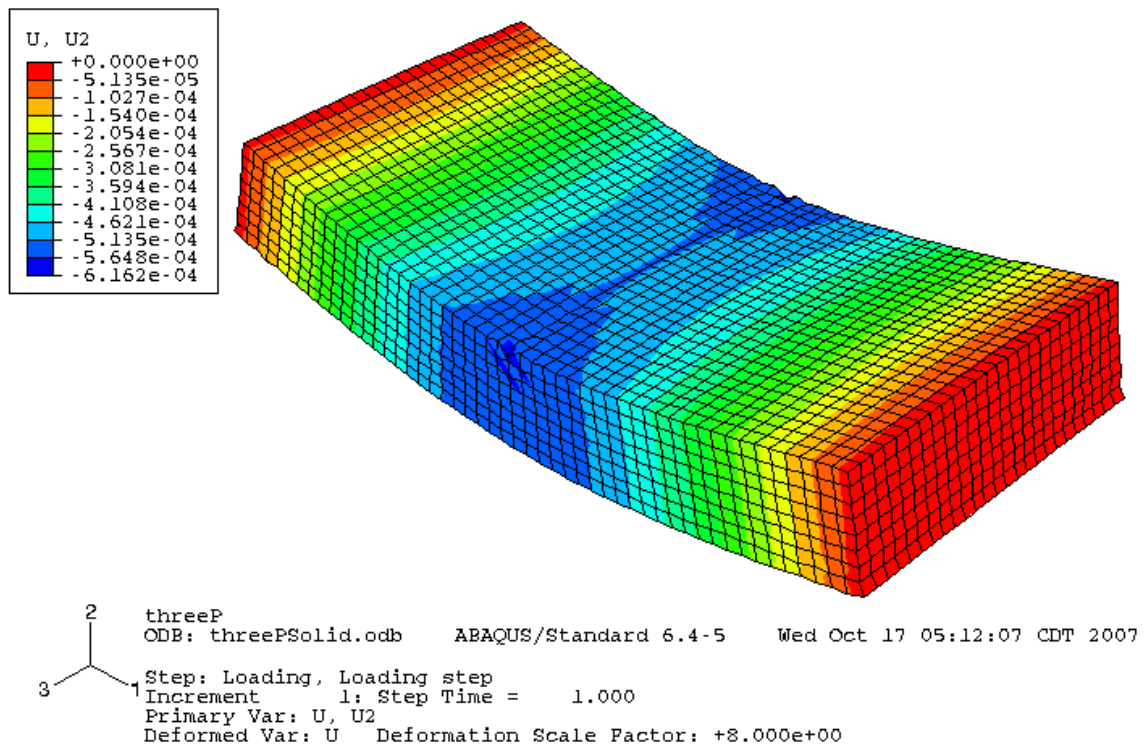


Fig. 43. Deflection of *3P4* specimen configuration (Note – The deflections are in meters (SI Units))

From the ABAQUS simulations as seen from Figs. 40, 41, 42 and 43 the deflections of the beam in various specimen configurations are calculated as the average of the deflection of the middle portion of the beam. Thus, the deflection of the *3P1* specimen configuration was

$$\delta_{3P1} = \frac{0.3927 + 0.4363}{2} = 0.4145 \text{ mm}, \quad (30)$$

the deflection of the *3P2* specimen configuration was

$$\delta_{3P2} = \frac{0.3429 + 0.3810}{2} = 0.3619 \text{ mm}, \quad (31)$$

the deflection of the *3P3* specimen configuration was

$$\delta_{3P3} = \frac{0.3866 + 0.4269}{2} = 0.4081 \text{ mm and} \quad (32)$$

the deflection of the *3P4* specimen configuration was

$$\delta_{3P4} = \frac{0.4621 + 0.5135}{2} = 0.4878 \text{ mm} \quad (33)$$

The deflection of a simply supported beam with a concentrated load in the middle of the beam was calculated analytically using strength of materials approach in the next section.

Analytical results

The deflection of the beam is also calculated using the strength of materials approach in addition to the experimental analysis and ABAQUS simulations. Three-point bending is the same as a simply supported beam with a concentrated load at the center (Fig. 39). Since the beam thickness is comparable to the other width and the length of the beam in this case, deflection due to both bending moment and shear force is considered while calculating the deflection of the beam. The simply supported beam configuration is shown in Fig. 44.

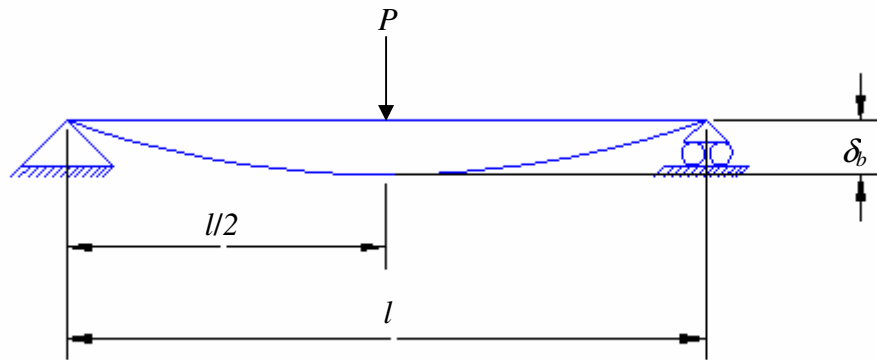


Fig. 44. Simply supported beam configuration

The maximum deflection (at half the beam length) due to bending moment in such a beam is given by [16]

$$\delta_b = \frac{Pl^3}{48EI} \quad (34)$$

where,

δ_b is the maximum deflection in m,

P is the load in N,

l is the length of the beam in m,

E is the Young's modulus of the material along the axis of the beam in Pa, and

I is the polar moment of inertia in m^4 .

For a beam with rectangular cross section, the polar moment of inertia is given by

$$I = \frac{bh^3}{12} \quad (35)$$

where,

b is the width of the beam in m, and

h is the thickness or height of the beam in m.

The maximum deflection due to shearing strain (at half the beam length) in such a beam is given by [16]

$$\delta_s = \frac{3Pl}{8AG} \quad (36)$$

where,

d_s is the maximum deflection due to shearing strain in m, and

A is the area of cross section calculated as the product of the width and the thickness in m^2 ,

G is the shear modulus corresponding to the shearing stress in Pa.

The total deflection of the beam due to both bending and shear is

$$\delta = \delta_b + \delta_s \quad (37)$$

For the *3P1* specimen configuration, the deflection due to bending is calculated by substituting the value of Young's modulus when the material is rotated by 45° about axis 3 of the material as given in Eq. (29) ($E_x = 1480$ MPa) in Eq. (34). The deflection due to shearing strain is calculated by substituting the value of the shear modulus G_{13} in Eq. (36). Thus, the total deflection of the *3P1* specimen configuration is obtained as

$$\delta_{3P1} = 0.3896 + 0.0305 = 0.4201 \text{ mm} \quad (38)$$

Similarly for the *3P2* specimen configuration, the deflection due to the bending is calculated by substituting the value of the E_1 of the material (1636 MPa) in Eq. (34) and the deflection due to shearing strain is calculated by substituting the value of the shear modulus G_{13} of the material in Eq. (36). Thus, the total deflection of the *3P2* specimen configuration is obtained as

$$\delta_{3P2} = 0.3565 + 0.0305 = 0.3870 \text{ mm} \quad (39)$$

For the *3P3* specimen configuration, the deflection due to bending is calculated by substituting the value of E_x of the material (1480 MPa) in Eq. (34) and the deflection due to shearing strain is calculated by substituting the value of the shear modulus G_{12} of the material in Eq. (36). Thus, the total deflection of the *3P3* specimen configuration is obtained as

$$\delta_{3P3} = 0.3896 + 0.0291 = 0.4187 \text{ mm} \quad (40)$$

For the *3P4* specimen configuration, the deflection due to bending is calculated by substituting the value of E_3 of the material (1197 MPa) in Eq. (34) and the deflection due to

shearing strain is calculated by substituting the value of the shear modulus G_{23} of the material in Eq. (36). Thus, the total deflection of the $3P3$ specimen configuration is obtained as

$$\delta_{3P4} = 0.4872 + 0.0305 = 0.5177 \text{ mm} \quad (41)$$

Table 6. A comparison table of the deflections of all specimen configurations at 200 N

	Deflection at 200 N (mm)		
	Experimental results	Numerical (ABAQUS) results	Analytical results
<i>3P1</i>	0.4918	0.4145	0.4201
<i>3P2</i>	0.3956	0.3619	0.3870
<i>3P3</i>	0.3713	0.4081	0.4187
<i>3P4</i>	0.5249	0.4878	0.5177

Comparing the values of the analytical results with the ABAQUS simulation results (Table 6), the error between the displacement values of the $3P1$ specimen configuration is approximately 1.3%, the error between the displacement values of the $3P2$ specimen configuration is approximately 6.4%, the error between the displacement values of the $3P3$ specimen configuration is approximately 2.5% and the error between the displacement values of $3P4$ specimen configuration is approximately 5.7%.

Comparing the values of the analytical results with the experimental results (Table 7), the error between the displacement values of *3P1* specimen configuration is approximately 14.6%, the error between the displacement values of the *3P2* specimen configuration is approximately 2.2%, the error between the displacement values of the *3P3* specimen configuration is approximately 12.7% and the error between the displacement values of the *3P4* specimen configuration is approximately 1.4%.

While the analytical and ABAQUS results matched closely for all the specimen configurations, only the experimental results of the *3P2* and *3P4* configurations matched closely with the analytical and ABAQUS results. The experimental results of the other the *3P1* and *3P3* specimen configuration showed a notable difference with the corresponding analytical and ABAQUS results. This may be explained by the composite like behavior of the material. As given in [21], “since the modulus in three-point bending of highly anisotropic laminates is a critical function of ply-stacking sequence, it will not correlate necessarily with tensile modulus, which is not stacking sequence dependent.”

Considering the bending of *3P1* specimens; it may be noted that when material is in tension, the layer to layer adhesion does not play a key role in the material deformation and it depends on the fiber properties. But, when the material is subjected to three-point bending, since the fibers are at equal orientations to the longitudinal axis of the beam, maximum amount of deflection arises from the layer to layer slippage of the fibers and the fibers carry very little amount of the load. So, if we replace the modulus E_x (1480 MPa) by E_3 (1197) in Eq. (33) while calculating the deflection due to bending, we get

$$\delta_{3P1} = 0.4872 + 0.0305 = 0.5177 \text{ mm} \quad (42)$$

The difference between the experimental and analytical results in this case is approximately 5.3%. It is seen that the accuracy has improved by a large amount.

Considering the bending of *3P2* specimens; when the material is in tension, most of the strength of the material comes from the fibers that are parallel to the axis of loading of the material, i.e., the longitudinal fibers, while the transverse fibers just get pulled away with the longitudinal fibers. When the material is bending, again most of the strength of the material comes from the fibers that are parallel to the longitudinal axis of the beam and the transverse fibers again get pulled away. This explains why the analytical results agreed closely with the experimental results in this case.

Considering the bending of *3P3* specimens; layer to layer adhesion is not of key importance in material deformation when the material is in tension. When the material is in bending also the layer to layer adhesion does not affect the material deformation. When the material experiences shearing deformation, it only results delaminating the material or separating the layers, but since the material is in tension at the same time, the layer separation does not affect the deflection of the beam. So, if we neglect the effect of shearing strain on this configuration while calculating the deflection of the beam, we get

$$\delta_{3P1} = 0.3896 \text{ mm} \quad (43)$$

The difference between the experimental and analytical results in this case is approximately 4.9%. A large degree of improvement is again observed in the accuracy of the predicted results.

Considering the bending of *3P4* specimens; layer to layer adhesion is the source of most of the strength of the material when it is in tension and the material behaves like it would when in tension along the z-axis. The effect of shear is also the same as it would be when the material is in bending. This explains why the analytical results are in close agreement with the experimental results.

IV. 2. Combined bending and torsion tests

The rapid prototyped material was tested in combined bending and torsion and the results from the experiments were compared with the results obtained from ABAQUS simulations of parts with the same loading conditions.

Experimental results

The specimens were tested in simultaneous bending and torsion. The specimens were fabricated in two different specimen configurations. The specimen dimensions were as shown in Fig. 45. The specimens were fabricated in the *xy* plane (*CBT1*) and in the *xz* plane (*CBT2*). The specimen configurations are as shown in Fig. 46. A notch was included in the specimens to place the weight hanger.

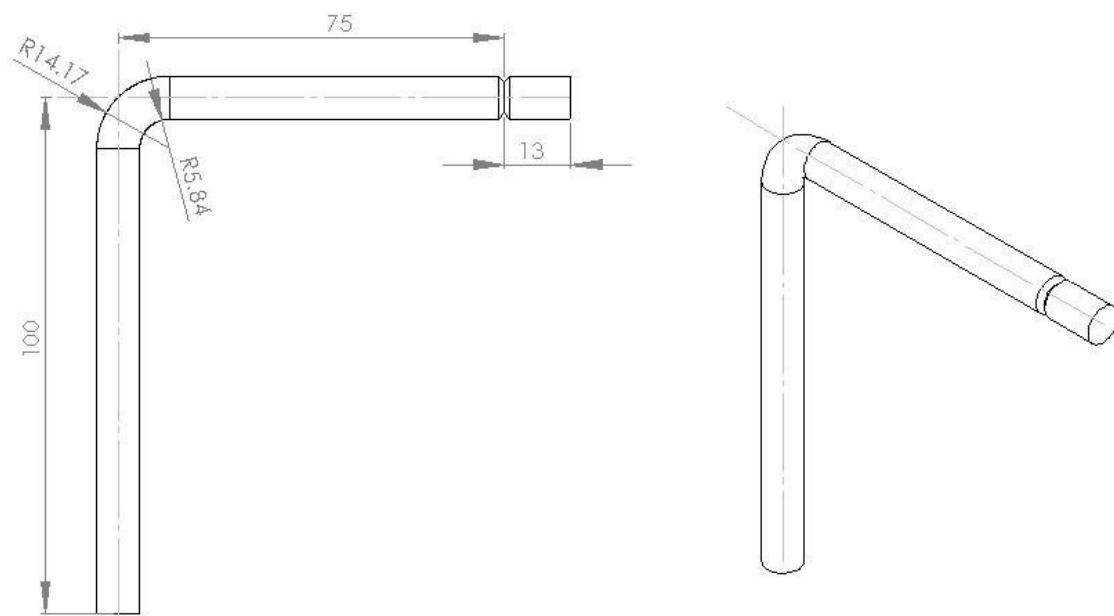


Fig. 45. Specimen dimensions of the specimens on which combined bending and torsion test was conducted (all dimensions are in mm)

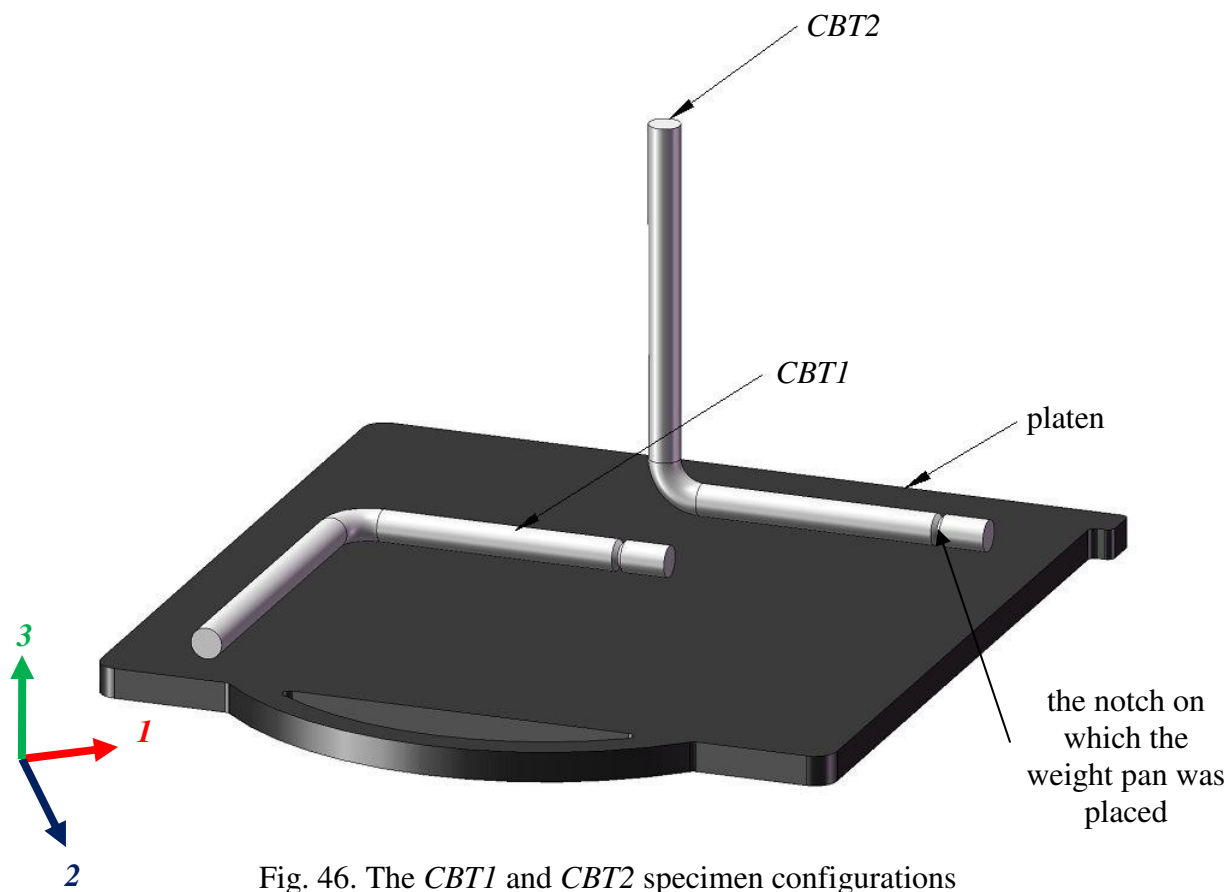


Fig. 46. The *CBT1* and *CBT2* specimen configurations

The combined bending and torsion tests were conducted on a TERCO Twist and Bend testing machine (Fig. 47). The standard configuration was modified a little to suit our purpose. The dial gauge of the instrument was shifted to the other side of the movable clamp and it was placed such that we could place it on the specimen and measure its deflection upon loading it. The pan on which the weight was placed was placed on the notch for which it was created. The other side of the specimen was rigidly clamped on to the movable clamp to restrict all its degrees of freedom. The dial gauge had a least count of 0.01 mm, i.e., the minimum deflection it could measure was 0.01 mm. It had a movable dial which made the deflection measurement easier because the dial gauge could be zeroed before placing the weight. Six specimens from both specimen configurations were tested in combined bending and torsion. The deflection values were tabulated and the average deflection for a specimen configuration and the standard deviation were calculated. Care was taken while placing the weight on the pan to ensure good accuracy of results. A close up of the dial gauge, specimen and the weight pan is shown in Fig. 48. The results of the experiments are as shown in Table 7.

It was seen the *CBT1* specimen configuration had an average deflection of 2.29 mm with a standard deviation of 1.3%, and the *CBT2* specimen configuration had an average deflection of 2.40 mm with a standard deviation of 1.7%.

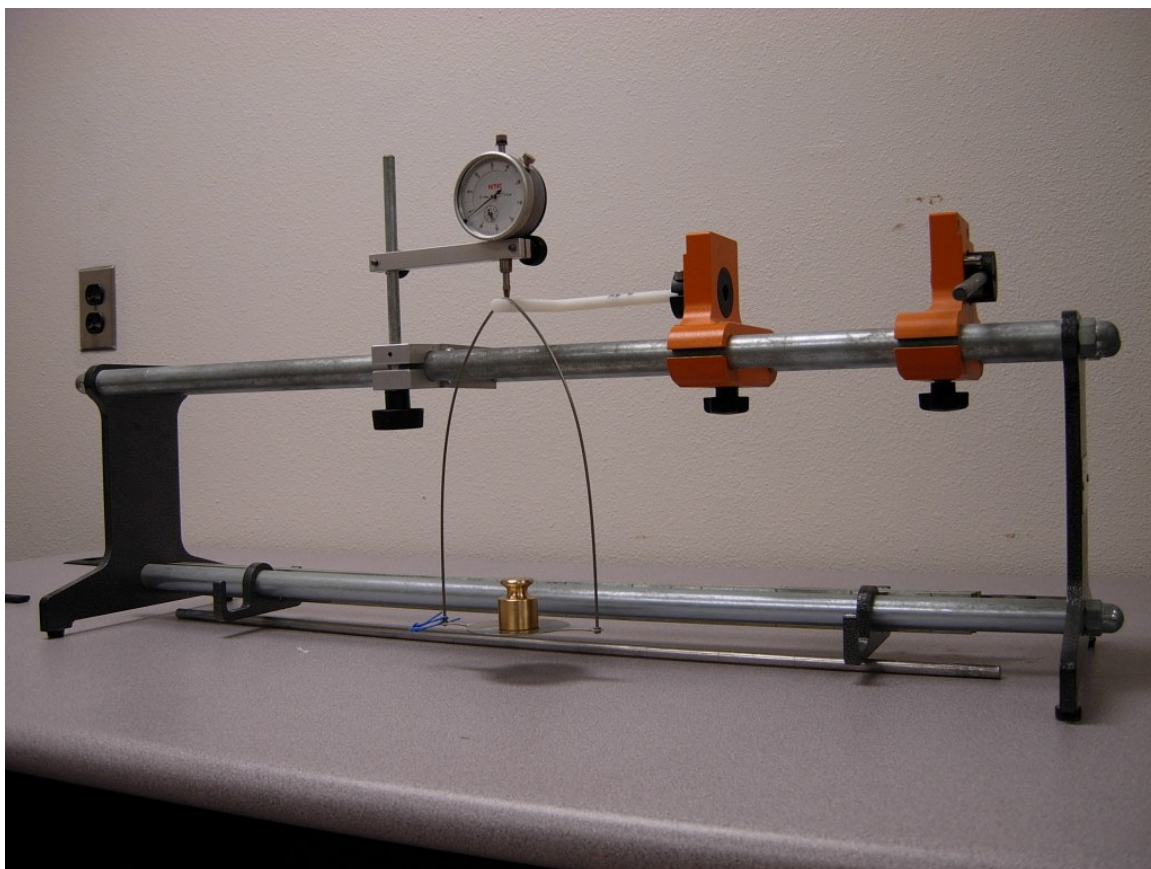


Fig. 47. The TERCO Twist and Bend testing machine used to conduct the combined bending and torsion experiments



Fig. 48. Close up of the dial gauge, specimen and the weight pan

Table 7. Deflection of all the specimens at 100 g, the average deflection of a specimen configuration and the corresponding standard deviation

Specimen configuration	<i>CBT1</i>	<i>CBT2</i>
	2.26	2.35
	2.27	2.45
	2.30	2.41
Deflection at 100 g (mm)	2.26	2.37
	2.33	2.43
	2.33	2.39
Average (mm)	2.29	2.40
Standard deviation	0.03	0.04

Numerical results

As discussed earlier, the combined bending and torsion tests were also simulated in AB-AQUS using the same loading and boundary conditions. The part was created using AB-AQUS CAE by sweeping it along the pre-defined path. The SI Units system was used throughout the analyses. The specimen with the prescribed loading and boundary conditions is shown in Fig. 49.

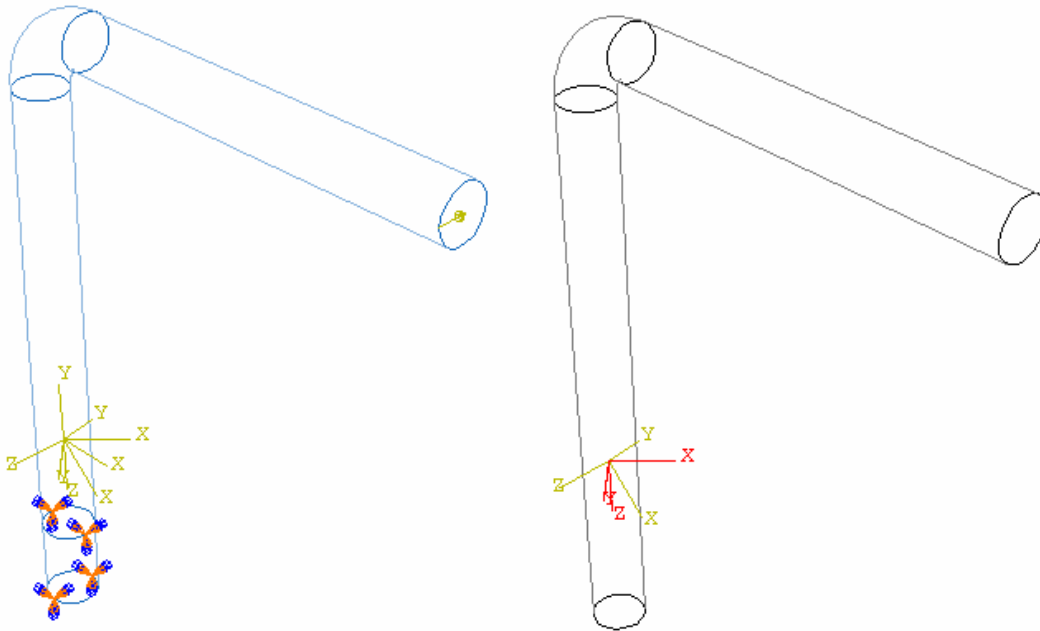


Fig. 49. (Left) The boundary conditions and the loading conditions on the specimen, and (Right) the two different coordinate systems used to simulate the two different specimen configurations (the one in yellow is the *CBT1* coordinate system and the one in red is the *CBT2* coordinate system)

The specimen was partitioned to create a cell from the base to a height of 13.5 mm. This portion of the specimen was restrained from all kinds of motions and rotations. The load was applied along the direction 3 of the ABAQUS coordinate system. The mesh density is shown in Fig. 50. The element shape was chosen as *tet – free* which means that the elements were tetrahedral. The element type was *C3D4: A 4-node linear tetrahedron* which is the default element type for tetrahedral element shape in ABAQUS.

The material properties were entered in the form of material constants which made ABAQUS treat the material as orthotropic, and the machine coordinate system was chosen as the CAE global coordinate system. Two different coordinate systems were created to assign the three different material orientations as required by the *CBT1* and *CBT2* specimen configurations as shown in Fig. 49 and an additional rotation of 45° about the z-axis was applied as before. The beam was subjected to the same loading conditions and boundary conditions for each configuration and only the material orientation was changed according to the specimen configuration that was being simulated. A load of 0.981 N was applied on the specimen. Displacement in direction 3 was chosen as the field output to see the deflection of the specimen. The deflections of the two specimen configurations are as shown in Figs. 51 and 52.

The deflection of *CBT1* specimen configuration is 2.18 mm and the deflection of *CBT2* specimen configuration is 2.34 mm. The difference in experimental and ABAQUS results for the *CBT1* specimen configuration is 4.8% and a difference of 2.5% is seen for the *CBT2* specimen configuration.

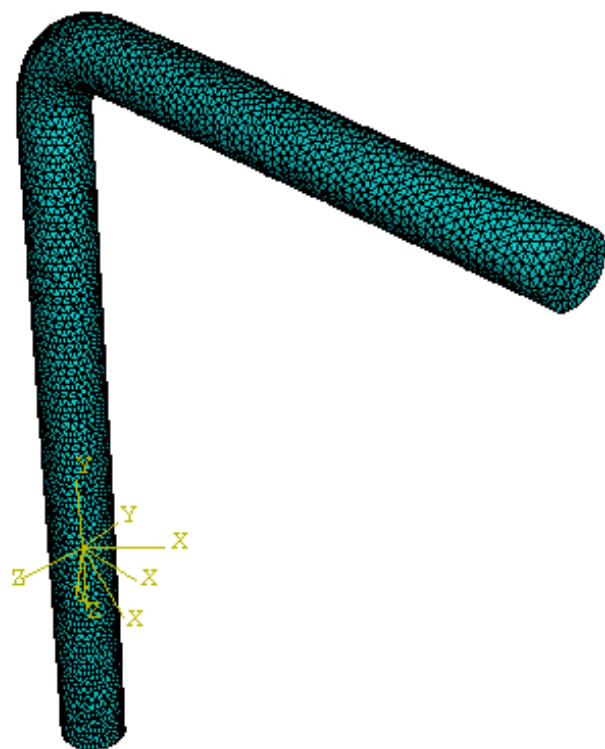


Fig. 50. Mesh density of the combined bending and torsion specimen

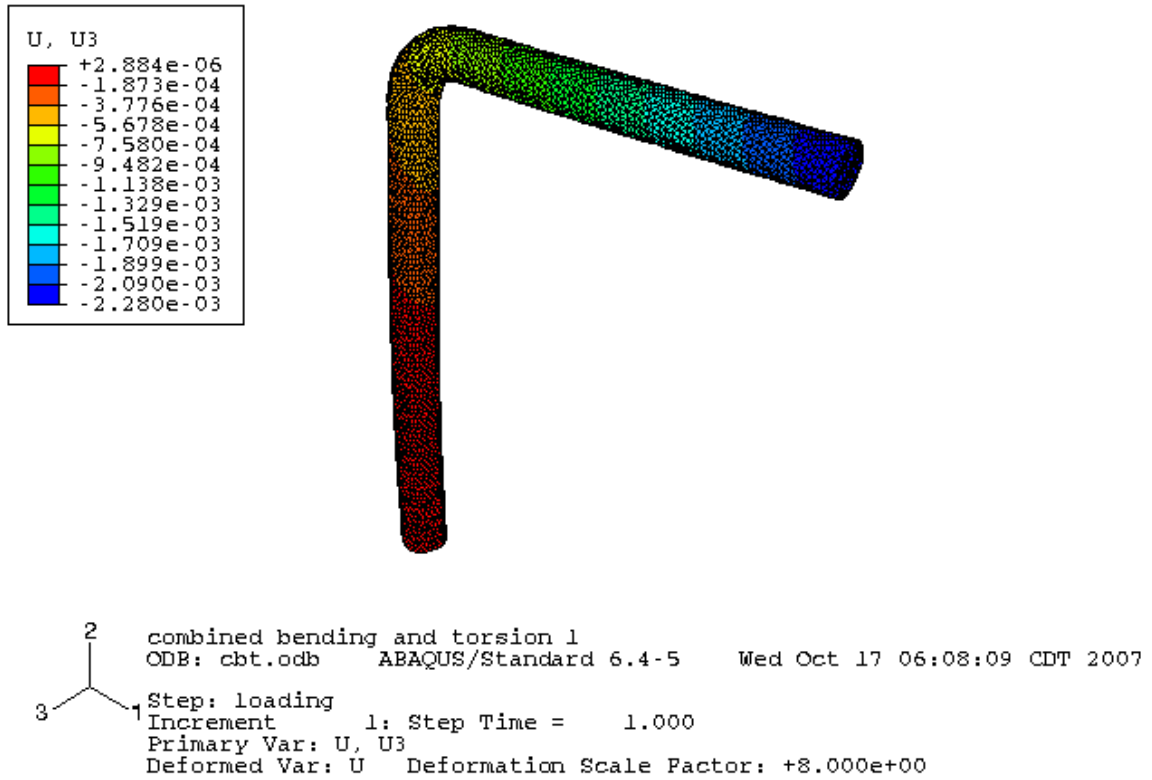


Fig. 51. Deflection of the *CBT1* specimen configuration

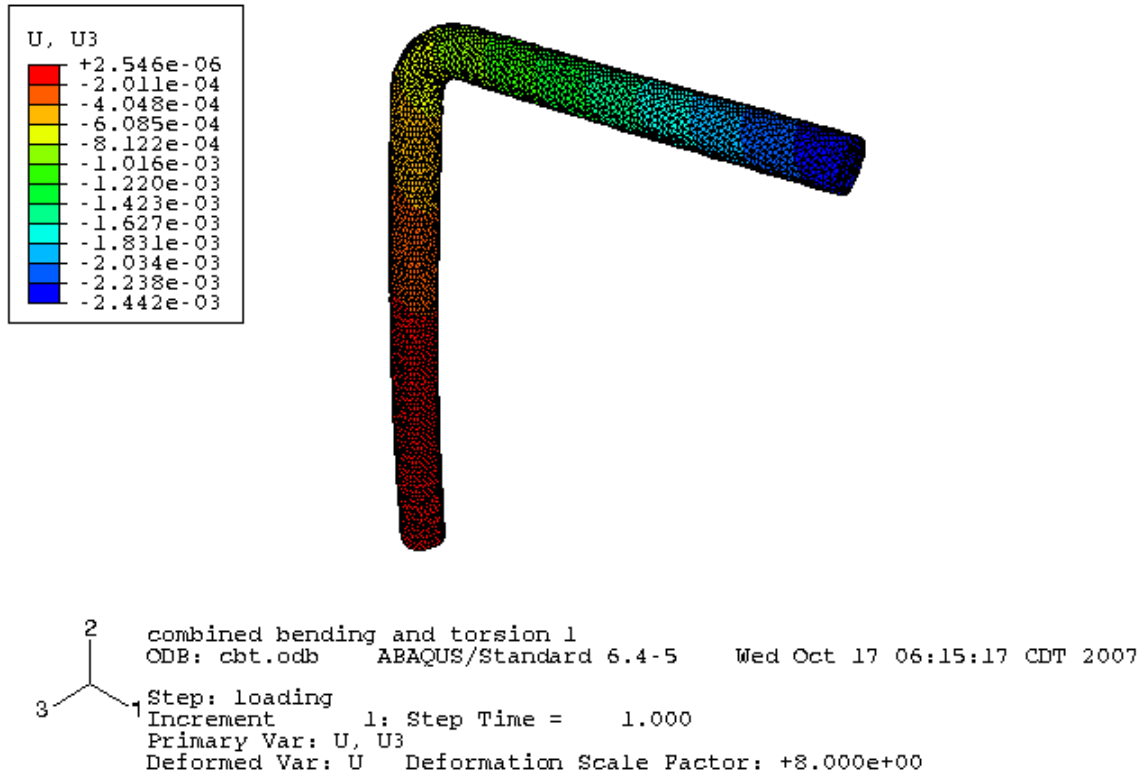


Fig. 52. Deflection of the *CBT2* specimen configuration

IV. 3. Freeform body subjected to pressure loading

To demonstrate the applications of the experimental results, a part that is made of fused deposition material is compared with the same part that is made of the bulk material that is used in fused deposition. A freeform body that was subjected to pressure loading was the part that was analyzed.

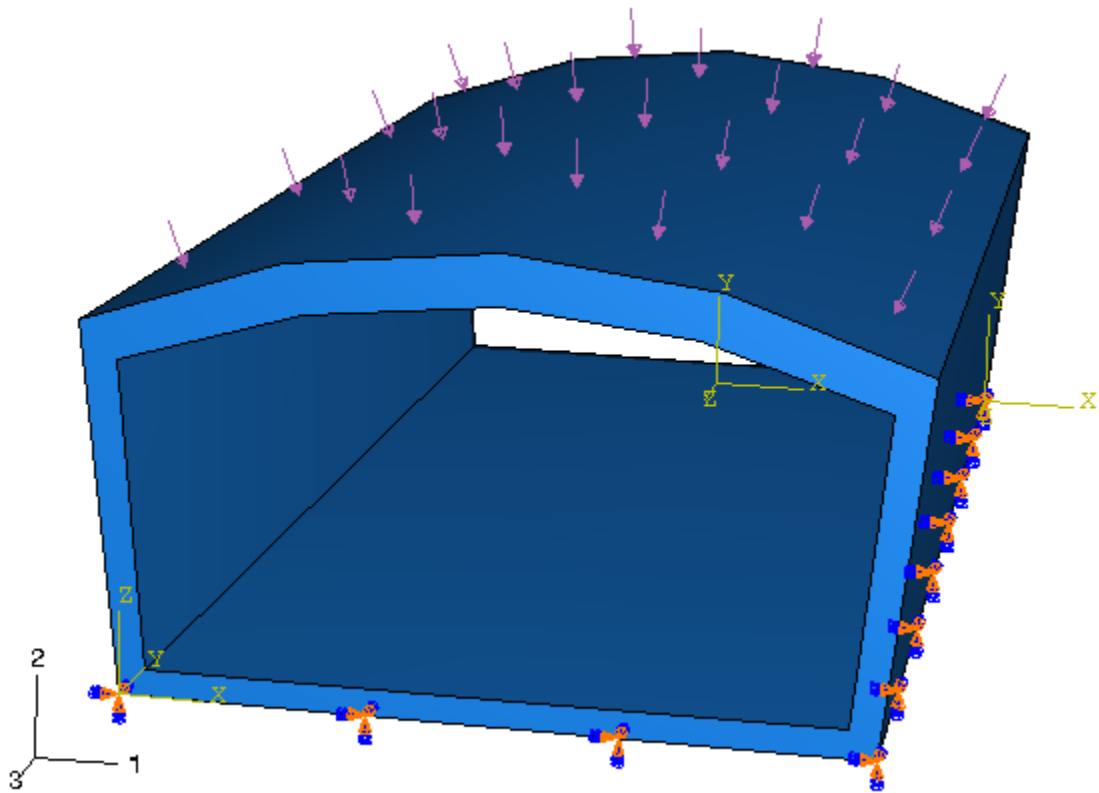


Fig. 53. The hollow freeform body subjected to the boundary and loading conditions

The part was created using ABAQUS CAE by extruding the cross section. The SI Units system was used throughout the analyses. The specimen with the prescribed loading and boundary conditions is shown in Fig. 53. All degrees of freedom were suppressed on the bottom face of the body and a uniform pressure was applied on the upper face. Two materials and solid sections were created to simulate the bulk material and fused deposition material conditions. One of the materials was bulk ABS which is an isotropic material with a Young's modulus of 2230 MPa and a Poisson's ratio of 0.34 [12]. The other material was the fused deposition ABS with material properties as given in Eq. 21.

The mesh density of the part is as shown in Fig. 54. The element shape was chosen as *Hex-Sweep* which was the default element. The element type was *C3D8R: An 8-node linear brick, reduced integration, hourglass control* which is the default element type for *Hex* element shape. The pipe was subjected to a concentrated load of 100 Pa, and a field output of the deflection and the Von Mises stresses in the part was obtained in both cases. The Von Mises stress in the bulk material is as shown in Fig. 55, and the Von Mises stress in the fused deposition material is as shown in Fig. 56. The deflection of the bulk material is as shown in Fig. 57 and the deflection of the fused deposition material is as shown in Fig. 58.

It was seen that the difference in the maximum deflections in the part made of bulk ABS and fused deposition ABS was ~27%.

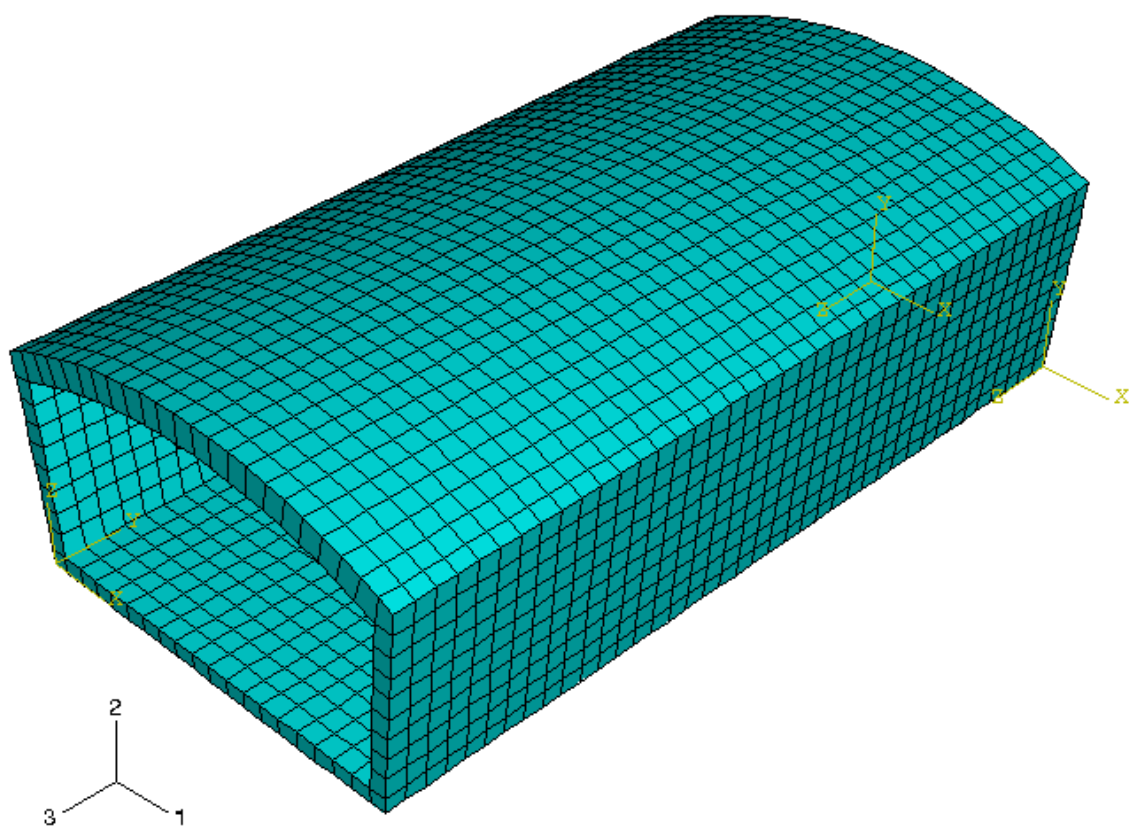


Fig. 54. Mesh density of the freeform body

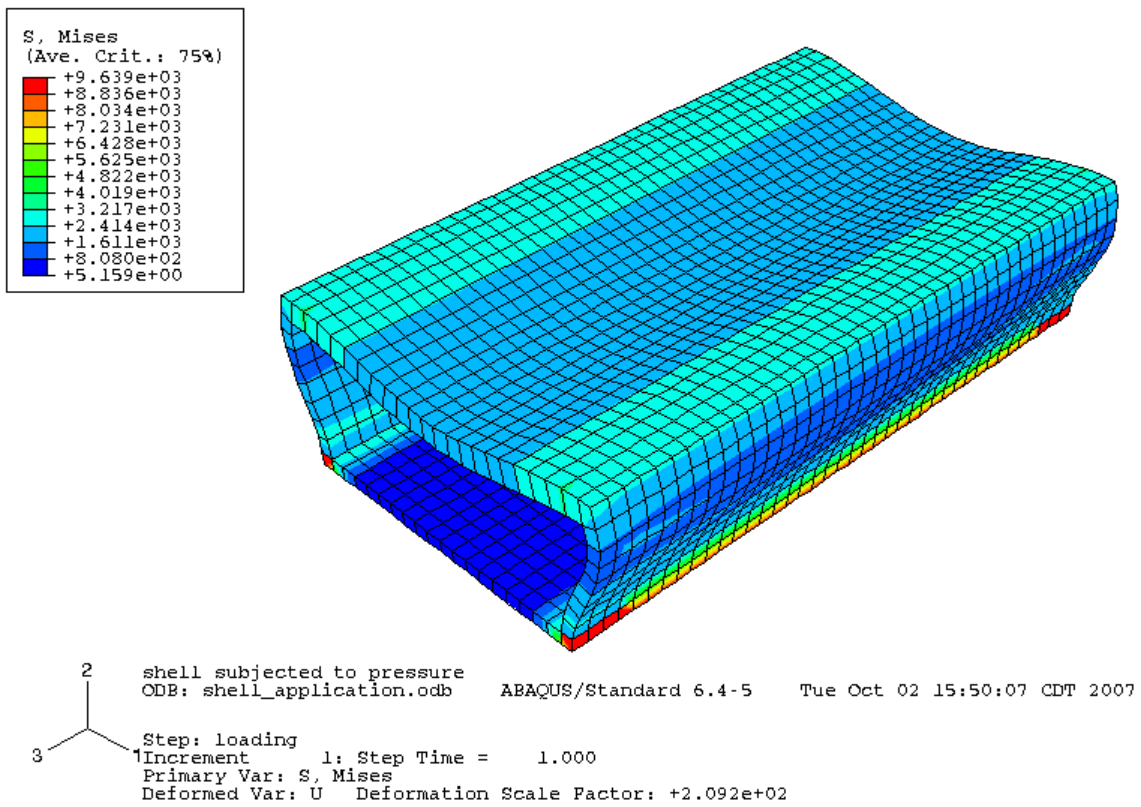


Fig. 55. Von Mises stress in the freeform body made of bulk ABS

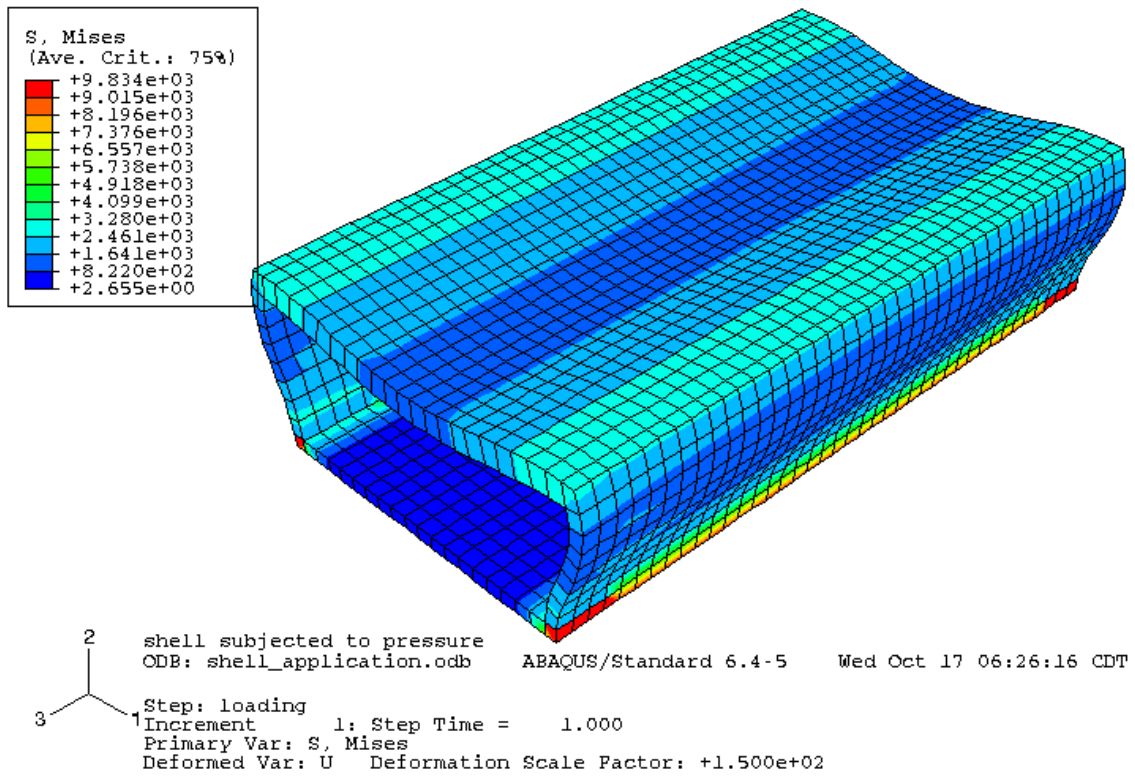


Fig. 56. Von Mises stress in the freeform body made of fused deposition ABS

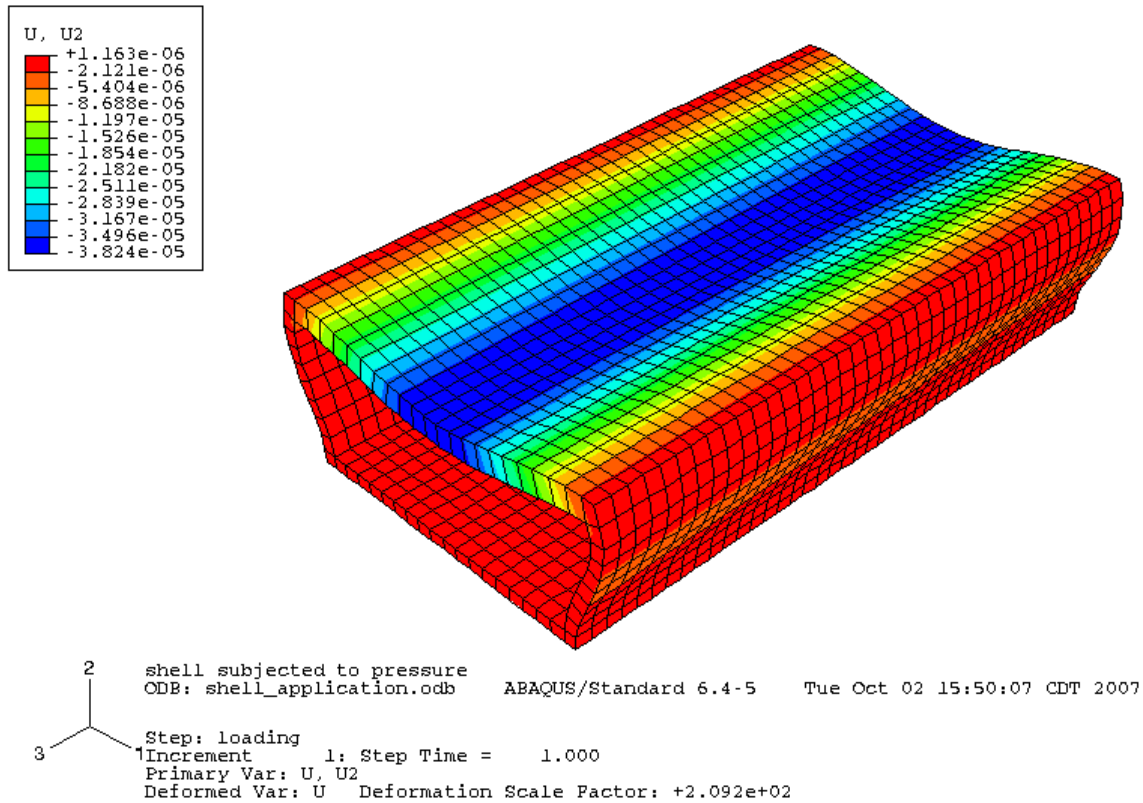


Fig. 57. Deflection of the freeform body made of bulk ABS

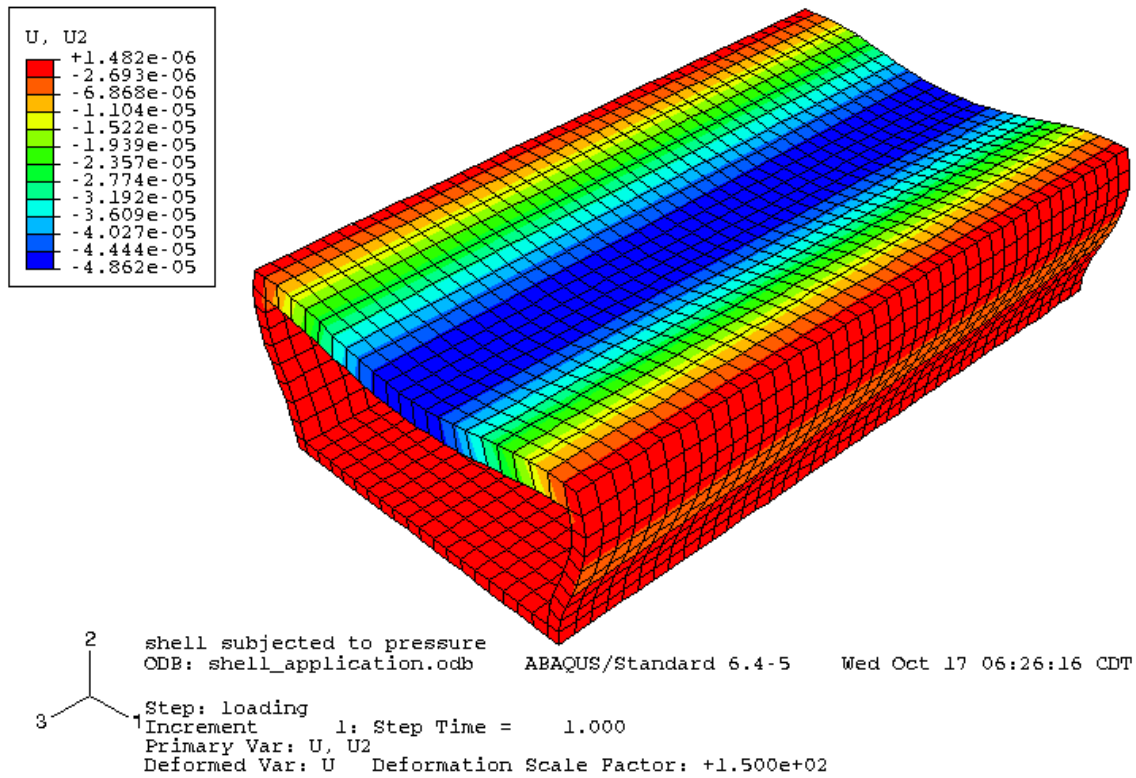


Fig. 58. Deflection in the freeform body made of fused deposition ABS

CHAPTER V

CONCLUSION

A study on the constitutive behavior and material modeling of the rapid prototyped ABS material has been presented. The material structure was analyzed to determine the constitutive law to be applied to define the stress-strain relations. The mechanical material constants that were needed to define the compliance/stiffness matrices completely were identified. Biaxial tensile tests and torsion tests were conducted on different specimens to determine these mechanical material constants.

The main objective was to show that the material can be modeled as a solid material when analyzing the parts that have load carrying applications. This would greatly reduce the computation power and time if the material is simulated using FEA packages.

The mechanical material properties that were experimentally determined were used to simulate various parts to measure the deflections in three-point bending. The deflection was also calculated using analytical methods taking into account both deflections due to bending moment and shearing strain. The deflection was also measured by carrying out three-point bending tests on the corresponding specimen configurations. These tests were carried out on four specimen configurations. It was seen that the results of the finite element simulations and the analytical results agreed closely with each other for all the specimen configurations. The analytical and experimental results were close for two of the specimen configurations (2.2 and 1.4%), but did not agree closely for two other specimen configurations (14.6 and 12.7%). An investigation into this error was carried out and an

explanation as to why there was a difference between those two results was provided. Certain modifications were suggested to improve the predictability of the analytical results. The suggested modifications showed great improvement in the results (5.3 and 4.9% respectively).

The mechanical material properties were also used to simulate parts that were subjected to combined bending and torsion to measure their deflections. The parts were fabricated in two different specimen configurations. The deflections were also measured experimentally. An excellent agreement between the experimental and simulated results was observed (4.8 and 2.5%). Thus, the objective of modeling the material as a solid has been achieved.

The behavior of the material in bending, especially for low depth to span ratios, presents an area for further study. In the fused deposition modeling process, the nozzle is at a higher temperature than the platen on which the part is deposited. So, the fibers begin to solidify soon after coming out of the nozzle. Thus, the material strength also depends on the size of the part being, i.e., the fiber to fiber and layer to layer bonding is weaker in parts that have large dimensions. The effect of dimension of the part or the time taken for the deposition of a layer if included would yield more accurate results. Since the bulk material is primarily a thermoplastic material, an investigation into the viscoelastic properties of the material can also be conducted to improve the accuracy of the model.

REFERENCES

- [1] Kai, C. C., and Fai, L. K., 1997, *Rapid Prototyping: Principles and Applications in Manufacturing*, John Wiley & Sons (Asia) Pte Ltd, Singapore.
- [2] Kalpakijan, S., and Schmid, S. R., 2001, *Manufacturing Engineering and Technology*, Prentice-Hall, Inc., Upper Saddle River, New Jersey.
- [3] Dimension 3D Printing Group: A Business unit of Stratasys, Inc. website, <http://www.dimensionprinting.com/>
- [4] Basdekis, C. H., 1964, *ABS Plastics*, Reinhold Publishing Corporation, New York, Chaps. 1 and 6.
- [5] Masood, S. H., 1996, "Intelligent Rapid Prototyping with Fused Deposition Modeling," *Rapid Prototyping Journal*, **2**(1), pp. 24-33.
- [6] Palmer, J. A., Summers, J. L., Davis, D. W., Gallegos, P. L., Chavez, B. D., Yang, P., Medina, F., and Wicker, R. B., 2005, "Realizing 3-D Interconnected Direct Write Electronics within Smart Stereolithography Structures," IMECE2005-79360, *Proceedings of 2005 ASME International Mechanical Engineering Congress and Exposition*, ASME, Orlando, FL.

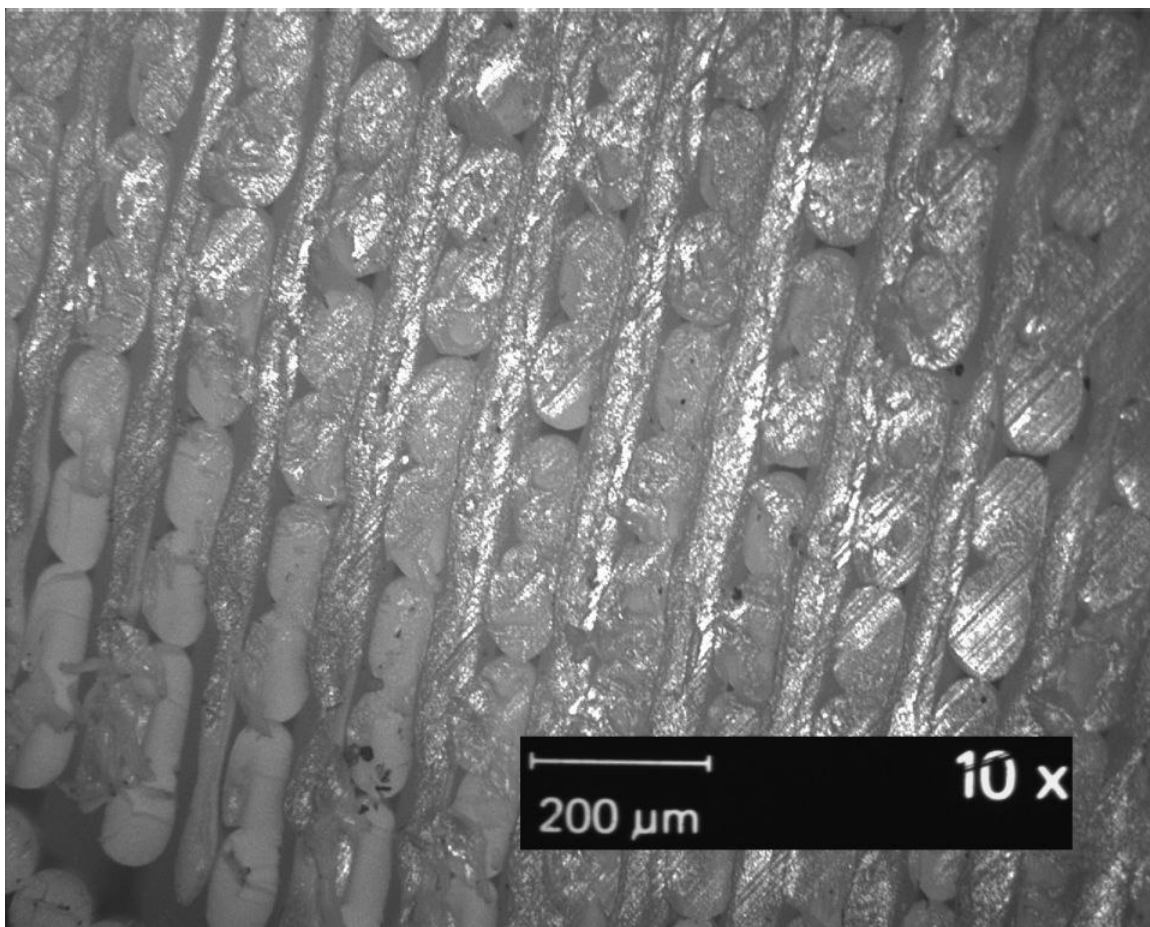
- [7] Agarwala, M. K., Jamalabad, V. R., Langrana, N. A., Safari, A., Whalen, P. J., and Danforth, S. C., 1996, "Structural Quality of Parts Processed by Fused Deposition," *Rapid Prototyping Journal*, **2**(4), pp. 4-19.
- [8] Kulkarni, P., and Dutta, D., 1999, "Deposition Strategies and Resulting Part Stiffnesses in Fused Deposition Modeling," *ASME Journal of Manufacturing Science and Engineering*, **121**, pp. 93-103.
- [9] Rodríguez, J. F., Thomas, J. P., and Renaud, J. E., 2001, "Mechanical Behavior of Acrylonitrile Butadiene Styrene (ABS) Fused Deposition Materials. Experimental Investigation," *Rapid Prototyping Journal*, **7**(3), pp. 148-158.
- [10] Rodríguez, J. F., Thomas, J. P., and Renaud, J. E., 2003, "Mechanical Behavior of Acrylonitrile Butadiene Styrene Fused Deposition Materials Modeling," *Rapid Prototyping Journal*, **9**(4), pp. 219-230.
- [11] Rodríguez, J. F., Thomas, J. P., and Renaud, J. E., 2003, "Design of Fused-Deposition ABS Components for Stiffness and Strength," *ASME Journal of Mechanical Design*, **125**, pp. 545-551.
- [12] Ahn, S-H., Montero, M., Odell, D., Roundy, S., and Wright, P. K., 2002, "Anisotropic Material Properties of Fused Deposition Modeling ABS," *Rapid Prototyping Journal*, **8**(4), pp. 248-257.

- [13] Bellini, A., and Güçeri, S., 2003, "Mechanical Characterization of Parts Fabricated using Fused Deposition Modeling," *Rapid Prototyping Journal*, **9**(4), pp. 252-264.
- [14] Daniel, I. M., and Ishai, O., 1994, *Engineering Mechanics of Composite Materials*, Oxford University Press, Inc., New York, New York.
- [15] Kollár, L. P., Springer, G. S., 2003, *Mechanics of Composite Structures*, Cambridge University Press, New York.
- [16] Timoshenko, S., Young, D. H., 1968, *Elements of Strength of Materials*, D. Van Nostrand Company, Inc., Princeton, New Jersey.
- [17] E 143 – 02, Standard Test Method for Shear Modulus at Room Temperature, ASTM International, United States.
- [18] The *Model 632.85 Biaxial Extensometer* Manual, 1986, MTS Systems Corp., Eden Prairie, Minnesota.
- [19] D 638 – 03, Standard Test Method for Tensile Properties of Plastics, ASTM International, United States.

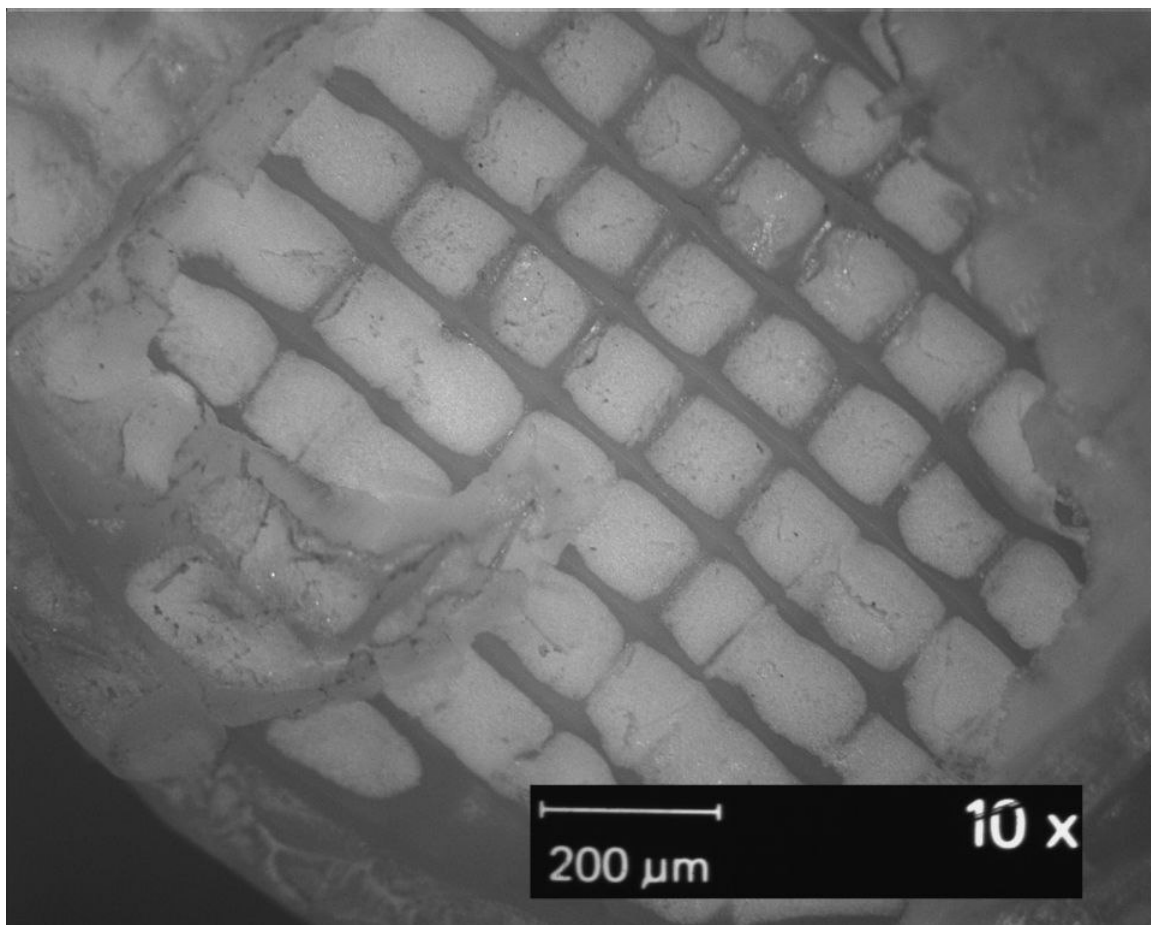
- [20] The LabVIEW™ Basics I Course Manual, © 1993, 2000 National Instruments Corporation, Austin, Texas.
- [21] D 5934 – 02, Standard Test Method for Determination of Modulus of Elasticity for Rigid and Semi-Rigid Plastic Specimens by Controlled Rate of Loading Using Three-Point Bending, ASTM International, United States.
- [22] ABAQUS User's Manual, © ABAQUS, Inc. 2004, Online Documentation, <http://sc.tamu.edu:2080/v6.5/>

APPENDIX A

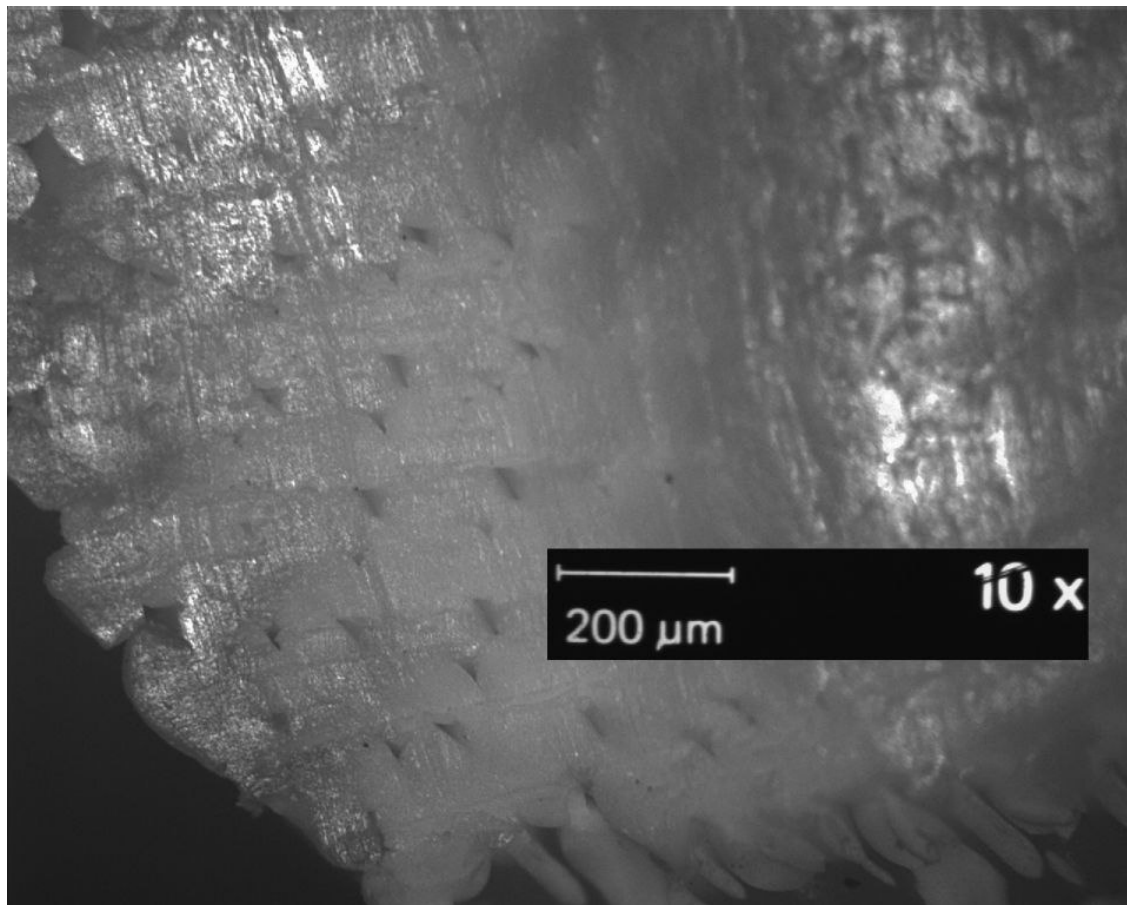
MICROGRAPHS OF VARIOUS CROSS SECTIONS



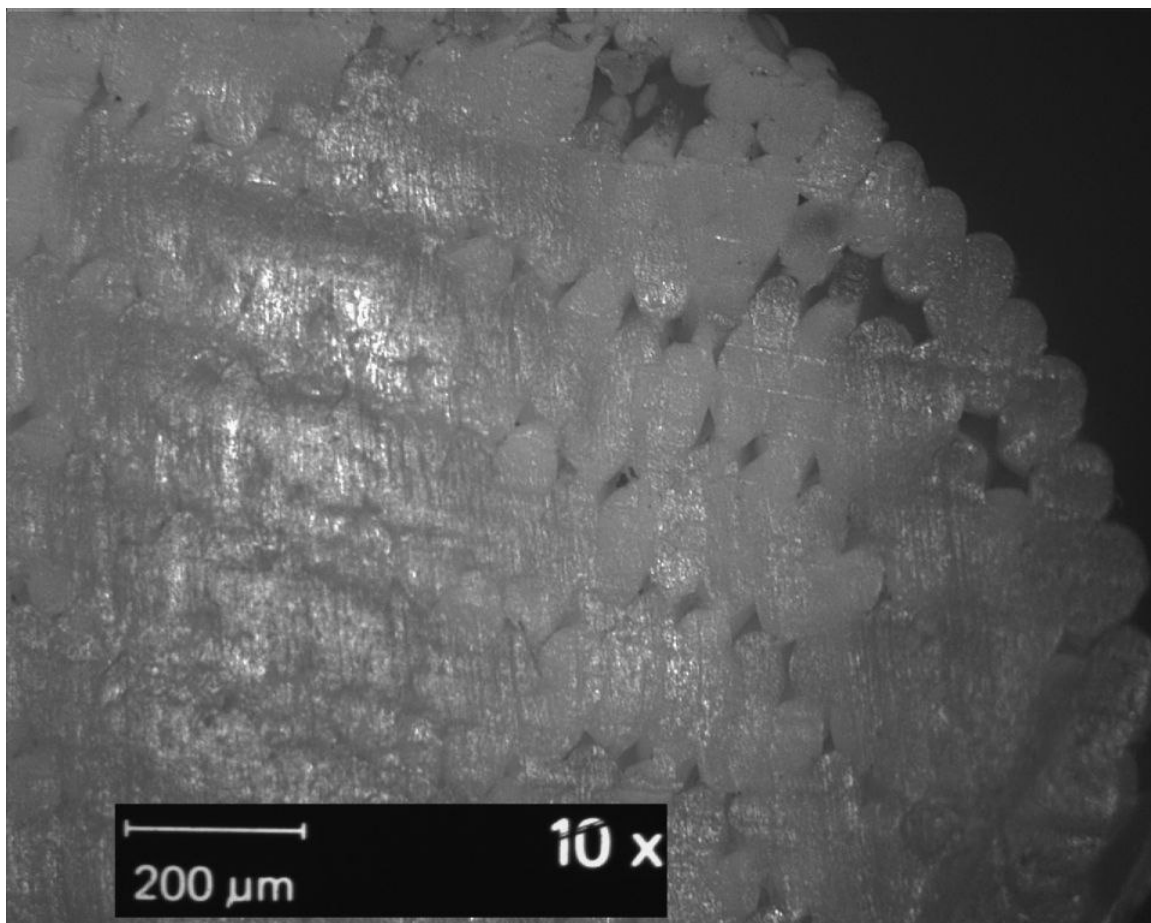
Micrograph of a cross section of a *TR5* specimen



Micrograph of a cross section of a *TR3* specimen



Micrograph of a cross section of a *TRI* specimen



Micrograph of a cross section of a *TR2* specimen

APPENDIX B

TRANSFORMATION OF THE COMPLIANCE MATRIX

Consider two Cartesian coordinate systems with axes p, q, r and p', q', r' . The orientation of the primed coordinate system with respect to the unprimed coordinate system can be specified in terms of three angles θ_p, θ_q and θ_r that are the consecutive rotations of the primed coordinate system about the p, q and r axes. These angles are positive in the counterclockwise direction.

The elements of the compliance matrix in the primed coordinate system and the elements of the compliance matrix in the unprimed coordinate system are related by the expression

$$[S'] = [T_\epsilon] \cdot [S] \cdot [T_\sigma]^{-1}$$

where,

$$[T_\epsilon] = [T_\epsilon^p] \cdot [T_\epsilon^q] \cdot [T_\epsilon^r]$$

with

$$[T_\eta^p] = \begin{bmatrix} 1 & 0 & 0 & 0 & 0 & 0 \\ 0 & c_p^2 & s_p^2 & c_p s_p & 0 & 0 \\ 0 & s_p^2 & c_p^2 & -c_p s_p & 0 & 0 \\ 0 & -2c_p s_p & 2c_p s_p & c_p^2 - s_p^2 & 0 & 0 \\ 0 & 0 & 0 & 0 & c_p & -s_p \\ 0 & 0 & 0 & 0 & s_p & c_p \end{bmatrix} \quad \begin{aligned} c_p &= \cos \theta_p \\ s_p &= \sin \theta_p \end{aligned}$$

$$[T_\varepsilon^q] = \begin{bmatrix} c_q^2 & 0 & s_q^2 & 0 & c_q s_q & 0 \\ 0 & 1 & 0 & 0 & 0 & 0 \\ s_q^2 & 0 & c_q^2 & 0 & -c_q s_q & 0 \\ 0 & 0 & 0 & c_q & 0 & -s_q \\ -2c_q s_q & 0 & 2c_q s_q & 0 & c_q^2 - s_q^2 & 0 \\ 0 & 0 & 0 & s_q & 0 & c_q \end{bmatrix} \quad \begin{array}{l} c_q = \cos \theta_q \\ s_q = \sin \theta_q \end{array}$$

$$[T_\varepsilon^r] = \begin{bmatrix} c_r^2 & s_r^2 & 0 & 0 & 0 & c_r s_r \\ s_r^2 & c_r^2 & 0 & 0 & 0 & -c_r s_r \\ 0 & 0 & 1 & 0 & 0 & 0 \\ 0 & 0 & 0 & c_r & -s_r & 0 \\ 0 & 0 & 0 & s_r & c_r & 0 \\ -2c_r s_r & 2c_r s_r & 0 & 0 & 0 & c_r^2 - s_r^2 \end{bmatrix} \quad \begin{array}{l} c_r = \cos \theta_r \\ s_r = \sin \theta_r \end{array}$$

and

$$[T_\sigma] = [T_\sigma^p] \cdot [T_\sigma^q] \cdot [T_\sigma^r]$$

with

$$[T_\sigma^p] = \begin{bmatrix} 1 & 0 & 0 & 0 & 0 & 0 \\ 0 & c_p^2 & s_p^2 & 2c_p s_p & 0 & 0 \\ 0 & s_p^2 & c_p^2 & -2c_p s_p & 0 & 0 \\ 0 & -c_p s_p & c_p s_p & c_p^2 - s_p^2 & 0 & 0 \\ 0 & 0 & 0 & 0 & c_p & -s_p \\ 0 & 0 & 0 & 0 & s_p & c_p \end{bmatrix} \quad \begin{array}{l} c_p = \cos \theta_p \\ s_p = \sin \theta_p \end{array}$$

$$[T_\sigma^q] = \begin{bmatrix} c_q^2 & 0 & s_q^2 & 0 & 2c_q s_q & 0 \\ 0 & 1 & 0 & 0 & 0 & 0 \\ s_q^2 & 0 & c_q^2 & 0 & -2c_q s_q & 0 \\ 0 & 0 & 0 & c_q & 0 & -s_q \\ -c_q s_q & 0 & c_q s_q & 0 & c_q^2 - s_q^2 & 0 \\ 0 & 0 & 0 & s_q & 0 & c_q \end{bmatrix} \quad \begin{array}{l} c_q = \cos \theta_q \\ s_q = \sin \theta_q \end{array}$$

$$[T_{\sigma}^r] = \begin{bmatrix} c_r^2 & s_r^2 & 0 & 0 & 0 & 2c_r s_r \\ s_r^2 & c_r^2 & 0 & 0 & 0 & -2c_r s_r \\ 0 & 0 & 1 & 0 & 0 & 0 \\ 0 & 0 & 0 & c_r & -s_r & 0 \\ 0 & 0 & 0 & s_r & c_r & 0 \\ -c_r s_r & c_r s_r & 0 & 0 & 0 & c_r^2 - s_r^2 \end{bmatrix} \quad \begin{array}{l} c_r = \cos \theta_r \\ s_r = \sin \theta_r \end{array}$$

VITA

Monish Shivappa Mamadapur received his Bachelor of Engineering degree in Mechanical Engineering from Rashtreeya Vidyalaya College of Engineering, Bangalore, under Visvesvaraya Technological University, Belgaum, India in 2005. He entered the Mechanical Engineering program at Texas A&M University in September 2005 and received his Master of Science degree in December 2007.

Mr. Mamadapur may be reached at Department of Mechanical Engineering, 3123 TAMU, College Station, TX 77843-3123. His email is: seriouslycomic@gmail.com.